FOCI-MOPS v1 - Integration of Marine Biogeochemistry within the Flexible Ocean and Climate Infrastructure version 1 (FOCI 1) Earth system model

Chia-Te Chien[1], Jonathan V. Durgadoo[1,2], Dana Ehlert[1], Ivy Frenger[1], David P. Keller[1], Wolfgang Koeve[1], Iris Kriest[1], Angela Landolfi[1,3], Lavinia Patara[1], Sebastian Wahl[1], and Andreas Oschlies[1,2]

[1]GEOMAR Helmholtz-Zentrum für Ozeanforschung Kiel, Düsternbrooker Weg 20, 24105 Kiel, Germany
[2]Kiel University, 24098 Kiel, Germany
[3]ISMAR-CNR, via Fosso del Cavaliere 100, 0133 Rome Italy

Correspondence: Chia-Te Chien (cchien@geomar.de)

Abstract.

The consideration of marine biogeochemistry is essential for simulating the carbon cycle in an Earth system model. Here we present the implementation and evaluation of a marine biogeochemical model, Model of Oceanic Pelagic Stoichiometry (MOPS) in the Flexible Ocean and Climate Infrastructure (FOCI) climate model. FOCI-MOPS enables the simulation of marine biological processes, the marine carbon, nitrogen and oxygen cycles with prescribed or prognostic atmospheric CO_2 concentration. A series of experiments covering the historical period (1850 – 2014) were performed following the DECK (Diagnostic, Evaluation and Characterization of Klima) and CMIP6 (Coupled Model Intercomparison Project 6) protocols. Overall, modelled biogeochemical tracer distributions and fluxes, as well as transient evolution in surface air temperature, air-sea CO_2 fluxes, and changes in ocean carbon and heat contents, are in good agreement with observations. Modelled inorganic and organic tracer distributions are quantitatively evaluated by statistically-derived metrics. Results of the FOCI-MOPS model, including sea surface temperature, surface pH, oxygen (100 – 600 m), nitrate (0 - 100 m), and primary production, are within the range of other CMIP6 model results. Overall, the evaluation of FOCI-MOPS indicates its suitability for Earth climate system simulations.

1 Introduction

The strongest anthropogenic forcing on the Earth system during the last century has been a rise in atmospheric CO_2 concentrations due to anthropogenic CO_2 emissions (IPCC, 2019). About half of those emissions are currently taken up by the terrestrial biosphere and the ocean (Friedlingstein et al., 2020; Sabine et al., 2004; Gruber et al., 2019), shared to about equal proportion. The anthropogenic carbon is taken up by the ocean mostly due to the physical-chemical processes of the solubility pump (Sarmiento and Gruber, 2002) and on land by increased net primary productivity (Arneth et al., 2010). In addition to the uptake of anthropogenic carbon, the natural carbon fluxes are perturbed by climate change. In the ocean, the increase in seawater temperature directly decreases the solubility of CO_2. Global warming also leads to changes in ocean circulation, for

instance, shifting wind patterns might change the Southern Ocean upwelling and increase natural CO_2 outgassing (Le Quéré et al., 2007). The increased natural outgassing in the Southern Ocean is also shown in modeling studies (Zickfeld et al., 2007; Tjiputra et al., 2010). The chemical capacity of the ocean to take up CO_2 decreases with increasing CO_2 concentrations in seawater (Friedlingstein et al., 2006; Riebesell et al., 2009; Fassbender et al., 2017). On land, increasing temperatures limit plant growth in low latitudes and enhance the decomposition of organic matter (Pugnaire et al., 2019; Lin et al., 2010; Sarmiento and Gruber, 2002). Those mechanisms are expected to lead to a weakening of the terrestrial and marine sinks for the extra carbon arising from human activity, but a detailed quantitative understanding is still lacking.

For a comprehensive investigation of climate-carbon cycle interactions and possible feedbacks, the implementation of ocean biogeochemistry in climate models is crucial. While existing global ocean biogeochemical models simulate surface ocean pCO_2 reasonably well, there are still discrepancies between the model results and data products concerning oceanic CO_2 sink estimates (Hauck et al., 2020). In order to improve our understanding of the Earth system, continuous development of the ocean in Earth system models is required. This includes an adequate representation of the marine carbon uptake variability on the finite atmospheric CO_2 pool and hence on climate.

A new climate model, the Flexible Ocean and Climate Infrastructure (FOCI), has been successfully developed (Matthes et al., 2020). The model consists of a fully coupled atmosphere-ocean-sea-ice general circulation model and includes a land model, the Jena Scheme for Biosphere-Atmosphere Coupling in Hamburg (JSBACH; Brovkin et al., 2009; Reick et al., 2013), plus options for interactive stratospheric chemistry in the atmosphere, the ECHAM6.3-HAM2.3-MOZ1.0 (ECHAM6-HAMMOZ; Schultz et al., 2018), and the option for regional grid refinement in the ocean, the Adaptive Grid Refinement In Fortran package (AGRIF; Debreu et al., 2008) for the Nucleus for European Modelling of the Ocean (NEMO; Madec, 2016). Here we present the implementation of the marine biogeochemical model component, Model of Oceanic Pelagic Stoichiometry (MOPS; Kriest and Oschlies, 2015) into FOCI. MOPS enables the simulation of marine biological processes, the marine carbon, nitrate (NO_3), phosphate (PO_4), and oxygen (O_2) cycles. MOPS features a smaller number of prognostic variables than other Coupled Model Intercomparison Project Phase 6 (CMIP6) models (Séférian et al., 2020) (e.g. does not simulate iron and silicate), which makes it computationally a comparatively more efficient model. Biogeochemical parameters in MOPS have been calibrated so that it reproduces well observed nutrient distributions and fluxes such as N_2 fixation and denitrification (Kriest and Oschlies, 2015). Because circulation patterns used in earlier calibration exercises of MOPS (Kriest et al., 2020) are similar to those of the physics-only FOCI model (Matthes et al., 2020), a similar performance of MOPS is expected here.

In this paper, we present the technical description of the marine biogeochemistry component in FOCI and its validation for the model mean state following a 500 years spin-up simulation, for historical simulations covering the period from 1850 to 2014 and control simulations with pre-industrial conditions. We also discuss the variability among ensemble members of each set-up and the differences between CO_2-concentration-driven and CO_2-emission-driven experiments.

2 Model description

2.1 Ocean circulation and the coupling to the atmosphere

The physical ocean model component in FOCI is detailed in Matthes et al. (2020). In brief, the ocean model is built on NEMO version 3.6 (Madec, 2016) with a nominal global ocean resolution of $1/2^\circ$ on a tri-polar grid (ORCA05), with Louvain-la-Neuve sea Ice Model version 2 (LIM2) as the dynamic-thermodynamic sea-ice model (Madec, 2016). There are 46 vertical levels with thicknesses varying from 6 m at the surface to 250 m in the deep ocean. A two-step flux-corrected transport, total variance dissipation scheme (TVD; Zalesak, 1979) is used for tracer advection to ensure positive-definite values. Tracer diffusion is aligned along isopycnals, and viscosity is applied via a bi-Laplacian operator. The exchange of momentum, heat, freshwater fluxes, and sea-ice properties between the ocean and the atmosphere is realised by the OASIS3-MCT coupler (Valcke, 2013). Note that all air-sea flux calculations are performed in the atmospheric module and have to be mapped from the coarser spatial grid of the atmospheric model (approximately 1.8°) to the finer one of the ocean ($1/2^\circ$).

2.2 Ocean biogeochemistry

MOPS (Model of Oceanic Pelagic Stoichiometry) simulates the elemental cycles of oceanic phosphorus, nitrogen and oxygen, and consists of seven compartments, namely phosphate, nitrate, oxygen, phytoplankton, zooplankton, detritus, and dissolved organic matter (DOM) (Fig. 1). We here only provide a general overview of the model structure and the changes made for its implementation in FOCI. For further details of MOPS, we refer the reader to the original description of MOPS by Kriest and Oschlies (2015), and to the detailed model description in Appendix A.

For the implementation in FOCI, MOPS has been complemented with a carbon cycle that includes biological uptake and remineralisation effects on dissolved inorganic carbon (DIC) and alkalinity (ALK) (assuming fixed elemental ratios according to the stoichiometry by Paulmier et al., 2009), and the effects of formation and dissolution of calcite on these two tracers. For biogenic calcite production and dissolution, we implement an implicit approach (Schmittner et al., 2008) where the production of calcite is calculated from organic detritus production in a fixed ratio. Integrated over the entire water column, and assuming a fixed molar $\mathrm{CaCO_3}$:P ratio from the production of detritus, at each time step, the newly produced vertically integrated calcite is then immediately distributed and released as DIC and ALK over the water column with an e-folding length scale. Air-sea gas exchange of CO_2 at the sea surface is calculated according to Orr et al. (2017). Altogether, the ocean biogeochemistry is simulated via nine prognostic tracers and five chemical elements (PO_4 (P), NO_3 (N), O_2 (O), DIC (C), ALK (C, N, P), phytoplankton (C, N, P), zooplankton (C, N, P), detritus (C, N, P, Ca), and DOM (C, N, P)).

In MOPS phytoplankton growth depends on ambient PO_4, NO_3, temperature and light. Phytoplankton is grazed by zooplankton, parameterised by a Holling-III function, that uses a sigmoidal functional response of the grazing rate to increasing food (Holling and Buckingham, 1976). Subsequent zooplankton egestion and plankton mortality produce sinking detritus and neutrally buoyant DOM. The sinking speed of detritus increases linearly with depth, and the remineralisation rate is constant and temperature-independent. In the absence of lateral or vertical exchange, these would result in a flux profile given by a power law of depth (the so-called "Martin" curve with exponent b; Martin et al., 1987). However, the model also simulates

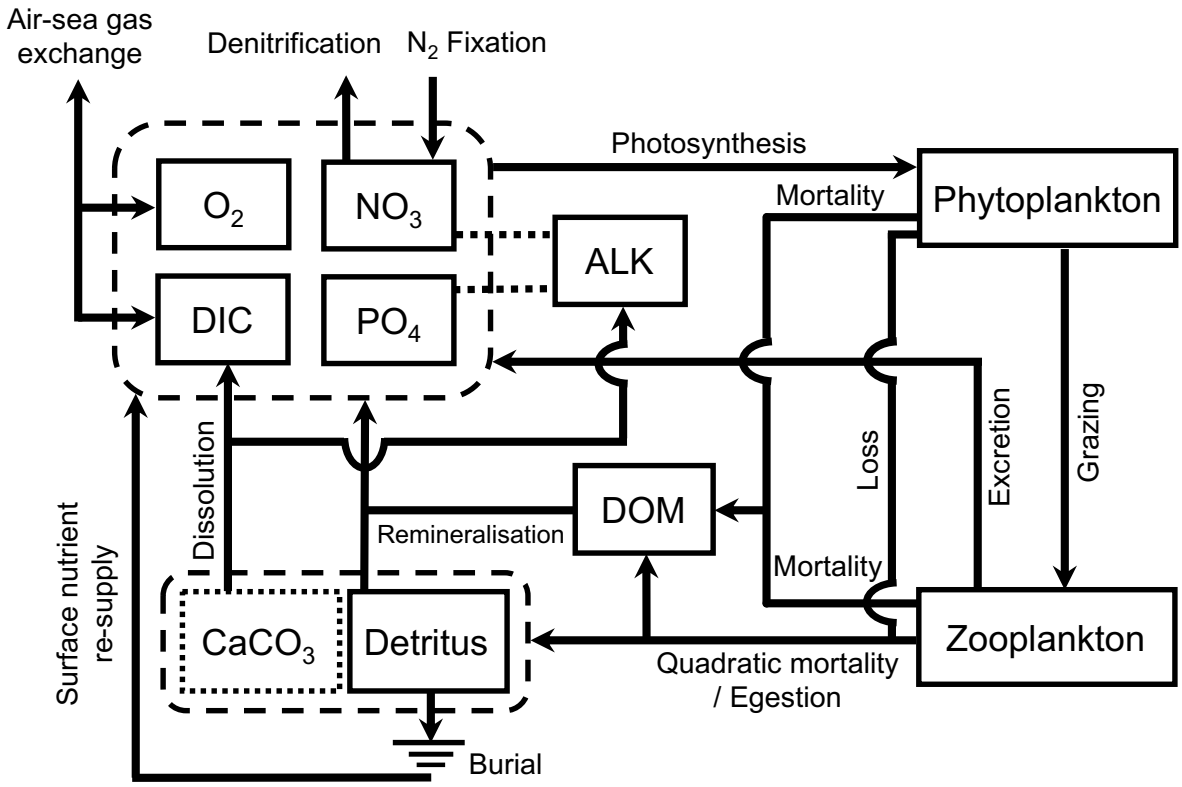

Figure 1. Schematic of the ocean biogeochemistry model FOCI-MOPS. Arrows indicate processes and fluxes between model compartments (solid squares). The dashed lines between ALK and NO_3, and between ALK and PO_4, depict that ALK is affected by changes in NO_3 and PO_4. $CaCO_3$ is represented as a dotted square for it is not a prognostic tracer in the model. See Appendix A for a detailed description. ALK: Alkalinity; DIC: dissolved inorganic carbon; DOM: dissolved organic matter.

oxygen-dependent remineralisation of organic matter. If oxygen falls below a threshold, denitrification sets in during anaerobic remineralisation and reduces NO_3, albeit at a slower rate than aerobic remineralisation. The decrease of remineralisation caused by oxygen deficiency, especially in oxygen minimum zones, distorts the nominal value of b. There is no benthic denitrification in the model. The loss of fixed nitrogen due to denitrification, affects the supply of NO_3 to the surface and influences nitrogen fixation at the sea surface, which, in the model, is diagnosed depending on temperature and the local ratio between simulated NO_3 and PO_4.

There is no sediment module in MOPS. Organic detritus arriving at the seafloor is partially buried and the burial fraction is depending on the rain rate (Appendix A3). The resulting loss of phosphorus and nitrogen to the sediment is compensated for by adding an amount of PO_4 and NO_3 equivalent to the globally integrated burial, distributed homogeneously in the topmost model layer, rather than through river runoff. Likewise, we account for the burial loss of organic carbon and the associated virtual flux of ALK by a compensating supply of DIC and a decrease of ALK homogeneously distributed over the global sea

surface. Supply and removal of these tracers to the surface layer ensures mass conservation with respect to the fluxes across the sea floor. Calcite arriving at the seafloor is not buried but immediately dissolved in the deepest model box, accommodating for the fact that a climate model like FOCI does not allow for the spin-up times needed for $CaCO_3$ sediments to reach a steady state.

With the implementation of MOPS, one year of FOCI-MOPS simulation takes 0.6 hrs and costs about 730 CPU hours with 1260 CPUs (Intel® Xeon® Platinum 9242 Processor) on 14 nodes on the North-German Supercomputing Alliance (HLRN) complex LISE at the Zuse Institute Berlin (ZIB). For details of the hardware, please refer to the HLRN-IV documentation on HLRN web page (https://www.hlrn.de/). With the same CPU configuration, the computing time for FOCI-MOPS increases 26% compared to a physics-only FOCI version. For comparison, an increase of 42% computing cost was found for the biogeochemical component PISCESv2-gas implemented in CNRM-ESM2-1 with an online grid-coarsening algorithm (Berthet et al., 2019).

A direct calibration by means of optimisation of FOCI-MOPS, a computationally expensive ESM, is presently not feasible. Therefore we selected MOPS parameters that resulted from a calibration using transport matrices that were derived from a circulation of a reanaylsis dataset, the Estimating the Circulation and Climate of the Ocean (ECCO), which is computationally more efficient. In particular, six biogeochemical model parameters of MOPS were adjusted via an automatic calibration procedure against observed nutrient and oxygen distributions as described in Kriest et al. (2020, optimisation ECCO*). While the circulation of the ECCO and FOCI largely are similar, to account for existing differences, we manually adjusted three of six parameters after initial tests as described in Appendix A5. The Appendix also describes the choice of parameters regulating calcite formation and dissolution. The final full set of parameter values can be found in Table A1.

2.3 Model simulations and data used for model evaluation

Following the CMIP6 protocol (Eyring et al., 2016), we performed a series of experiments to evaluate FOCI-MOPS (Table 1). A 500 years spin-up with marine biogeochemistry (*spinup*) was restarted from the end of a 1500 years 'physics-only' FOCI spin-up under year 1850 climate conditions (e.g. solar radiation, greenhouse gases, atmospheric nitrogen deposition, sulfate aerosol from volcanic eruptions, land usage, and population density. See Matthes et al. (2020) for details of the boundary conditions.) Details of physical characteristics of the 1500 years spin-up (FOCI1.3-SW038) are described in Matthes et al. (2020), including a cold bias in sea surface temperature (SST) and surface air temperature (SAT) in the North Atlantic and a warm bias in the Southern Ocean. Also the depth of the maximum transport of the Atlantic Meridional Overturning Circulation (AMOC) is shallower compared to the RAPID array observations (McCarthy et al., 2015). For the 500 years FOCI-MOPS spin-up, phosphate (PO_4), nitrate (NO_3), and oxygen (O_2) are initialised using the WOA2013 data set (Garcia et al., 2013a, b), and pre-industrial DIC and ALK are taken from GLODAPv2.2016b (Lauvset et al., 2016). The 480th, 490th, and 500th year of the *spinup* served as different initial conditions for an ensemble of three pre-industrial control (*piControl*) and transient historical (*Hist*) simulations (years 1850–2014) with prescribed atmospheric CO_2 concentrations. We also carried out a set of experiments where, instead of prescribing atmospheric CO_2 concentrations, the model was forced with CO_2 emissions, and the atmospheric CO_2 was calculated prognostically. For those experiments, we use the 480th year of the FOCI-MOPS spin-up as

Table 1. Overview of FOCI-MOPS simulations.

Experiment	Years (no.)	Description
spinup	1 – 500 (500)	A spin-up run under pre-industrial (year 1850) climate conditions restarted from the end of a 1500 years 'physics-only' FOCI spin-up
"ESM-spinup"	1 – 250 (250)	A zero-emission-driven spin-up under 1850 climate conditions restarted from the 480th year of the FOCI-MOPS *spinup*
piControl	1 – 165 (3x165)	Pre-industrial simulations under 1850 climate conditions restarted from years 480, 490, and 500 of the FOCI-MOPS *spinup*
ESM-piControl	1 – 165 (3x165)	Zero-emission-driven pre-industrial simulations under 1850 climate conditions restarted from years 230, 240, and 250 of the *"ESM-spinup"*
Hist	1850 – 2014 (3x165)	Historical simulations following the CMIP6 protocol with prescribed atmospheric CO_2 concentrations restarted from years 480, 490, and 500 of the FOCI-MOPS *spinup*
ESM-Hist	1850 – 2014 (3x165)	Historical simulations following the CMIP6 protocol with prescribed CO_2 emissions restarted from years 230, 240, and 250 of the FOCI-MOPS *"ESM-spinup"*

a starting point for a 250 years CO_2 zero-emission-driven spin-up ("*ESM-spinup*", with quotation marks for a spin-up shorter than *spinup*) to allow for some equilibration between the atmosphere, land, and ocean carbon compartments. An ensemble of three ESM model pre-industrial control (*ESM-piControl*) and transient historical (*ESM-Hist*) was then started from the 230th, 240th and 250th year of "*ESM-spinup*".

To evaluate the performance of FOCI-MOPS, we compared the distribution of inorganic tracers in *Hist* to interpolated and non-interpolated data of GLODAPv2.2016b (Lauvset et al., 2016; Olsen et al., 2016). For O_2, NO_3, PO_4, and ALK, model outputs are averaged over 1972 to 2013, and for DIC, modelled year 2002 is used. For organic tracers, 10-year mean (from 2005 to 2014) chlorophyll estimates from remote sensing (MODIS-Aqua, https://jeodpp.jrc.ec.europa.eu/ftp/public/JRC-OpenData/GMIS/satellite/9km/ , downloaded on 20 January 2021, Melin, 2013), together with in-situ observations of meso-zooplankton, particulate organic nitrogen, and dissolved organic phosphorus, are used for comparison. Details of the biogeochemical data sets and model evaluation metrics are described in Appendix B.

3 Evaluation of model results

3.1 Temporal evolution of model simulations

3.1.1 Spin-up drift

Over the first 100 years of the FOCI-MOPS 500-year spin-up (*spinup*), a small (<1.5%) decrease in inorganic nutrients (PO_4 and NO_3) is used to build up organic material (plankton biomass, DOM, and detritus), as they are initialized to zero at the start of *spinup*. After these initial adjustments, most of the global mean tracer concentrations and globally integrated fluxes showed drifts that were small relative to their mean concentrations (up to 0.1% in the carbon flux at 2000m) and reached or

asymptotically approached a steady state at the end of *spinup* (Fig. 2). An exception is NO_3 because the marine nitrogen cycle did not reach a steady state, with N_2 fixation and denitrification not yet being in equilibrium after 500 years. This is commonly observed in models due to the spatial separation of these counteracting N-cycle processes. The equilibration of marine N_2 fixation and denitrification can take thousands of years (Falkowski, 1997; Oschlies et al., 2019). Owing to a net NO_3 loss due to a higher global denitrification than N_2 fixation rate, together with the build-up of organic matter in the beginning, global-average NO_3 is about 1.1 mmol N m^{-3} lower at the end of the *spinup* compared to the beginning, amounting to a decrease of 0.007% per year. After a small positive spike in the beginning, O_2 concentrations continuously decrease throughout the *spinup* and in the end are close to a steady state. The loss of O_2 indicates that, in the model the supply of O_2 via mixing is too slow, and/or the consumption due to remineralisation is overestimated. The changes in O_2 concentration are associated with the temporal drift of the carbon export across 2000 m. While the export flux at 100 m reached a steady state already after 100 years, the flux at 2000 m was still increasing at the end of the spin-up. This reflects that the remineralisation of organic matter was slowing down in the upper 2000 meters due to the decreasing O_2 concentration, allowing an increasing fraction of organic material to remineralise below 2000 meters. After 500 years, global-average O_2 is about 8.4 mmol O_2 m^{-3} (5 %) lower than in the beginning. In the model, DIC varies mainly due to the build-up of organic matter and changes in air-sea CO_2 fluxes. Drift in the DIC inventory during the last 100 years in the *spinup* is -0.086 Pg C yr^{-1}, which meets the "acceptably small drift" ($\pm$0.1 Pg C yr^{-1}) suggested in Jones et al. (2016). Global $CaCO_3$ production equals dissolution as there is no dynamic $CaCO_3$ pool in the model. Therefore, the alkalinity inventory is only affected by the changes in PO_4 and NO_3. Since PO_4 and NO_3 decrease during the formation of organic matter, and the nitrate reservoir additionally decreases resulting from the imbalance of denitrification and N_2 fixation (plus nitrification), the ALK inventory increases during the *spinup*, in the stoichiometric ratio of 0.9914:-1 ALK:NO_3 (Paulmier et al., 2009). The remaining small drifts in the *spinup* might exert an effect on the historical simulations, where they were accounted for by subtracting the respective control simulations.

3.1.2 Historical simulations

Even after the 500 year spin-up (see section 3.1.1), some drifts in tracers and fluxes can still exist, and can been seen in the *piControl* and *ESM-piControl* (Fig. S1 – S2). The drifts in *Hist* and *ESM-Hist* (Fig. S3 – S4) runs are removed by subtracting the *piControl* and *ESM-piControl* simulation trends from the corresponding historical runs (Fig. 3). Drifts continue over the additional years of the CO_2 emission driven spin-up (*"ESM-spinup"*), therefore, the absolute tracer concentrations and fluxes in *ESM-Hist*, which is initialised from the end of *"ESM-spinup"*, are partly different from those in the *Hist* runs, and as apparent in the time series of NO_3, O_2, DIC, and ALK, discussed above. Nevertheless, the historical evolution and variability of the *ESM-Hist* simulation is qualitatively and quantitatively very similar to the one in *Hist*. In the *Hist* simulations, PO_4 increases slightly mainly due to a decrease in dissolved organic phosphorus (DOP; the model also implicitly represents DOM in phosphorus units in a C:N:P molar ratio of 117:16:1), which declines by 0.007% per year. Decreases in phytoplankton, zooplankton, and detritus are also small, ranging from 0.005% to 0.01% per year. Global-average NO_3 in 2014 is about 0.017 mmol N m^{-3} (0.06 %) higher than in 1850. One reason for the increase in NO_3 is a decrease of denitrification. The reduction of DOM and organic particle pools also contributes to the NO_3 increase (0.006 mmol N m^{-3}). The changes in NO_3 are reflected

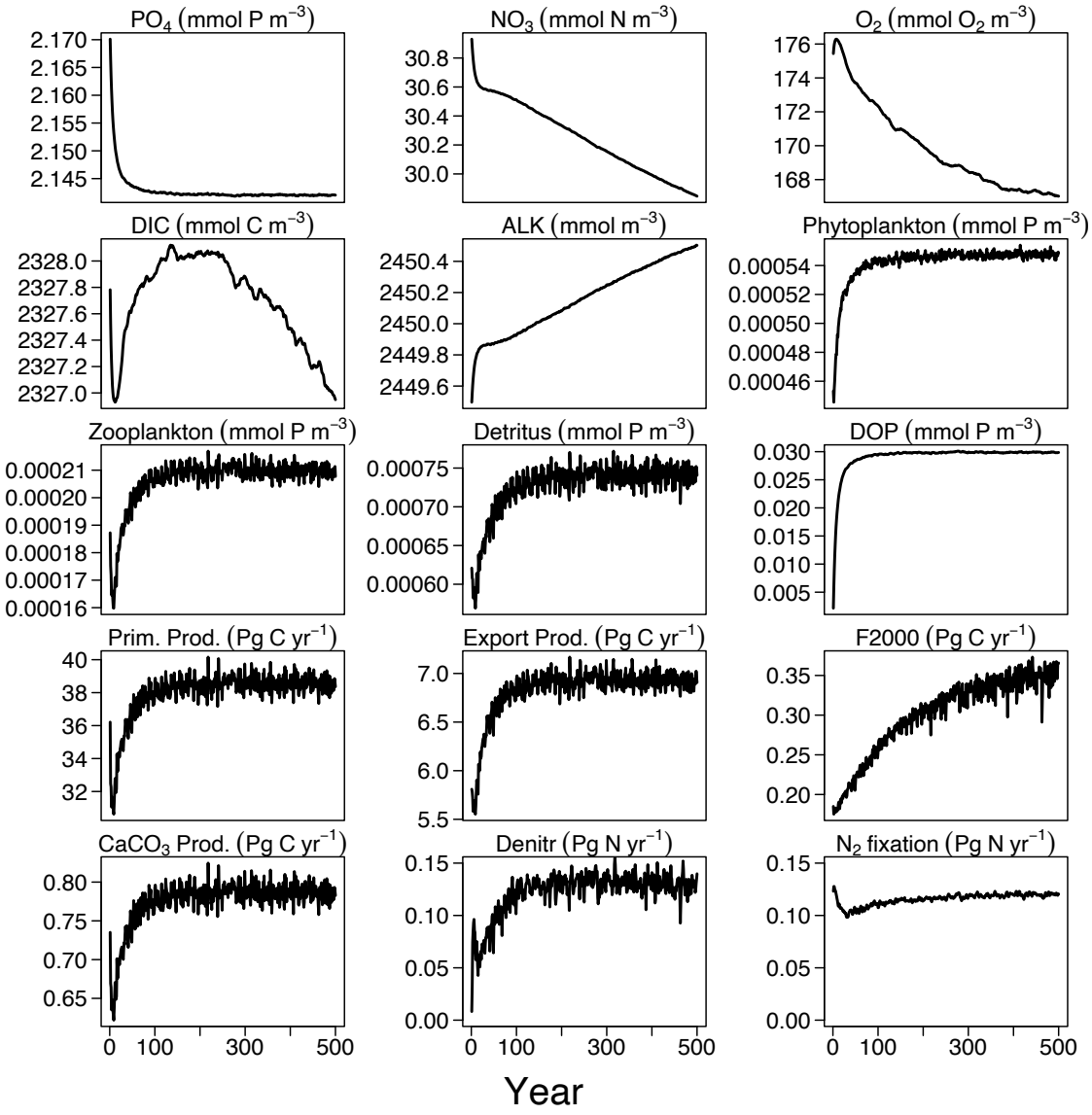

Figure 2. Time series of tracer concentrations and fluxes in the 500 year *spinup* experiment, of the inorganic tracers (PO_4, NO_3, O_2, dissolved inorganic carbon (DIC), and alkalinity (ALK)), organic tracers (phytoplankton, zooplankton, detritus, and dissolved organic phosphorus (DOP)), and fluxes (primary production, export production at 100 m and carbon flux at 2000 m (F2000), $CaCO_3$ production, denitrification (Denitr), and N_2 fixation (Nfix)).

also in a decreasing ALK inventory. The simulated relative decrease of the O_2 inventory is higher than that of PO_4 and NO_3. In the model, the ocean loses about 1.5 mmol O_2 m^{-3} (0.9%) of oxygen between 1850 and 2014. Changes in circulation and
185 mixing, together with the decrease in solubility due to a warming ocean, dominate the decline in marine O_2 content. The small decrease in export production would lead to reduced O_2 consumption via respiration, and therefore elevated rather than reduce

oxygen inventory. Globally averaged DIC increases by 8 mmol C m^{-3} (0.35%), mainly due to increased air-sea CO_2 fluxes into the ocean under rising atmospheric CO_2, i.e. the uptake of anthropogenic CO_2.

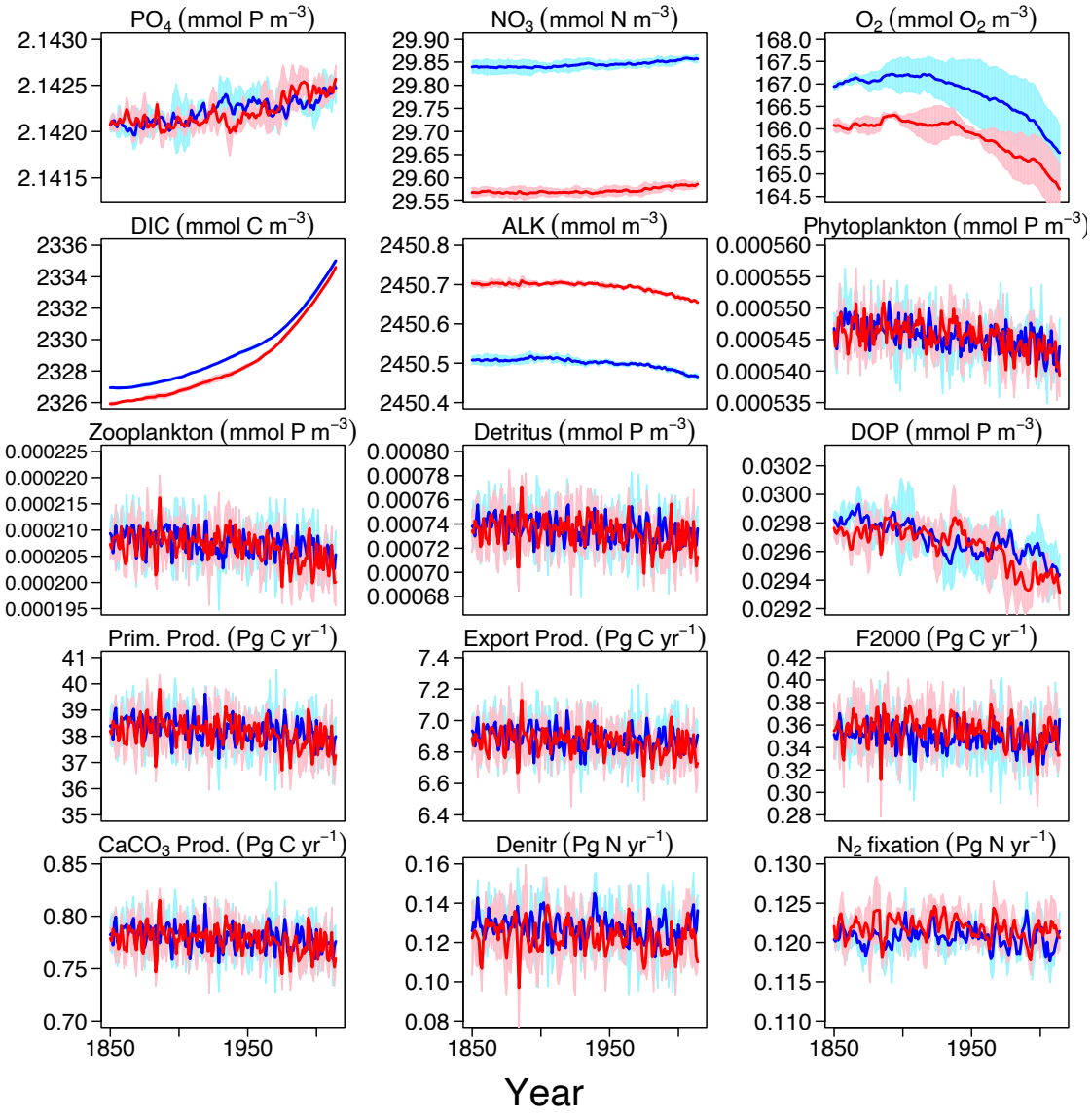

Figure 3. Time series of tracer concentrations and fluxes for the 165 years (1850 – 2014) *Hist* and *ESM-Hist* experiments, each for a three member ensemble. Each ensemble member is corrected by the drifts in the respective *piControl* and *ESM-piControl* runs. Dark blue and dark red lines stand for the mean, and light blue and light red shaded areas represent one standard deviation in *Hist* and *ESM-Hist*, respectively. The arrangement of the sub panels is the same as in Fig. 2

3.2 Biogeochemical model performance

3.2.1 Spatial distribution of inorganic tracers

The surface concentration of O_2 is primarily determined by the temperature-dependent solubility. In the ocean interior, it is a sensitive balance between ocean circulation and oxygen consumption during remineralisation of detritus and dissolved organic matter (DOM). In FOCI-MOPS, water column denitrification occurs in low-oxygen waters when O_2 concentration is below 36 mmol O_2 m^{-3}. The low-oxygen waters develop where the physical supply of O_2 is sluggish and O_2 consumption via respiration is high. The model reproduces the low-oxygen waters at the eastern margins of tropical and subtropical ocean basins (Fig. 4a, S5). In the zonally averaged ocean basin means, the low-oxygen waters are situated between 100 to 1500 m in the Atlantic, the Indian, and the Pacific Oceans (Fig. 4a, d – f). In the same depth range, the modelled O_2 is biased low, in particular in the southern hemisphere (Fig. 4i – k, S5). Another region with clear negative O_2 biases can be seen at depths below 1500 m and all the way to the bottom in the Pacific Ocean (Fig. 4k). The low biases in the zonal mean is due to an underestimated O_2 in the eastern equatorial Pacific (Fig. S5), a feature that is likely due to overestimated production in the euphotic zone above, and imperfect physics and remineralisation settings, which are commonly found in numerical models (Dietze and Loeptien, 2013; Ilyina et al., 2013; Cabré et al., 2015; Paulsen et al., 2018). In general, O_2 in the model is biased high between 1000–3000 m and is biased low below 3000 m. In additional to the biological processes, the difference can be explained by the ventilation of the water masses. The modelled AMOC has a shallow bias and indeed is weaker in the deep water (3000 – 5000 m) (Fig. 5), as remarked also in Matthes et al. (2020), and common across climate models (e.g. Weijer et al. (2020)). A more sluggishly ventilated deep water in latitude-depth structure (Fig. 5a) is consistent with the higher concentration in inorganic tracers and the negative biases in O_2.

Surface phosphate (PO_4) concentrations simulated by FOCI-MOPS, in general, agree with observations with positive biases in the Atlantic and a negative bias in the subarctic gyre in the North Pacific Ocean (Fig. 6a, b). In the interior, the model–data misfits are generally smallest in the Southern Ocean (SO) and the Arctic (Fig. 6h, l). In the Atlantic, Indian, and Pacific Oceans, modelled PO_4 shows positive biases at around 100 - 1000 m and below 3000 m, and negative biases between 1000 and 3000 m (Fig. 6i – k).

In order to better understand the distribution of PO_4 we adopt the methodology of Duteil et al. (2012) and calculate regenerated (PO_{4reg}) and preformed PO_4 (PO_{4pre}) assuming oxygen saturation (O_{2sat}) at isopycnal outcrops (e.g. PO_{4reg} = AOU/r-O_2:PO_4, AOU = O_{2sat}-O_{2obs}, PO_{4pre} = PO_4-PO_{4reg}). For observations, we apply the O_2:PO_4 ratio of 170 mol O_2: mol P estimated in Anderson and Sarmiento (1994). For model output, we apply the ratio of 165.08044 mol O_2: mol P used in the model.

Except for the deep Atlantic (deeper than 3000 m), preformed PO_4 is generally too low in the ocean interior compared to observations (Fig. 7h – k). A lack of iron limitation in the model could cause a too strong uptake of PO_4 by phytoplankton in iron limited regions, such as the Southern Ocean, and lead to too low preformed PO_4. The overestimated regenerated PO_4 in the deep Pacific > 3000 m (Fig. 8k) contributes to the overall high bias of PO_4 (Fig. 6k), and is consistent with the low O_2 biases in the same region (Fig. 4k, S5). The high bias of PO_4 may at least partly be explained by excessive remineralisation of

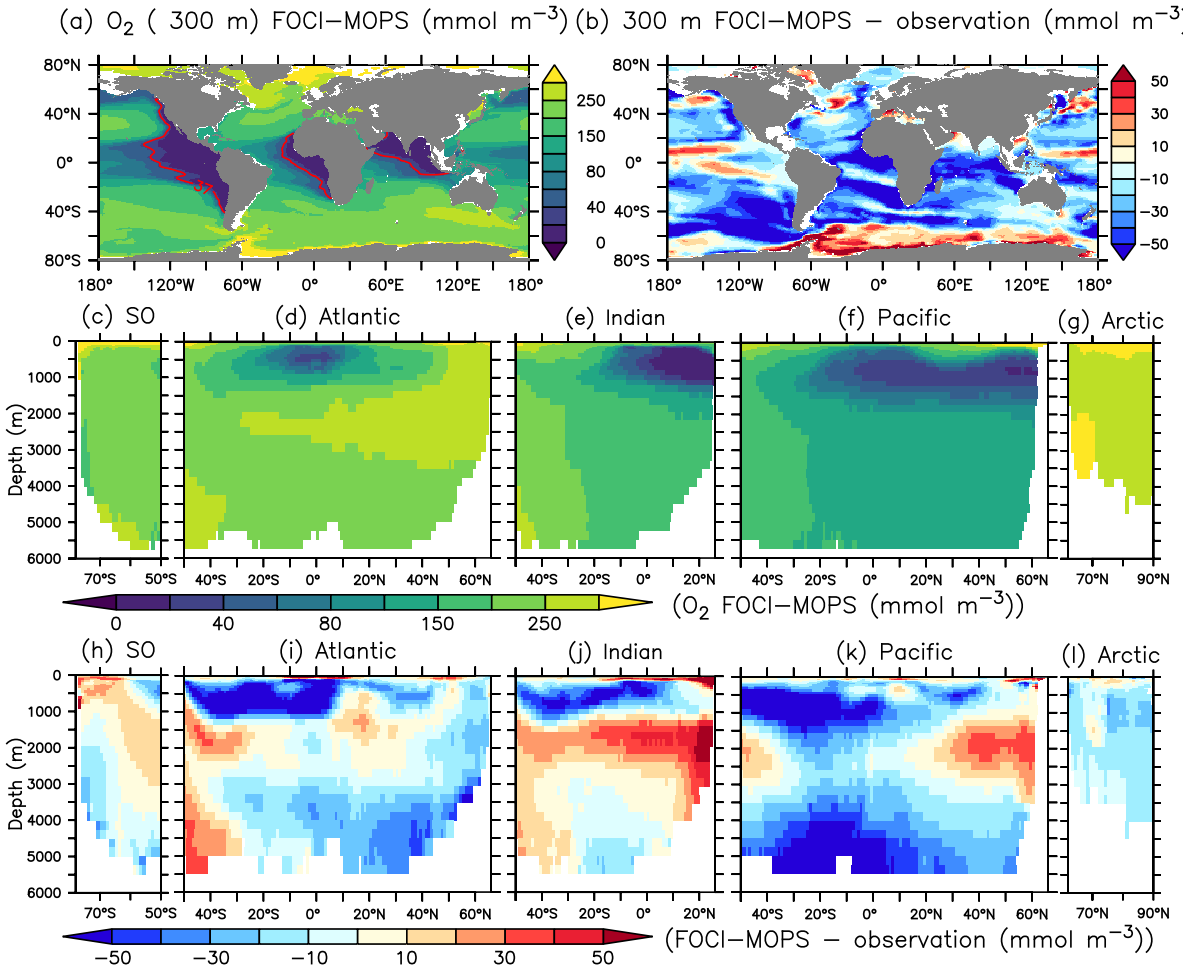

Figure 4. O_2 climatology over 1972 – 2013 of the *Hist* simulations at (a) 300 m depth and zonally averaged across the (c) Southern Ocean, (d) Atlantic, (e) Indian, (f) Pacific, and (g) Arctic Ocean in FOCI-MOPS. The corresponding difference model minus observation is shown in (b), (h), (i), (j), (k), and (l), respectively. Observational data are from GLODAPv2.2016b which covers years 1972 to 2013 (Lauvset et al., 2016; Olsen et al., 2016). Red contour lines in (a) depict O_2 of 36 mmol O_2 m^{-3}, below this concentration anaerobic remineralisation kicks in in the model. Partitioning of ocean basins follows the World Ocean Atlas 2013 definitions.

detritus and DOM in the eastern Pacific Ocean as a result of overestimated primary production (PP) and export production (EP) (see section 3.3). A too sluggish ventilation of these water masses could also explain the excessive accumulation of regenerated PO_4 and apparent oxygen utilisation (Fig. 5), as the PO_4 is also overestimated in the deep Atlantic Ocean.

Biases of climatological nitrate NO_3 overall show a similar distribution as for phosphate (Fig. 9a). Simulated NO_3 differs from the pattern of PO_4 mostly in low latitudes at intermediate depth. Some positive biases can be seen in the Arctic and near the

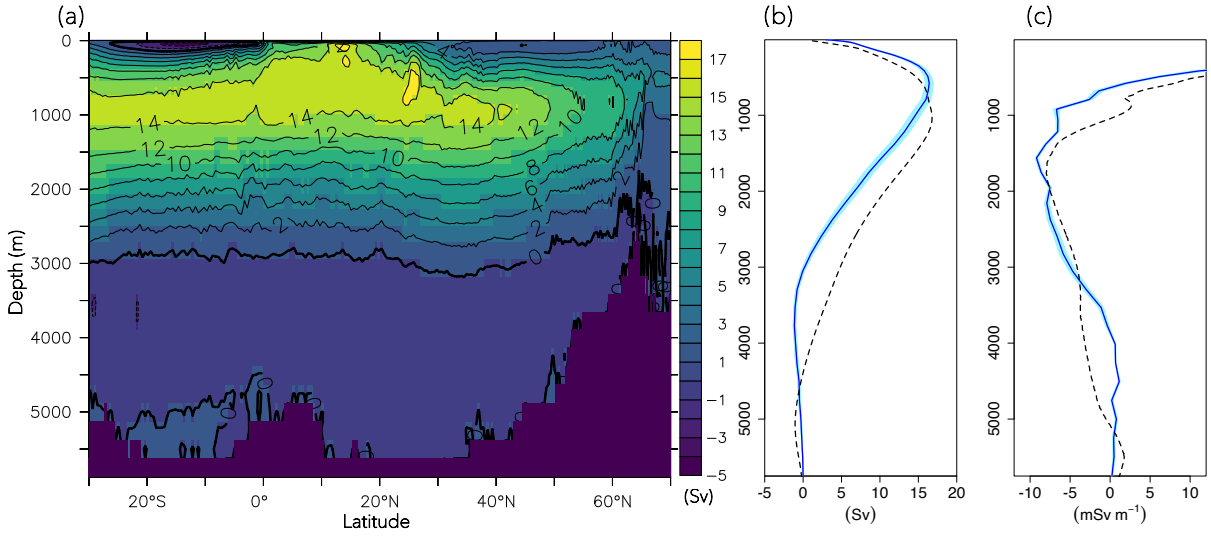

Figure 5. Atlantic meridional overturning stream function climatology over 2004 – 2014 of the *Hist* simulations. (a) Latitude–depth structure, (b) vertical profile at 26.5° N, and (c) z derivative of AMOC at 26.5° N. Blue lines and the shaded areas are modelled results, and dashed black lines are observational values from the RAPID array (McCarthy et al., 2015).

southern hemispheric Subtropical Front (Fig. 9b). In the ocean interior, NO_3 is removed by denitrification. Substantial rates of denitrification can be realised (depending on the supply of organic matter) when O_2 concentrations fall below a few mmol m^{-3} (Eq. A11, A16). Modelled denitrification occurs in the Atlantic Ocean, the northern Indian Ocean, the eastern tropical Pacific, and is most prominent in the Pacific (black contour lines in Fig. 9i – k). Globally integrated water column denitrification in the model amounts to 0.13 Pg N yr^{-1}, higher than observation-based estimates (ranging from 0.02 to 0.12 Pg N yr^{-1}, see section 3.3 below). It is likely that excessive denitrification contributes to some of the negative biases between 300 and 1000 m in the low latitude oceans (Fig. 9i – k, S5) that are not accompanied by similar negative biases in PO_4 (Fig. 6i – k).

The spatial pattern of dissolved inorganic carbon (DIC) and alkalinity (ALK) in general agree with observed patterns at the sea surface, but both show negative biases (Fig. 10b, Fig. 11b). In the interior, the biases turn positive below 3000 m for both DIC and ALK, which is most obvious in the Atlantic and the Pacific Oceans, similar to the patterns of PO_4 and NO_3. In the ocean, potential differences in CO_2 uptake between model and observations can contribute to DIC biases. Both DIC and ALK are affected by the remineralisation of detritus and the production of $CaCO_3$, via zooplankton egestion and plankton mortality in the surface layer and dissolution of $CaCO_3$ throughout the water column, respectively. There is a clear transition from a negative bias of DIC and ALK in the surface ocean to a positive bias in deep waters across all ocean basins except the Arctic where plankton activity is limited (Fig. 11h – l). This indicates that the e-folding export and dissolution of $CaCO_3$ (Sec. A2.2) might lead to an excessive transport of ALK (and DIC) to the deep ocean. The positive biases in DIC and ALK in the deep water might also indicate a too sluggish ventilation of deep waters, which is also consistent with the positive biases in PO_4 and NO_3, as well as the negative bias in O_2.

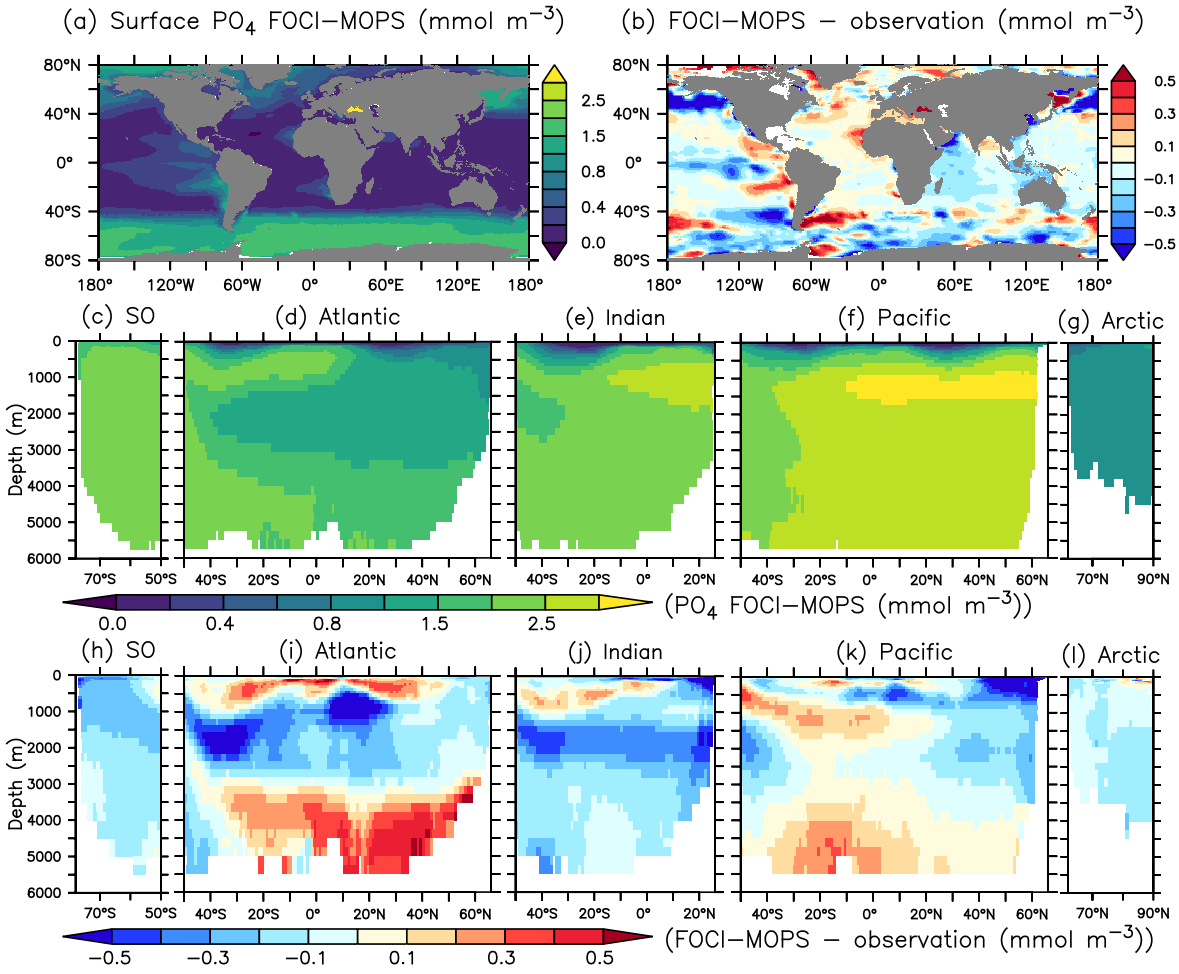

Figure 6. PO_4 climatology over 1972 – 2013 of the *Hist* simulations (panels a, c-g) and the difference model - observation (panels b, h-i). Observational data are from GLODAPv2.2016b which covers years 1972 to 2013 (Lauvset et al., 2016; Olsen et al., 2016). The order of the panels is the same as in Fig. 4

Typically, one standard deviation of distribution of the inorganic tracers are smaller than 10% of the mean value of the *Hist* ensemble simulations (Fig. S6–12). Areas with higher variation usually occur where vertical mixing is stronger, such as in high latitudes.

3.2.2 Spatial distribution of organic tracers in the surface

250 In FOCI-MOPS, the growth of phytoplankton is determined by temperature, light, and ambient NO_3 and PO_4 concentrations (Eq. A1 – A5). The distribution of phytoplankton (Phy) in the surface layer (∼6 m) overall agrees relatively well with observa-

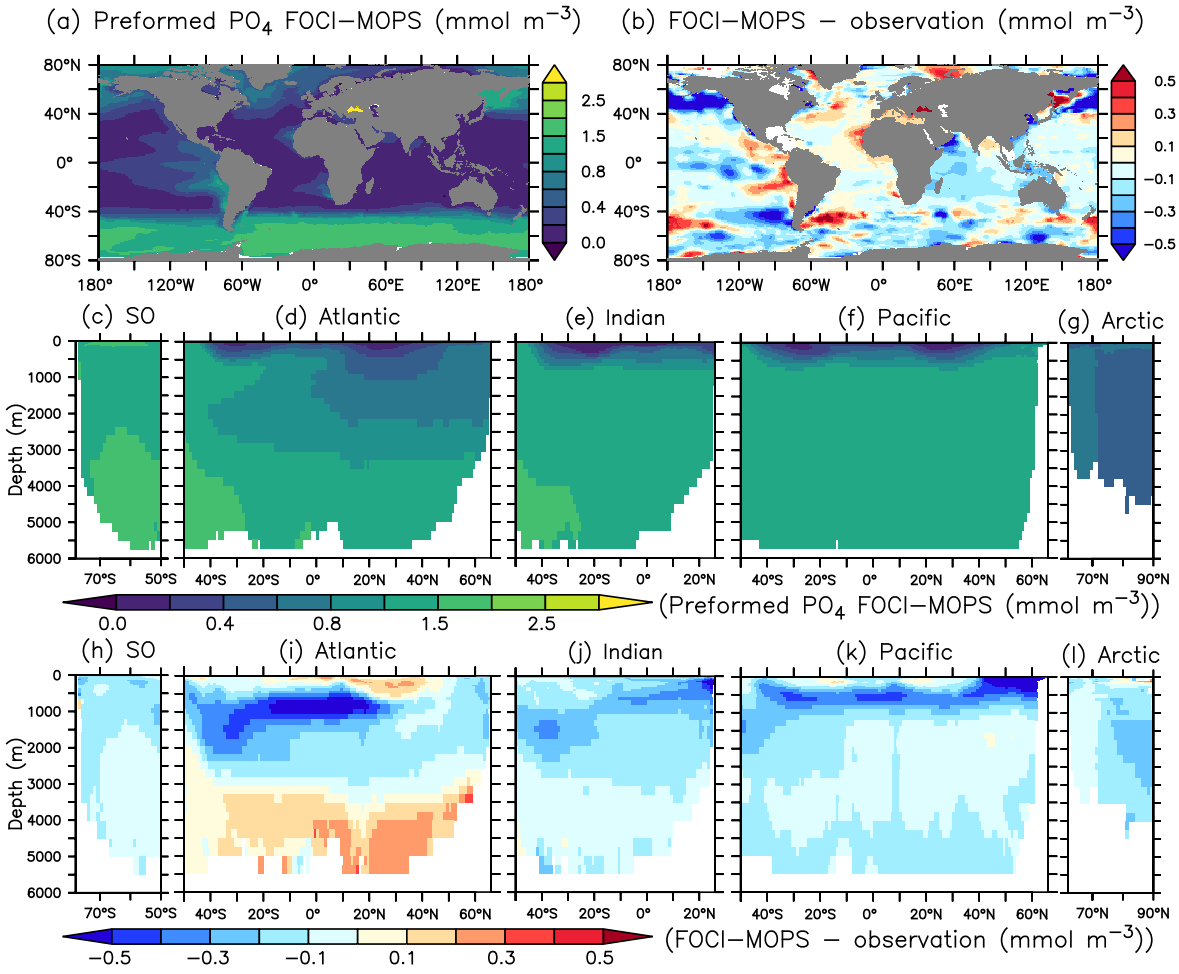

Figure 7. Preformed PO_4 climatology over 1972 – 2013 of the *Hist* simulations (panels a, c-g) and the difference with observations using GLODAPv2.2016b, which covers years 1972 to 2013 (Lauvset et al., 2016; Olsen et al., 2016) (panels b, h-i). Preformed PO_4 is estimated as PO_4 minus regenerated PO_4. The order of the panels is the same as in Fig. 4

tional estimates (Fig. 12a, e, and i), the most distinct discrepancies occur in coastal regions, where the observed phytoplankton concentrations often exceed 0.06 mmol P m^{-3}, but modelled phytoplankton do not (Fig. 12e). The difference might be due to the lack of terrestrial nutrient runoff in the current model version. Also, shelves are not well resolved with a 1/2° spatial
255 resolution, a typical bias of global models. In the open-ocean pelagic regions, however, the modelled phytoplankton is usually higher than the observation, which might be due to the missing iron limitation in the model. The higher phytoplankton biomass might also explain some of the low biases in PO_4 in the equatorial regions.

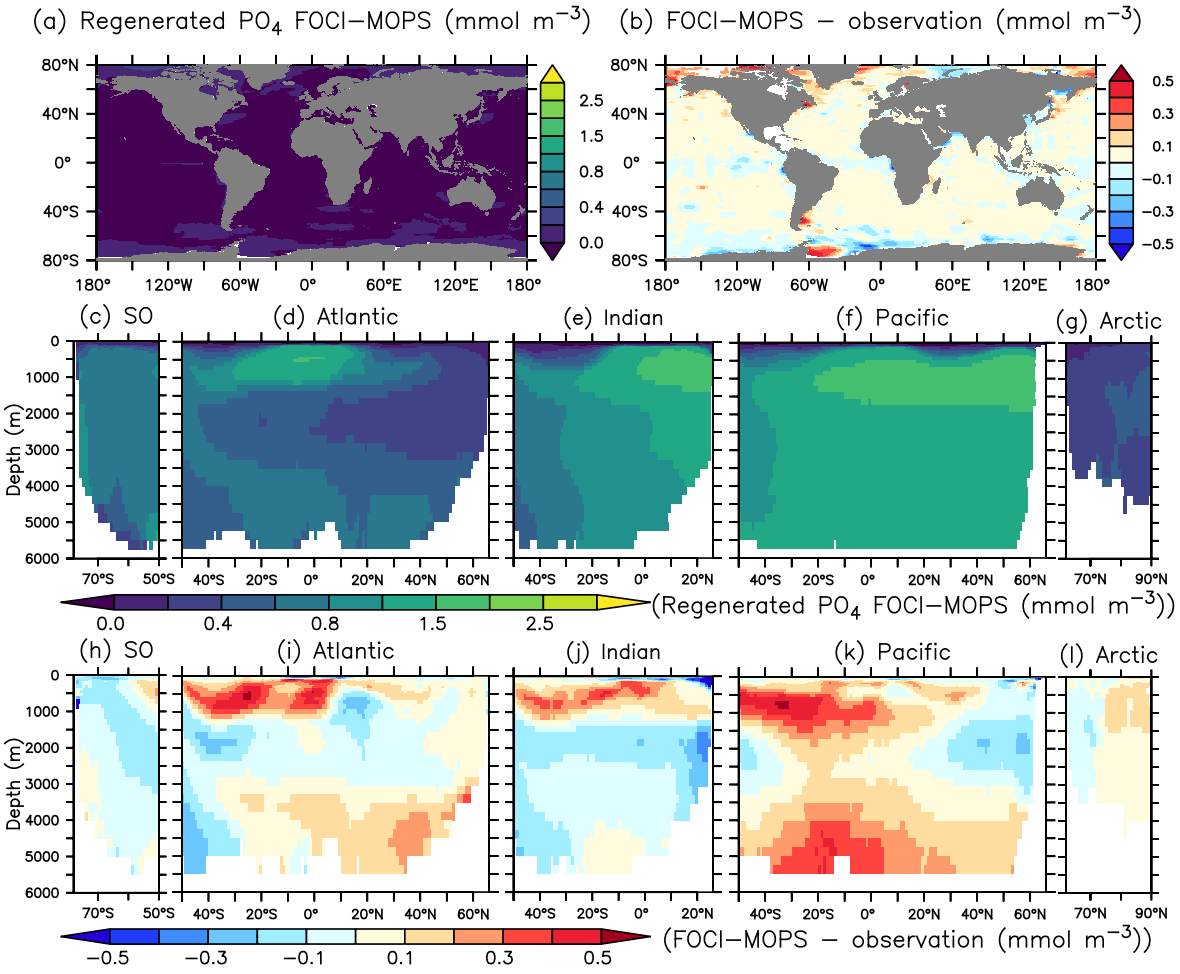

Figure 8. Regenerated PO_4 climatology over 1972 – 2013 of the *Hist* simulations (panels a, c-g) and the difference with observations using GLODAPv2.2016b, which covers years 1972 to 2013 (Lauvset et al., 2016; Olsen et al., 2016) (panels b, h-i). Regenerated PO_4 is estimated as apparent oxygen utilisation, see text. The order of the panels is the same as in Fig. 4

Zooplankton and particulate organic phosphorus (POP, sum of simulated phosphorus in detritus, phytoplankton, plus half of the zooplankton, see section B2.4 for further details) are generally closely associated with the presence of phytoplankton; their distributions largely correlate with those of phytoplankton in the model (Fig. 12b, c). While the large-scale pattern is similar, Zooplankton and POP are less homogeneously distributed than phytoplankton. For example, modelled phytoplankton biomass is around three-fold higher in the nutrient replete eastern tropical Pacific than in the oligotrophic gyres, while the same ratio can be over 10-fold for zooplankton. Modelled zooplankton are overestimated around the equator and the Southern Ocean around 40° S in the surface (0–100 m) (Fig.12j), where phytoplankton is overestimated as well (Fig.12i). Observations show much

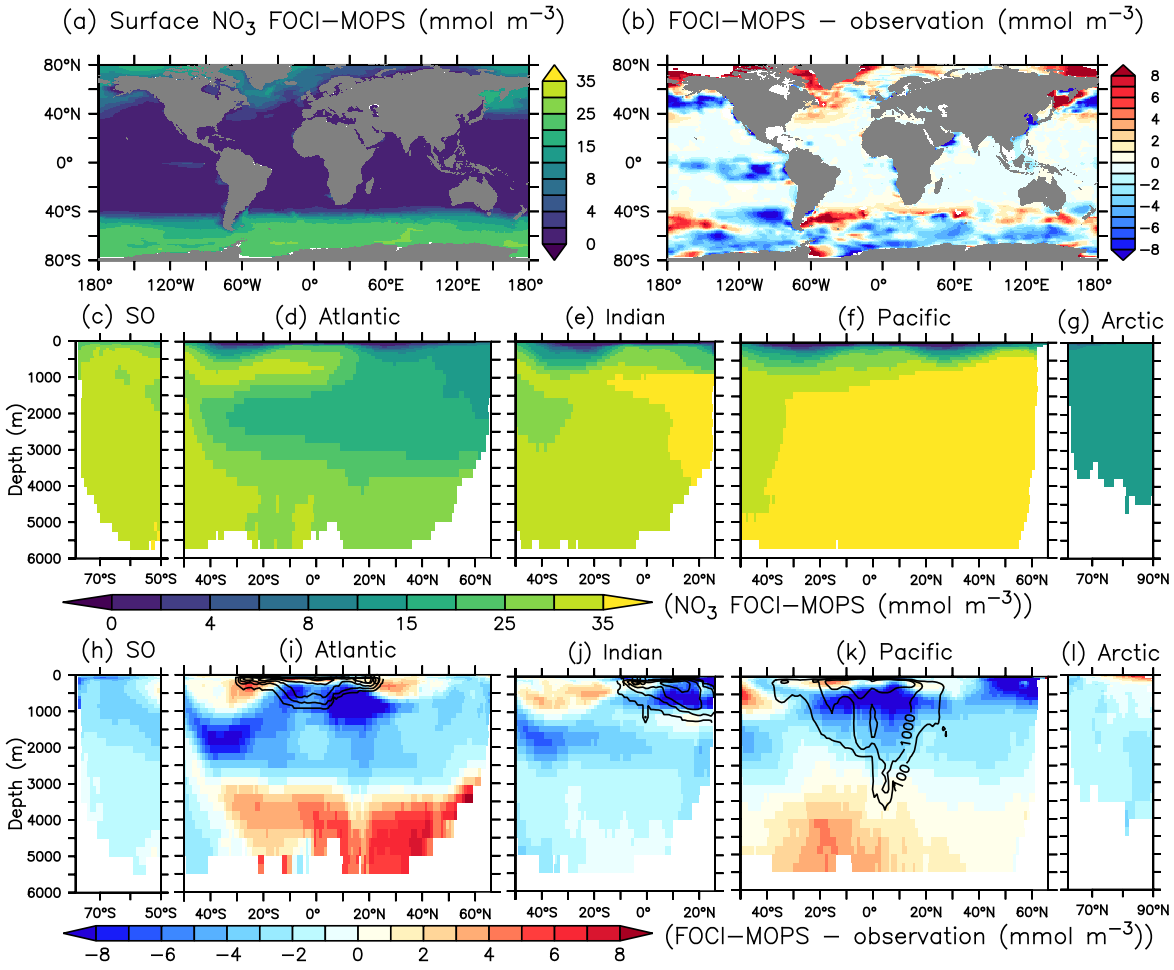

Figure 9. NO_3 climatology over 1972 – 2013 of the *Hist* simulations and the difference model - observation. Black contour lines represent zonally integrated denitrification rates (mmol N m^{-2} day^{-1}). Observational data are from GLODAPv2.2016b which covers years 1972 to 2013 (Lauvset et al., 2016; Olsen et al., 2016). Panels order as described in Fig. 4

higher POP at high latitudes than low latitudes in the surface (0–100 m)(Fig.12k), which is not captured by the model. Note that observational data of phytoplankton, zooplankton, and POP are from different types of estimates, therefore the observations do not necessarily correlate to each other as in the model. As dissolved organic phosphorus (DOP) is neutrally buoyant, it is controlled by ocean circulation in addition to the production and remineralisation. DOP is much lower in the deeper water than in the surface, therefore in upwelling regions such as the eastern equatorial Pacific, DOP is lower. Meanwhile, nutrients supply from the upwelling promotes the growth of phytoplankton and the production of POP. As a result, the spatial distribution of surface DOP in the model in general is negatively correlated with POP and is more homogeneously distributed (Fig. 12d).

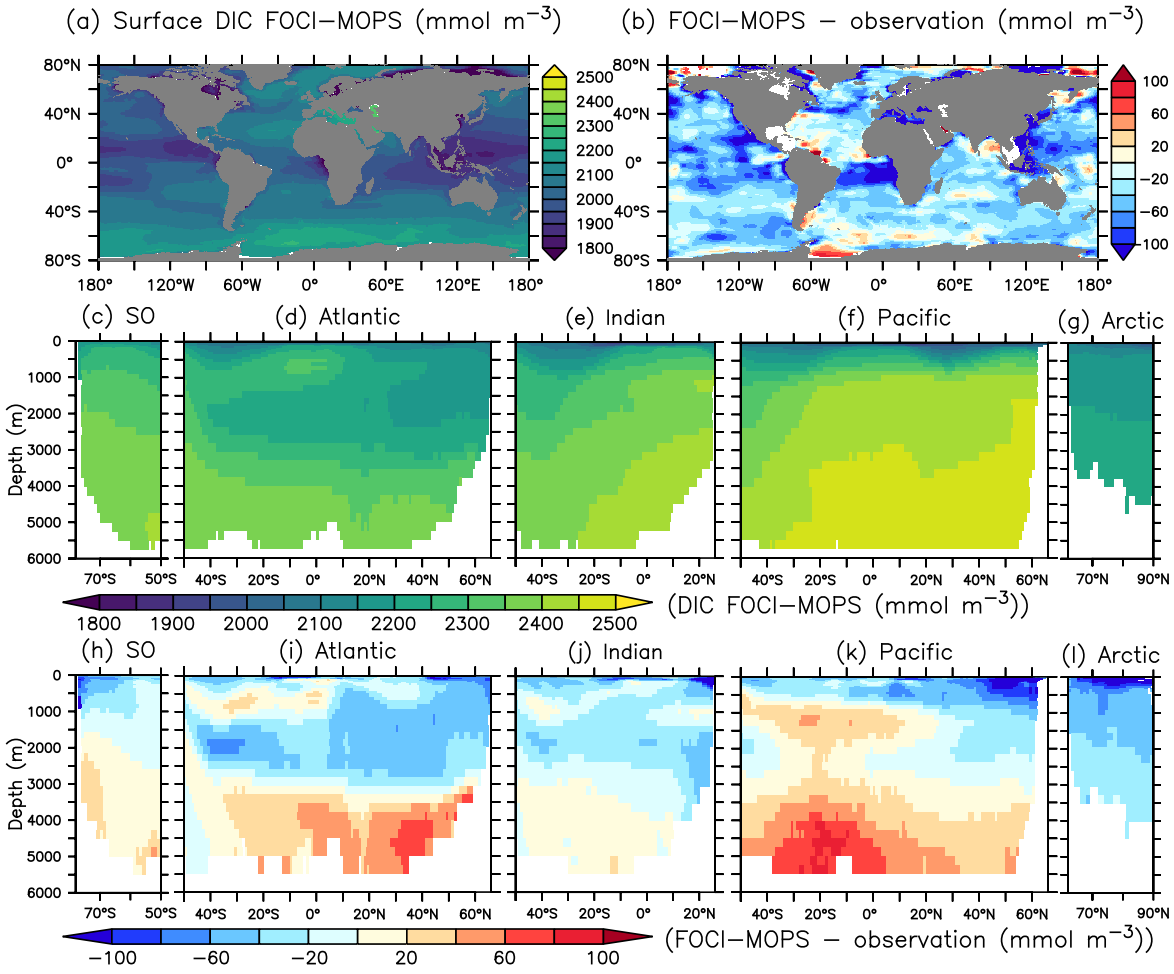

Figure 10. Dissolved inorganic carbon (DIC) of year 2002 of the *Hist* simulations and the difference model - observations. Observational data are sum of the preindustrial TCO_2 and the accumulated anthropogenic carbon in the year 2002 from GLODAPv2.2016b (Lauvset et al., 2016; Olsen et al., 2016). The order of panels is the same as in Fig. 4

Observations of DOP are very sparse but suggest that DOP tends to be overestimated in the model. This may indicate a too long DOP remineralisation timescale; however, a shorter timescale may lead to an even stronger bias in surface phosphate concentrations (Fig. 12). Alternatively, changing the partitioning between DOP and POP production (e.g., via parameter σ_{DOP} in eqns. A9 and A10), together with modified POP sinking speed and remineralisation could potentially improve DOP without negative effects on other (surface) components. Further investigations regarding the simultaneous fit of MOPS to all inorganic and organic tracers are currently underway.

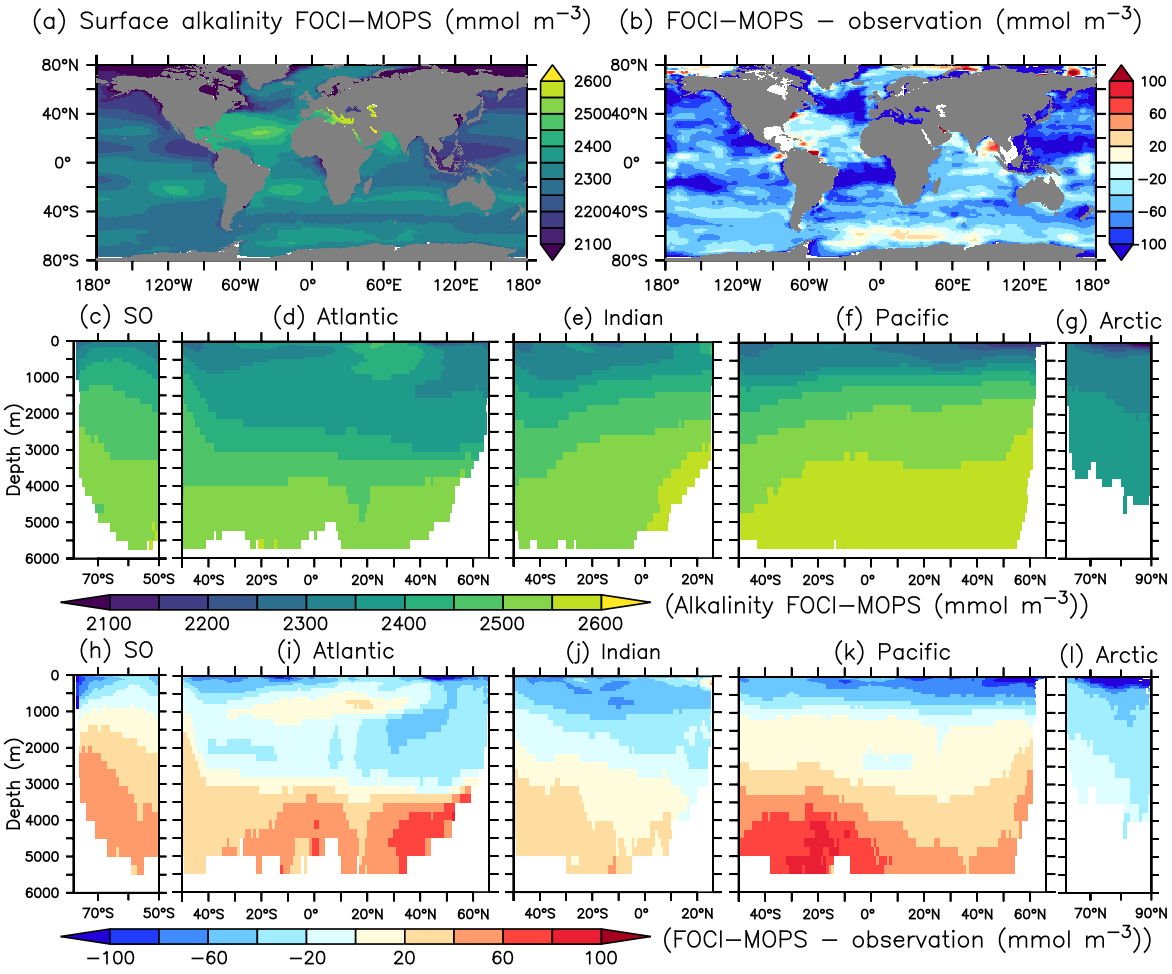

Figure 11. Alkalinity (ALK) climatology over 1972 – 2013 of the *Hist* simulations and the difference model - observations. Observational data are from GLODAPv2.2016b which covers years 1972 to 2013 (Lauvset et al., 2016; Olsen et al., 2016). The order of panels is the same as in Fig. 4

Similar to the inorganic tracers, one standard deviation of distribution of the organic tracers are smaller than 10% of the mean value of the *Hist* ensemble simulations (Fig. S13).

3.2.3 Statistical performance of the simulated inorganic and organic tracers

The correlation coefficient r, standard deviation σ_{M} and centred root-mean-squared-error RMSE' (RMSE minus global bias) of modelled nutrients and oxygen shows a very good match compared to the non-interpolated observations (Table 2, Fig. 13), although nutrients are biased somewhat low, especially at the surface (0 – 100 m), which is the only depth range where oxygen

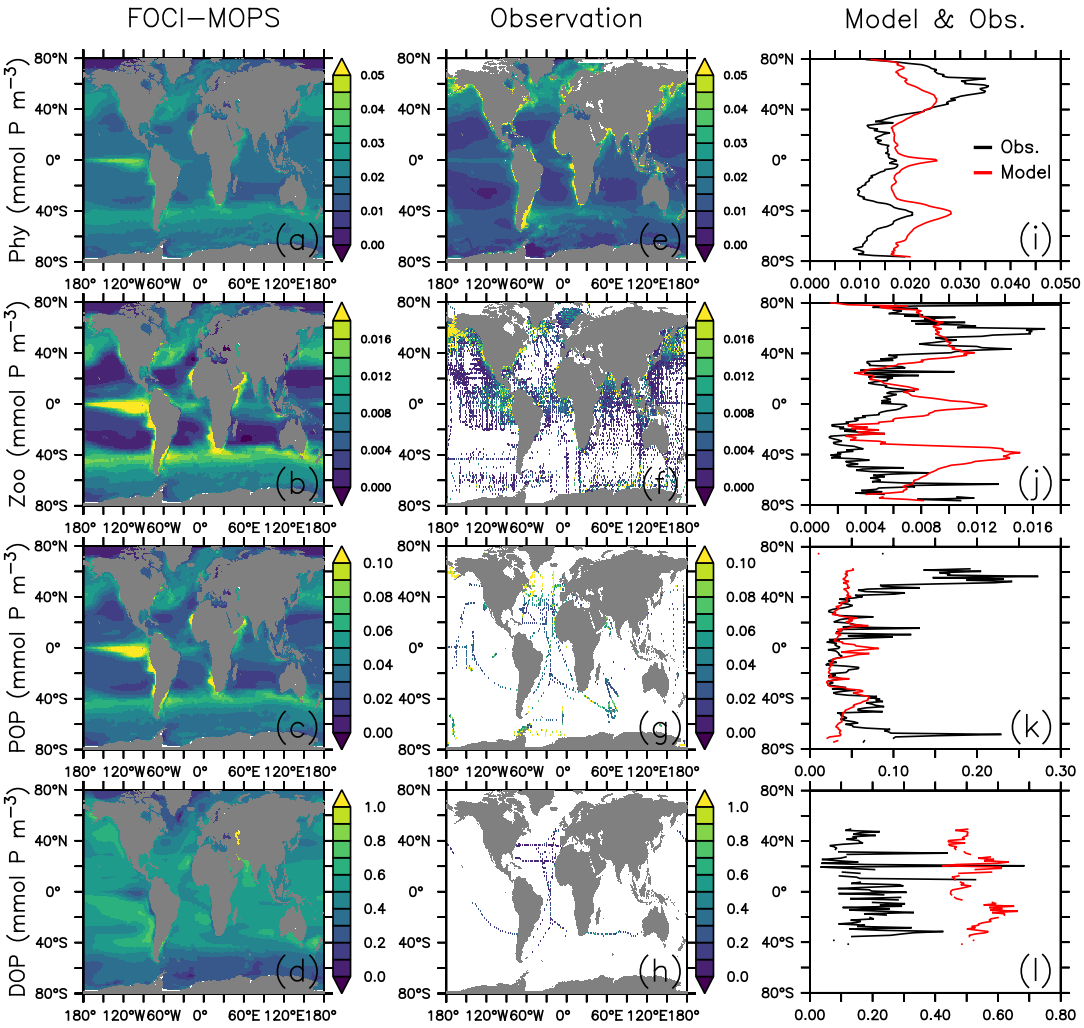

Figure 12. Organic tracer concentrations (first layer (∼6 m) of phytoplankton (Phy) , 0–100 m of zooplankton (Zoo) , particulate organic phosphorus (POP), and dissolved organic phosphorus (DOP)) climatology over 2005 – 2014 of the *Hist* simulations (a – d), observations (e – h), and the zonally averaged values (i – l). In the zonally averaged panels model results are subsampled according to the availability of observations. Observational data of Phy, Zoo, and POP are derived from chlorophyll (MODIS-Aqua; Melin, 2013), mesozooplankton (MAREDAT; Moriarty and O'Brien, 2013), and POM (Martiny et al., 2014), respectively. Observations of DOP are from multiple published (Torres-Valdés et al., 2009; Moutin et al., 2008; Landolfi et al., 2016; Yoshimura et al., 2007) and unpublished (Landolfi, unpubl.) data sets. See sections B2.2, B2.3, B2.4, and B2.5 for details of the observations.

shows a high bias (note color shading of symbols in Fig. 13). The modelled ALK and DIC are slightly biased low above 2000 m. The modelled surface ALK averaged over 1972 to 2013 is 2286±1 mmol m^{-3} and surface DIC averaged over 1870 to 1899 (pre-industrial DIC) is 1985±0 mmol m^{-3}. They are lower than the values among CMIP5 models (surface ALK and pre-industrial DIC are 2365 – 2500 and 2050 – 2170 mmol m^{-3}, respectively; Oka, 2020), but are only slightly lower than the observations (surface ALK and pre-industrial DIC are 2362 and 2019 mmol m^{-3}, respectively; Lauvset et al., 2016; Olsen et al., 2016). Note that the low bias in the full-domain ALK here is contrary to a higher inventory when compared to the initial state (Fig. 2 and 3). The low bias against individual (non-interpolated) data results from the fact that more observations are located in the upper 2000 m, where the model underestimates ALK concentrations. Compared to global model assessments of CMIP5 models with similar metrics evaluated by Ilyina et al. (2013), Séférian et al. (2013), and Kwiatkowski et al. (2014), the model performs well (Table 2) with respect to dissolved inorganic tracers.

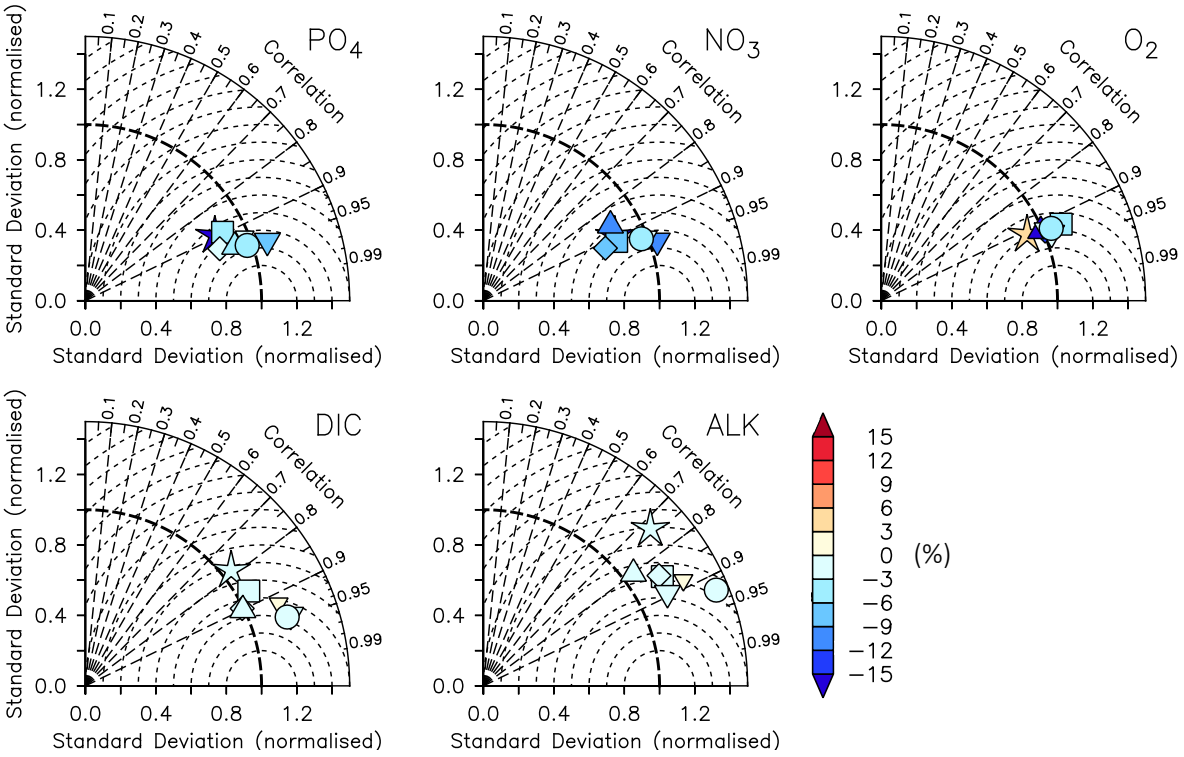

Figure 13. Taylor diagrams for phosphate (PO_4), nitrate (NO_3), oxygen (O_2), dissolved inorganic carbon (DIC) and alkalinity (ALK) (left to right). Colours indicate model bias (relative to observations; in percent). The model is subsampled according to the availability of observations. Observational data are from GLODAPv2.2016b (Lauvset et al., 2016; Olsen et al., 2016). Symbols indicate different vertical domains: Star: 0-100m; Square: 100-200 m; Diamond: 200-500 m; Triangle: 500-1000 m; Delta: 1000-2000 m; Small delta: 2000-5000 m; Circle: full domain.

Table 2. Correlation coefficient r, normalised standard deviation $\sigma_{\mathrm{M}}/\sigma_{\mathrm{O}}$, global bias normalised by observed mean (in squared brackets: non-normalised bias, in μg Chl L^{-1} for phytoplankton, and in mmol m^{-3} for all other tracers), and Bhattacharyya distance (BD) of experiment *Hist* presented in this study, and from studies by Ilyina et al. (2013, historical run in "MR" model configuration, Table 5; "I2013"), Séférian et al. (2013, one biogeochemical model with three different circulations,Table 3; "S2013") and Kwiatkowski et al. (2014, six biogeochemical models in one circulation, Table 3; "K2014"). Except for chlorophyll, the values in FOCI-MOPS are from comparison with non-interpolated data from GLODAPv2.2016b (Lauvset et al., 2016; Olsen et al., 2016). Round brackets are introduced for distinguishing hyphen and negative signs. For all model studies we report metrics for the surface (here refers to 0-100m); additionally, for the metrics by Ilyina et al. (2013) we show the range over five different depth levels (surface, 100 m, 500 m, 1000 m, and 3000 m) in the "all domains" column. For the "all domains" column in this study we show the range over seven different vertical domains (0-100 m, 100-200 m, 200-500 m, 500-1000 m, 1000-2000 m, 2000-5000 m, 0-8000 m). For metrics by Séférian et al. (2013) we report the range over three different circulations, and for metrics by Kwiatkowski et al. (2014) the range over five different models. Note that except for the Bhattacharyya distance all metrics of *Hist* have been calculated from volume-weighted properties. *: computed from phosphorus units via a C:Chl according to Sathyendranath et al. (2009).

Metric	Tracer	I2013 ("MR")		S2013	K2014	This study	
		surface	all domains	surface	surface	surface	all domains
r	PO_4	0.94	0.83-0.94	0.85-0.91	–	0.89	0.89-0.96
	NO_3	0.87	0.82-0.95	0.87-0.94	0.79-0.94	0.89	0.85-0.95
	O_2	0.99	0.89-0.99	–	–	0.91	0.91-0.94
	DIC	0.93	0.76-0.94	–	0.65-0.93	0.78	0.78-0.95
	ALK	0.79	0.25-0.92	–	0.58-0.91	0.72	0.72-0.92
	Chl	–	–	0.38-0.43	0.04-0.50	0.36	–
$\sigma_{\mathrm{M}}/\sigma_{\mathrm{O}}$	PO_4	0.77	0.77-1.61	–	–	0.83	0.82-1.08
	NO_3	0.80	0.80-1.10	–	0.95-1.21	0.84	0.75-1.04
	O_2	1.02	1.02-1.26	–	–	0.91	0.91-1.11
	DIC	1.09	1.09-2.69	–	0.96-1.18	1.06	0.99-1.23
	ALK	1.26	1.12-3.08	–	0.88-1.19	1.31	1.08-1.43
	Chl	–	–	–	0.40-2.65	0.41	–
Bias (rel., %) [Bias]	PO_4	-27.17	-27.2-(-8.3)	[-0.3-0]	–	-17.5 [-0.10]	-17.5-(-2.2)
	NO_3	-2.97	-24.7-8.1	[-1.3-4.9]	–	-18.7 [-1.27]	-18.7-(-1.7)
	O_2	0.26	-3.8-3.2	–	–	3.0	-21.0-3.0
	DIC	3.34	3.3-4.7	–	–	-2.7	-2.7-0.1
	ALK	3.28	3.3-4.8	–	–	-2.7	-2.7-0.8
	Chl	–	–	[-0.1]	–	[*0.1*]*	–
BD	PO_4	0.05	0.04-0.38	–	–	0.03	0.03-0.09
	NO_3	0.04	0.04-0.36	–	–	0.04	0.04-0.14
	O_2	0.09	0.08-0.16	–	–	0.04	0.01-0.07
	DIC	0.36	0.09-0.43	–	–	0.07	0.02-0.19
	ALK	0.69	0.12-0.69	–	–	0.13	0.09-0.34

The model fit worsens for the organic tracers, with a correlation coefficient between 0.11 (DOP) and 0.42 (POP), and generally a too low spatial variance (between 41 and 61% of the observations; Table B2 and Fig. 14). Except for POP, organic tracers are biased high, and RMSE and RMSE' are large. Thus, the statistical metrics indicate a lower performance of the model for the organic tracers chlorophyll, zooplankton, DOP and POP. Nevertheless, the results for phytoplankton/chlorophyll are in line with earlier global model studies (Table 2). Note also that the uncertainty of the observational estimates of organic tracers is larger compared to inorganic tracers, the in-situ observations are sparse in space and time, with sampling biases, e.g., towards summer and with less high latitude observations (see also Appendix B2.).

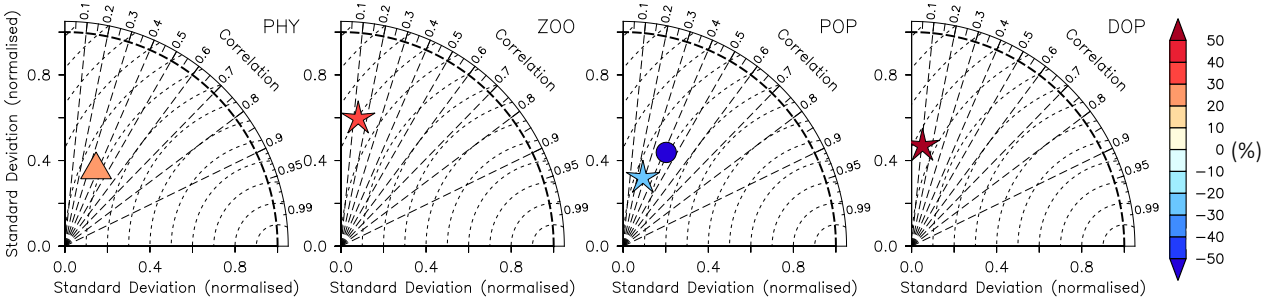

Figure 14. Taylor diagrams for phytoplankton (PHY), zooplankton (ZOO), particulate organic phosphorus (POP) and dissolved organic phosphorus (DOP) as shown in Fig. 12 (left to right). Colours indicate model bias (relative to observations; in percent). Observational data of Phy, Zoo, and POP are derived from chlorophyll (MODIS-Aqua; Melin, 2013), mesozooplankton (MAREDAT; Moriarty and O'Brien, 2013), and POM (Martiny et al., 2014), respectively. Observations of DOP are from multiple published (Torres-Valdés et al., 2009; Moutin et al., 2008; Landolfi et al., 2016; Yoshimura et al., 2007) and unpublished (Landolfi, unpubl.) data sets. See sections B2.2, B2.3, B2.4, and B2.5 for details of the observations. The model is subsampled according to the availability of observations. Symbols indicate different vertical domains: Triangle: surface (∼6 m); Star: 0-100 m; Circle: full domain (POP only).

Even if a biogeochemical model component is dynamically correct, a slight distortion in the physical model (e.g., a slight spatial shift in ocean current) can cause a large RMSE, and thereby induce a large model error. To account for such effects we have calculated three metrics that do not rely on the exact spatial pattern of tracers, but on the concentration distribution, namely the Bhattacharyya distance (BD) (Bhattacharyya, 1946), which evaluates the similarity between observed and simulated frequency distributions of tracers, the Hellinger distance (HD) (Hellinger, 1909), which is related to BD via $BD = -\ln(1 - HD^2)$, and the $L1$ norm, which evaluates the absolute difference between observed and simulated distributions. For all three metrics, smaller model-data misfit is associated with larger area of overlap between the two distributions, which yields smaller values (see Appendix B3). Figures 15 and 16 show examples for the distributions of inorganic and organic tracers, and Table B2 lists the metrics for different tracers. Applying these metrics, it is evident that most organic tracers (phyto- and zooplankton and POP), despite suffering from a large error with respect to r and RMSE, in general reflect the observed distribution (Fig. 16), and thus exhibit values for, e.g., BD which are in the same range as those of inorganic tracers. Only the strong overestimate

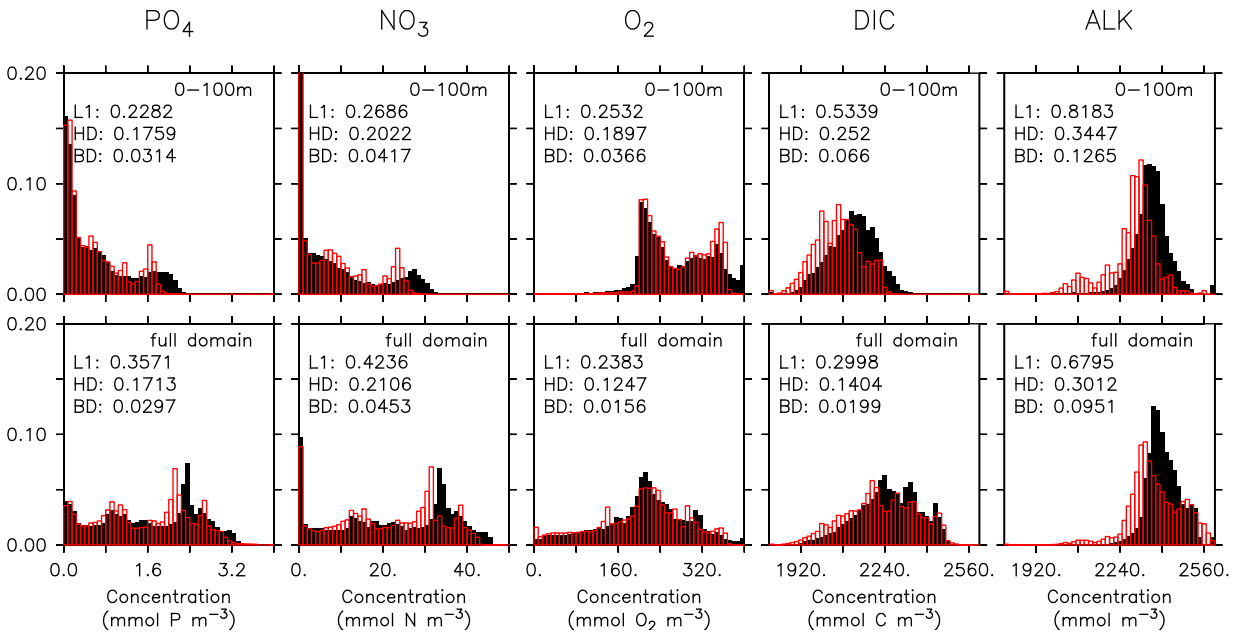

Figure 15. Frequency distribution of phosphate (PO_4), nitrate (NO_3), oxygen (O_2), DIC and alkalinity (left to right) from observations (black filled bars) and model (red bars) for the surface (0-100 m, top) and the full model domain (bottom). Numbers denote three different metrics for the similarity of the distributions, namely $L1$ (Equation B3), HD (Equation B2) and BD (Equation B1). Observational data are from GLODAPv2.2016b. The data cover years 1972 to 2013 except for DIC, which represents for the year 2002 (Lauvset et al., 2016; Olsen et al., 2016).

of DOP by the model is also reflected in BD. Here the model shows, for all metrics, a much higher misfit than for any other tracers.

To summarise, in terms of tracer distributions the performance of MOPS in FOCI is comparable to other global models, and even generally better with respect to inorganic tracers. The fit deteriorates with regard to the organic components in case of plankton and POP, and with a high bias for DOP.

3.3 Globally integrated biogeochemical fluxes and their spatial patterns

3.3.1 Oceanic biogeochemical fluxes

We average the globally integrated biogeochemical fluxes simulated by FOCI-MOPS over the time period 2005 to 2014 and over the ensemble of three *Hist* simulations (Table 3). Overall, primary production (37.8 Pg C y^{-1}), export production, that is the sinking of detritus at 100 m (6.8 Pg C y^{-1}), the flux of detritus at 2000 m (0.35 PgC y^{-1}), burial of detritus that sank to the bottom of the ocean (0.34 PgC y^{-1}), and N_2 fixation (0.12 Pg N y^{-1}) are within the range of observation-based estimates.

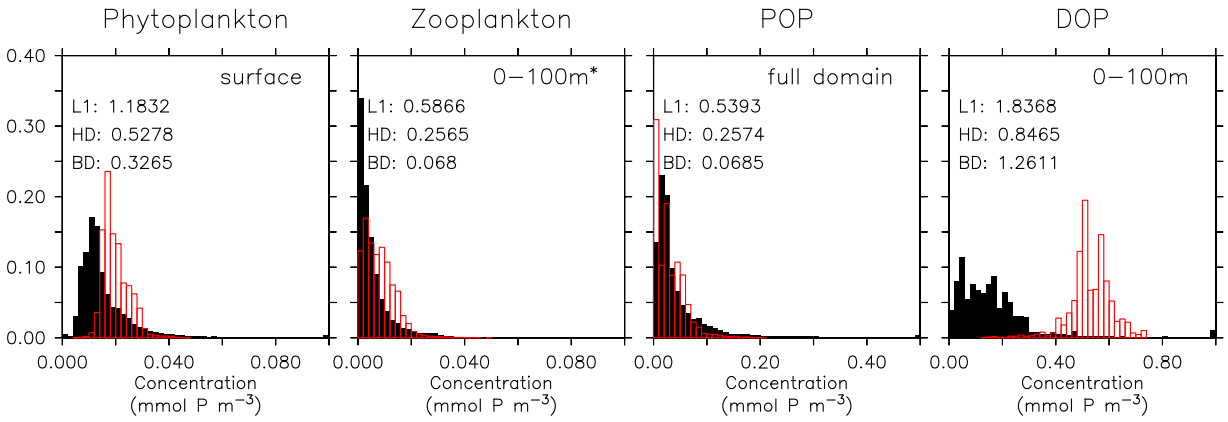

Figure 16. Frequency distribution of surface phytoplankton, zooplankton (0-100 m), POP (full domain) and DOP (0-100 m). Observational data of Phy, Zoo, and POP are derived from chlorophyll (MODIS-Aqua; Melin, 2013), mesozooplankton (MAREDAT; Moriarty and O'Brien, 2013), and POM (Martiny et al., 2014), respectively. Observations of DOP are from multiple published (Torres-Valdés et al., 2009; Moutin et al., 2008; Landolfi et al., 2016; Yoshimura et al., 2007) and unpublished (Landolfi, unpubl.) data sets. See sections B2.2, B2.3, B2.4, and B2.5 for details of the observations.The model is subsampled according to the availability of observations. Colours and numbers as described in Fig. 15.

$CaCO_3$ production (0.77 Pg C y^{-1}) is lower than previous observation-based estimates (0.8–4.7 Pg C y^{-1}). Water column denitrification (0.13 Pg N y^{-1}) is slightly higher than observational estimates.

The highest annual primary production occurs in the eastern equatorial Pacific Ocean and some coastal regions (> 1000 mg C m^{-2} day^{-1}, Fig. 17a). In the subtropical oligotrophic gyres, it is typically lower than 200 mg C m^{-2} day^{-1}. The spatial distributions of export production at 100 m and $CaCO_3$ production (Fig. 17b, c) are similar to that of primary production, suggesting that the latter is largely driving the former. The spatial pattern of the flux of sinking detritus at 2000 m is less similar to that of primary production due to the effects of advection and mixing (Fig. 17d). The distinct high flux at 2000 m depth in the eastern Pacific is partly due to the low O_2 levels between surface and 2000 m depth mentioned earlier. Regions of elevated flux of detritus largely overlap with O_2 concentrations below 36 mmol O_2 m^{-3}, which is the threshold for anaerobic remineralisation in the model. Denitrification is shaped by low O_2 levels associated with high primary production, consequent detritus flux, and sluggish ventilation, particularly in the so-called shadow zones along the eastern margins of the subtropical oceans (Fig. 17e). These biological and physical effects together result in the most pronounced water column denitrification in the eastern tropical Pacific, which accounts for 71% of the global denitrification rate in our model, which is within the range that was derived from nitrogen gas measurements (70 – 88 %; DeVries et al., 2012). Due to temperature limitation, N_2 fixation occurs mostly between 40° N and 40° S in the model. In the model, 60% of N_2 fixation occurs in the Pacific Ocean, in agreement, though at the lower end, of observational estimates that ranges between 60 – 80 % (Luo et al., 2012). Variation (one

Table 3. Primary production, export production, flux of detritus at 2000 m, global burial, $CaCO_3$ production (Pg C y^{-1}), N_2 fixation and water column denitrification (Pg N y^{-1}) in *Hist* simulations (average over years 2005 to 2014) and observation-based estimates.

Fluxes	FOCI-MOPS (This study)	Observation-based estimates	References
Primary Production	37.8±0.1	35.6–77.4	Carr et al. (2006)
		35.2	Honjo et al. (2008)
		51–65	Buitenhuis et al. (2013)
Export Production	6.8±0.0	6–13.2	Dunne et al. (2007)
		1.8–4.6	Lutz et al. (2007)
		5.7	Honjo et al. (2008)
		5.89	Siegel et al. (2014)
Flux, 2000 m	0.35±0.00	0.12–0.28	Dunne et al. (2007)
		0.43	Honjo et al. (2008)
		0.33	Guidi et al. (2015)
Global Burial	0.34±0.00	0.15	Muller-Karger et al. (2005)
		0.59	Wallmann (2010)
$CaCO_3$ production	0.77±0.00	0.8–1.4	Iglesias-Rodriguez et al. (2002)
		1.3–1.9	Balch et al. (2007)
		0.9–1.1	Lee (2001)
		4.7	Buitenhuis et al. (2019)
N_2 fixation	0.121±0.000	0.094–0.175	Eugster and Gruber (2012)
		0.128–0.146	Luo et al. (2012)
		0.195–0.35	Somes et al. (2013)
		0.126–0.223	Wang et al. (2019)
Denitrification	0.125±0.002	0.02–0.12	Bianchi et al. (2012)
		0.039–0.066	Eugster and Gruber (2012)
		006–0.072	DeVries et al. (2012)
		0.05-0.077	DeVries et al. (2013)
		0.065–0.08	Somes et al. (2013)
		0.056–0.073	Wang et al. (2019)

standard deviation) among the three *Hist* simulations of the biogeochemical fluxes are smaller than 10% of the mean fluxes (Fig. S14).

3.3.2 Air-sea exchange of carbon

Figure 18 shows the ocean pCO_2 and the air-sea CO_2 fluxes (positive downwards) in the *Hist* simulations for the 2005 – 2014 period, as well as the observation-based estimate for the same period (Landschützer and Bakker, 2017). In general, sea surface

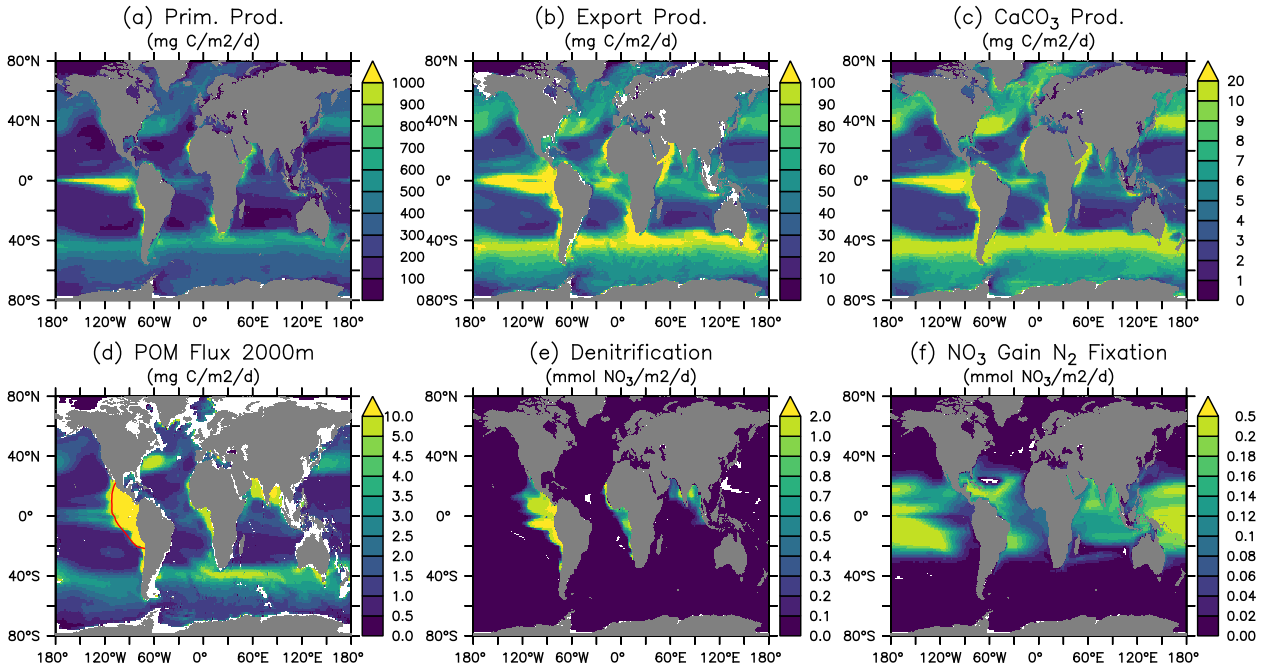

Figure 17. Patterns of primary production, export production at 100 m, $CaCO_3$ production, flux of detritus at 2000 m, denitrification, and N_2 fixation in the *Hist* simulations averaged over 2005–2014. Red contour line in (d) indicates O_2 level of 36 mmol O_2 m^{-3}. Values are column-integrated except for the export production and the flux of detritus.

pCO_2 and air-sea CO_2 flux are affected by various biological and physical processes (Dong et al., 2016; Qu et al., 2022). For example, a too high phytoplankton production could result in a too low DIC and leads to an underestimate of the magnitude of negative CO_2 flux (outgassing). Our model results are consistent with such a scenario in the eastern equatorial Pacific, north Pacific, and parts of the Southern Ocean. The too high phytoplankton production and resultant underestimated DIC could be due to the lack of Fe limitation, as we can see surface PO_4 and NO_3 are underestimated in the same regions. On the other hand, physical factors such as sea surface temperature (SST) (Fig. 19, and see Fig.S16 for the standard deviation among the *Hist* simulations) can also affect pCO_2 and CO_2 flux. Overestimated SST can be associated with positive pCO_2 and negative air-sea CO_2 flux biases. Those biological and physical factors result in complex patterns in the pCO_2 and CO_2 flux, and often it is difficult to quantify the contribution of individual factors. On top of these factors, our model-data comparison is for the period of present-day data (2005–2014). Therefore, the mismatches in pCO_2 and CO_2 uptake can be from two components, the mismatch inherited from the spinup at a steady state, and the mismatch in the uptake of anthropogenic carbon accumulated during the historical period. Since there is no pre-industrial observations, we cannot differentiate the contributions from each part. Nevertheless, the modelled large scale pattern of CO_2 fluxes/uptake agrees with observations, and the biases in air-sea

CO_2 fluxes are in the range of other Earth System Models participating in the CMIP5 intercomparison (Dong et al., 2016). When zonally averaged, much of the biases are averaged out, and both ocean pCO_2 and air-sea CO_2 fluxes in FOCI-MOPS match the observations rather well (Fig. 18d, h).

At high latitudes, the variation in the ocean pCO_2 and the air-sea CO_2 fluxes are usually higher (Fig. S15), due to the physical mixing is stronger and with higher uncertainty.

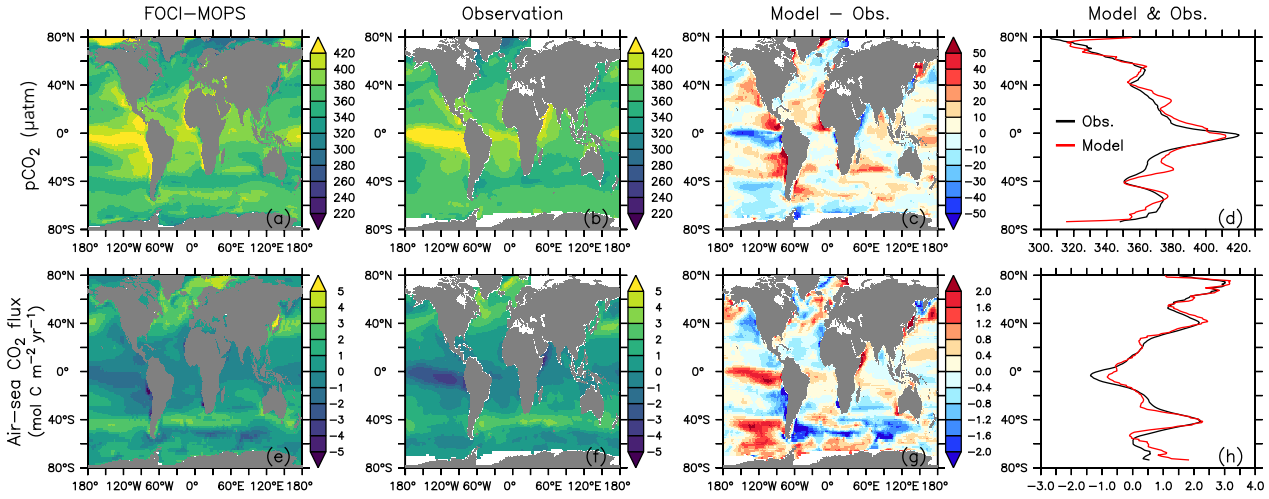

Figure 18. Ocean pCO_2 and air-sea CO_2 fluxes (positive downwards). (a) and (e) *Hist* ensemble mean averaged over 2005 to 2014. (b) and (f) are observations (Landschützer and Bakker, 2017) over the same time period. (c) and (g) are model biases with respect to the observations, and (d) and (h) are zonally averaged values of observations and model results where observations are available.

3.4 Response to increasing atmospheric CO_2

3.4.1 Atmospheric CO_2, air-sea CO_2 flux, surface air temperature anomaly, and ocean heat content anomaly

Atmospheric CO_2 in *ESM-piControl* drifts slowly from 286.0±0.4 ppm between 1850–1879 to 287.1±0.7 ppm between 2005–2014, with an average of 286.4±0.14 ppm over the whole period, which is 2 ppm above the prescribed concentration in *piControl*. During the historical period, atmospheric CO_2 in *ESM-Hist* increases from 286.1±0.46 ppm in 1850 to 410.1±2.33 ppm in 2014, slightly higher than the historical value of 397.5 ppm (Fig. 20a). According to these results, the pre-industrial ocean in FOCI-MOPS acts as a small net CO_2 source to the atmosphere: The mean global oceanic CO_2 loss in *piControl* and *ESM-piControl* during the simulation period are 0.07±0.01 and 0.05±0.01 Pg C yr^{-1}, respectively. In the historical simulations, the globally integrated air-sea CO_2 flux gradually increases between 1850 to 1960 along with increasing anthropogenic CO_2 perturbation. After 1960, the rate of increase accelerates, and the flux reaches 2.11±0.10 and 2.21±0.14 Pg C yr^{-1} over 2005

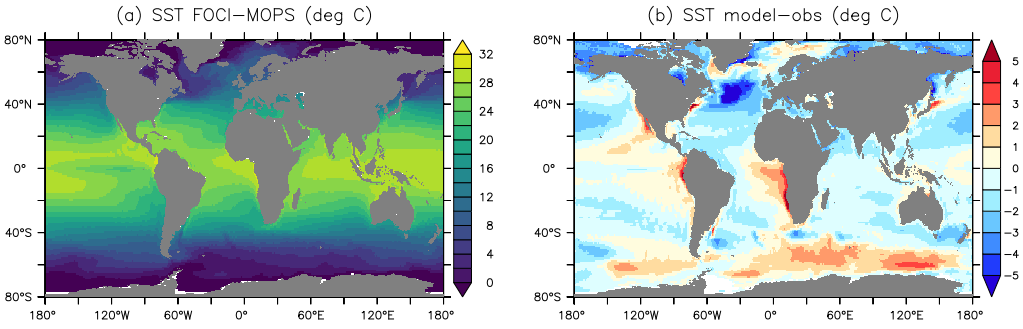

Figure 19. Sea surface temperature (SST). (a) *Hist* ensemble mean averaged over 2005 to 2014. (b) The difference between model results and observations (HadISST, Rayner et al., 2003).

– 2014 period in *Hist* and *ESM-Hist*, respectively, both are slightly lower than the 2.34 Pg C yr^{-1} estimated by the Global Carbon Project (Friedlingstein et al., 2020, see summary tab) (Fig. 20b).

The cumulative air-sea CO_2 flux (positive downwards) from 1850 to 2014 in *ESM-Hist* amounts to 139±2 Pg C, which is 10 Pg C higher than that of *Hist*, with most of the difference building up over the time period 1850 to 1994 (Table 4). In the land model JSBACH, the air-land carbon flux is fulfilled by the NPP (net primary productivity), which is determined by the difference between photosynthesis and autotrophic respiration of vegetation. The vegetation carbon losses to grazing by herbivores, litter production, and crop harvest, and is consequently transported back to the atmosphere. We have followed Liddicoat et al. (2021) and calculated the compatible emission in the historical simulations. The cumulative compatible emission from 1850 to 2014 in the *Hist* simulations is 367±3 Pg C, lower than the lower limit of observation (380 Pg C), but agrees with the mean of CMIP6 models when excluded the highest two model values (367 Pg C, Liddicoat et al., 2021). The underestimated cumulative compatible emission implies missing processes including land carbon uptake during the Second World War, during that period land use might not be correctly accounted for in the model forcing (Bastos et al., 2016). Despite the different cumulative fluxes until 1994, the cumulative CO_2 flux is about the same (25±1 Pg C) over 1994 to 2007 in *Hist* and *ESM-Hist* runs (Table 4). Both *Hist* and *ESM-Hist* simulate lower cumulative CO_2 fluxes when compared with observations, and are comparable to or slightly lower than CMIP6 models (Table 4). The cumulative fluxes over 1994 to 2007 are within the range of observations. The latitudinal distributions of cumulative CO_2 fluxes and carbon storage in FOCI-MOPS are consistent with those of CMIP6 models (Fig. 21). The highest CO_2 uptake between 40–65°S is associated with the wind-driven upwelling, which brings deep water with low anthropogenic CO_2 to the surface and is able to uptake a higher amount of CO_2 (Frölicher et al., 2015). The stronger upwelling seems to be related to the higher variation in CO_2 uptake around the similar latitudes within the ensemble, and among the CMIP6 models. The anthropogenic CO_2 is then transported to mid-latitude around 25 -40°S. Similar pattern occurs in the Northern Hemisphere. The considerable difference between *Hist* and *ESM-Hist* simulations around 45 – 65°S is

Table 4. Cumulative air-sea CO_2 fluxes (Pg C) in FOCI-MOPS and observation-based estimates and CIMP6 model results. FOCI-MOPS results are from mean of *Hist* and *ESM-Hist* runs. Changes in piControl runs are subtracted from the historical runs.

	Hist	*ESM-Hist*	Observations and CMIP6 model results
Cumulative air-sea CO_2 flux (1850 – 1994)	88±3	97±2	111±21 (1800 – 1994, Gruber et al., 2019)
Cumulative air-sea CO_2 flux (1994 – 2007)*	25±1	25±1	29±5 (Gruber et al., 2019)
Cumulative air-sea CO_2 flux (1850 – 2014)	129±2	139±2	140±10** (CMIP6 model results, Terhaar et al., 2021)

* Including only half of the air-sea CO_2 flux in 1994 and in 2007, to be consistent with the data period (mid-1994 to mid-2007) provided in Gruber et al. (2019)

** Mean of some CMIP6 models, including ACCESS-ESM1-5, CanESM5-CanOE, CanESM5, CESM2, CESM2-WACCM, CNRM-ESM2-1, GFDL-CM4, GFDL-ESM4, IPSL-CM6A-LR, MPI-ESM1-2-HR, NorESM2-LM, UKESM1-0-LL, and MIROC-ES2L (Terhaar et al., 2021, unconstrained results)

because of the underestimated cumulative compatible emission in the *Hist*. Nevertheless, the cumulative air-sea CO_2 flux is about 10 Pg C higher in the *ESM-Hist* and is less than 0.03% of the total DIC inventory, it has an insignificant contribution to the interior DIC distribution between *ESM-Hist* and *Hist* (Fig. S17).

In *Hist* and *ESM-Hist*, surface air temperature anomalies remain indistinguishable from *piControl* and *ESM-piControl*, and only start to increase from the 1920s onwards. The temperature anomalies during 2005–2014 are 0.80±0.05, 1.04±0.12, and 0.93 °C in *Hist*, *ESM-Hist*, and observations, respectively (Fig. 20c).

The heat content integrated from 0 to 2000 m during 2005–2014 in *Hist* increased about 257±6 Zeta joules (ZJ) from 1955–1964 period, very close to the observations (260–267 ZJ). The increase in *ESM-Hist* is 317±3 ZJ, 60 ZJ higher than in the *Hist*, and reflects the higher surface temperature anomalies, which presumable are a consequence of the higher atmospheric CO_2 concentrations in experiment *ESM-Hist*.

In general, *Hist* and *ESM-Hist* have a similar temporal evolution and response to anthropogenic forcing, and both largely agree with observations in terms of air-sea CO_2 fluxes, temperature, and ocean heat content.

3.4.2 Environmental drivers of marine biogeochemical changes

In addition to the carbon cycle, of particular interest in this study is the impact of climate change on the marine biogeochemistry. Several drivers are considered important in this respect, including sea surface temperature (SST), seawater pH, oxygen (O_2) and nitrate (NO_3) levels, and primary production (PP) (Kwiatkowski et al., 2020). Here we show the temporal evolution of the anomalies of these variables relative to the 1870 – 1899 reference period, as described in Kwiatkowski et al. (2020). Overall, the anomalies in both *Hist* and *ESM-Hist* simulations agree with the range of the CMIP6 mean (Fig. 22). SST anomalies in *Hist* and *ESM-Hist* are comparable during the historical period until the year 2000. Between 2005 – 2014, the SST anomaly in *ESM-Hist* amounts to 0.70±0.13 °C, slightly higher than 0.54±0.05 °C in *Hist* (Fig. 22a). In 2014, the 0.23 °C higher SST in the *ESM-Hist* compared to the *Hist* is in line with the higher surface air temperature (Fig. 20c). Between 2005 – 2014, the sea-surface pH values in *Hist* and *ESM-Hist* are 0.095±0.000 and 0.099±0.002 units lower than 1870 – 1899 (Fig. 22b),

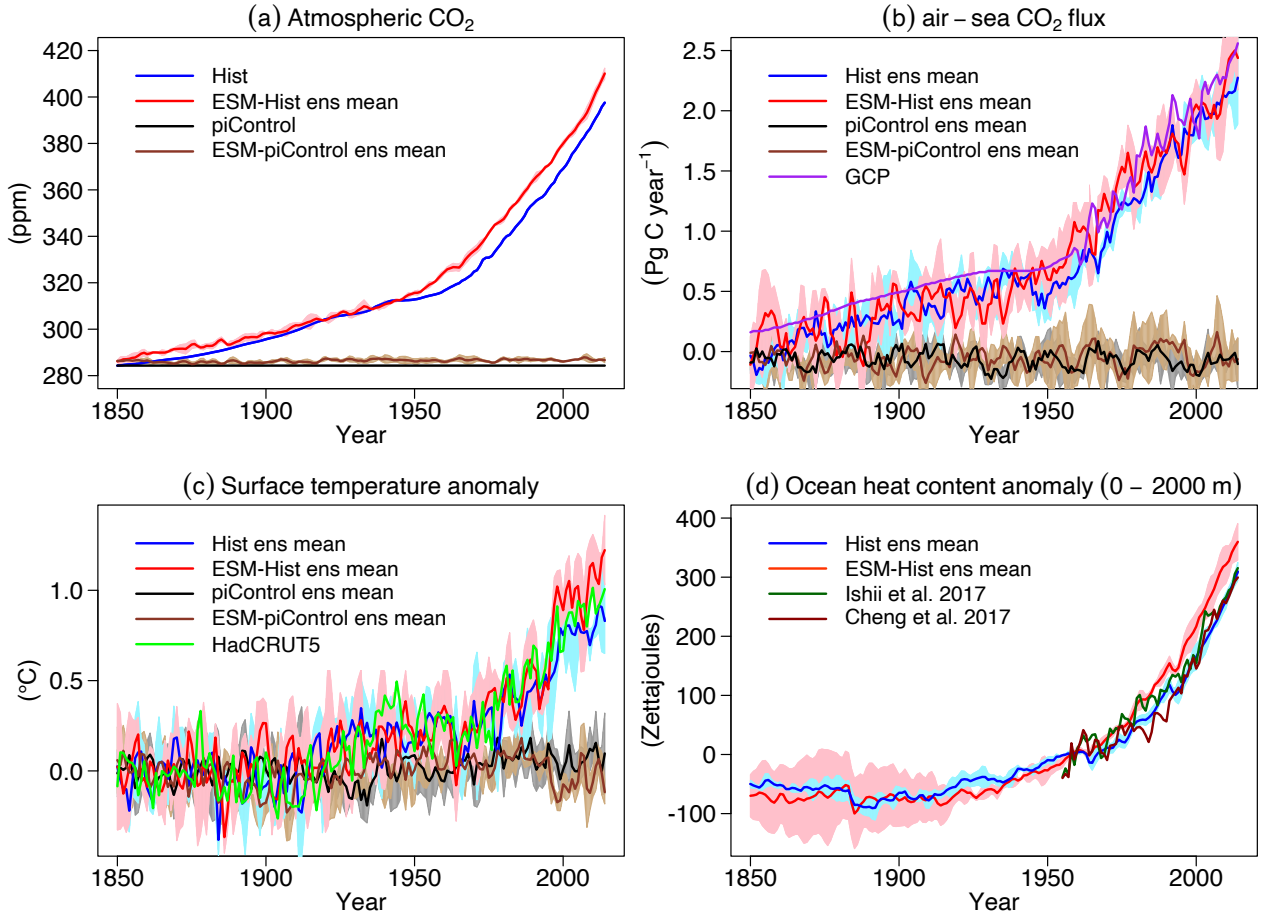

Figure 20. Time series of global atmospheric CO_2, globally-integrated air-sea CO_2 fluxes (positive downwards), globally-averaged surface temperature, and heat content at 0 - 2000 m in the ocean of of *Hist* and *ESM-Hist*. The piControl runs are subtracted to account for drifts. For surface temperature anomalies, the mean values over 1850 – 1879 are subtracted from the historical period, and for ocean heat content anomalies, the mean values over 1955 – 1964 are subtracted. (a) atmospheric CO_2 and (b) air-sea CO_2 fluxes, (c) surface temperature anomaly, and (d) ocean heat anomaly (0 – 2000 m). Gray/blue and brown/red lines stand for mean values of concentration-driven and emission-driven pre-industrial control/historical simulations, respectively. The purple line is air-sea CO_2 flux data from the Global Carbon Project (Friedlingstein et al., 2020, see summary tab in the data sheet). The light green line is surface temperature data from HadCRUT5 (Morice et al., 2021). Dark green and chocolate lines are ocean heat content data from Ishii et al. (2017) and Cheng et al. (2017).

415 respectively. The pH is slightly lower in *ESM-Hist* than in the *Hist* simulations due to a higher air-sea CO_2 flux (Fig. 20b). The O_2 anomalies averaged between 100 – 600 m are -2.92±0.58 mmol O_2 m^{-3} in *Hist* and -3.03±1.05 mmol O_2 m^{-3} in *ESM-Hist* simulations between 2005 – 2014 (Fig. 22c), that is, equivalent to a decrease of 2% in both simulations in this depth range. When it comes to the changes in the global O_2 inventory, FOCI-MOPS simulated a decrease of 284±32 Tmol O_2 per decade over 1960 to 2010. While the rate is substantially lower than what observations suggest (961±429 Tmol O_2 per

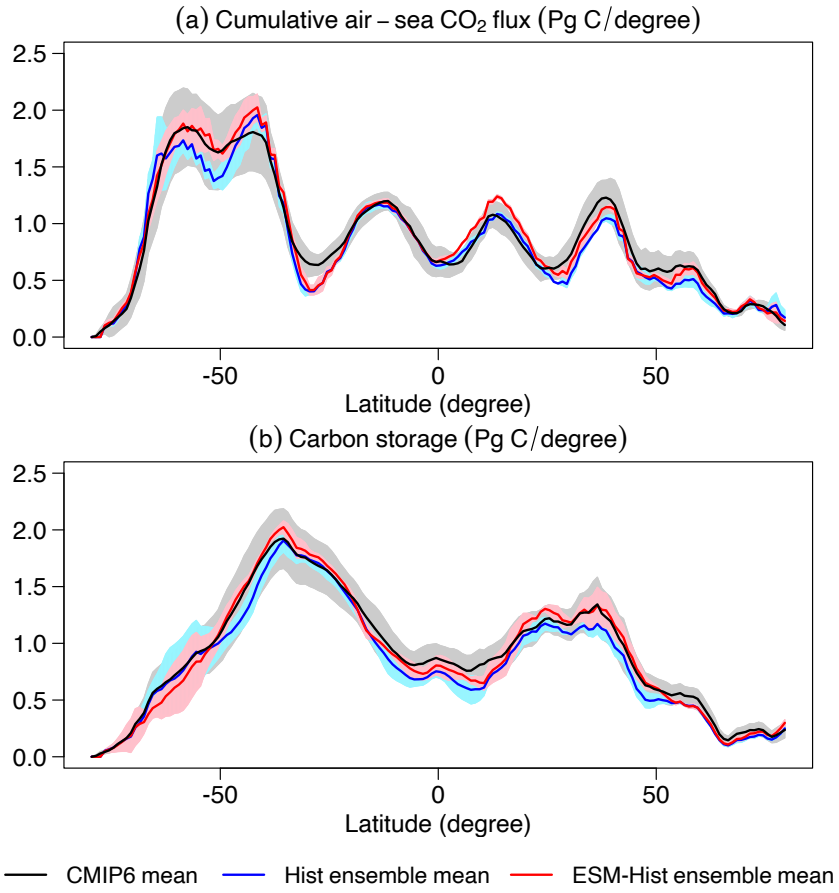

Figure 21. Cumulative air-sea CO_2 flux (positive downwards) and carbon storage between 1850 and 2014 simulated by FOCI-MOPS and CMIP6 models. The cumulative changes in air-sea CO_2 flux over 1850 to 2014 and changes in the carbon storage between 1850 and 2014 in piControl runs are subtracted from the historical runs. Zonally integrated (a) cumulative air-sea CO_2 flux and (b) carbon storage. Blue/red lines stand for mean values of *Hist* and *ESM-Hist* simulation ensembles of FOCI-MOPS, and black lines and shaded areas represent the mean and $\pm$ standard deviation of some CMIP6 models, including ACCESS-ESM1-5, CanESM5-CanOE, CanESM5, CESM2, CESM2-WACCM, CNRM-ESM2-1, GFDL-CM4, GFDL-ESM4, IPSL-CM6A-LR, MPI-ESM1-2-HR, NorESM2-LM, UKESM1-0-LL, and MIROC-ES2L. Results from MPI-ESM1-2-LR and MRI-ESM2-0 are also included for the carbon storage (Frölicher et al., 2015; Terhaar et al., 2021).

decade; Schmidtko et al., 2017), such an underestimation of observationally estimated changes in the marine O_2 inventory is a common feature among Earth system models (Oschlies et al., 2018). The NO_3 concentrations in the euphotic zone (0 – 100 m) are negatively correlated with SST (Fig. 22d), suggesting a reduced surface supply of NO_3 with increasing ocean stratification, a relationship that also exists in other global models (Fu et al., 2016). Similar to the temporal evolution of SST, the NO_3 remains relatively unchanged until the 2000s and the anomalies between 2005 – 2014 are -0.08$\pm$0.07 and -0.25$\pm$0.11 mmol N m^{-3} in *Hist* and *ESM-Hist* simulations, respectively (Fig. 22d). Temporal evolutions of PP in *Hist* and *ESM-Hist* are similar, the

averaged anomalies over 2005 – 2014 are -1.3±0.4% and -1.8±0.8% in the *Hist* and *ESM-Hist* simulations, respectively. These are at the upper end of the PP decrease projected with CMIP6 models (Fig. 22e).

4 Conclusions

In this study we present the implementation and evaluation of the marine biogeochemistry component coupled to FOCI. The resulting FOCI-MOPS model is based on MOPS ("Model of Oceanic Pelagic Stoichiometry"; Kriest and Oschlies, 2015), which simulates the elemental cycles of oceanic phosphorus, nitrogen, and oxygen, between their dissolved (PO_4, NO_3, O_2, and DOM) and particulate (phytoplankton, zooplankton, and detritus) pools . DIC and ALK are included in the implementation, providing a fully coupled carbon cycle in FOCI-MOPS. Spin-up (*spinup*) and an ensemble of three pre-industrial control (*piControl*) and historical (*Hist*) experiments, were performed with prescribed atmospheric CO_2 concentrations, following the CMIP6 protocols (Eyring et al., 2016). All tracers and fluxes approached steady-state or only showed small drifts relative to their mean concentrations in the end of the 500-year spin-up. The marine carbon inventory decreased 0.086 Pg C per year during the last 100 years in the spin-up, which is smaller than the drift suggested as "acceptable" (<0.1 Pg C yr^{-1}) in the Coupled Climate–Carbon Cycle Model Intercomparison Project (C4MIP) (Jones et al., 2016). Based on the applied metrics in Table 2 we conclude that FOCI-MOPS well reproduces observed biogeochemical patterns of inorganic tracers and phytoplankton/chlorophyll, and that the model large-scale performance is comparable with other CMIP models. Overall, globally integrated biogeochemical fluxes are in line with observational estimates (Table 3). The spatial patterns of surface-ocean pCO_2 and air-sea CO_2 fluxes agree well with observations (Fig. 18). Simulated changes due to the increasing atmospheric CO_2 in globally integrated air-sea CO_2 flux and ocean heat content (0–2000 m), as well as globally averaged surface air temperature also agree well with observations.

We also performed CO_2 emission-driven experiments, including *"ESM-spinup"*, *ESM-piControl* and *ESM-Hist*. The air-sea CO_2 flux in these simulations is slightly higher in the historical emission driven simulation (*ESM-Hist*) than in the atmospheric CO_2 driven simulation (*Hist*), resulting in a higher cumulative air-sea CO_2 flux of 139 Pg C relative to 129 Pg C in the *Hist* between 1850 and 2014. The difference in CO_2 perturbation forcing contributes to a higher atmospheric CO_2 until the end of the simulation period in *ESM-Hist* than in the *Hist* simulations. This higher atmospheric CO_2 likely contributes to the higher cumulative air-sea CO_2 flux, as well as the higher surface temperatures and ocean heat content in experiment *ESM-Hist*. Concerning the environmental drivers of marine biogeochemical changes (sea surface temperature, seawater pH, oxygen and nitrate levels, and primary production), their anomalies in both *Hist* and *ESM-Hist* simulations agree with the range of the CMIP6 model results (Fig. 22).

We plan to investigate possible shortcomings of the simulated ventilation by direct comparison of simulated and observed abiotic transient tracers (CFCs and SF6). This will better constrain shortcomings in the biogeochemical model component's parameterisations of export and remineralisation. We will implement an iron model (Somes et al., 2021) in the FOCI-MOPS to improve the potential model deficiency caused by lacking iron limitation in phytoplankton growth. Sensitivity runs with altered remineralisation schemes are currently under way. In addition, evaluations of surface seasonal cycle of the model will also be

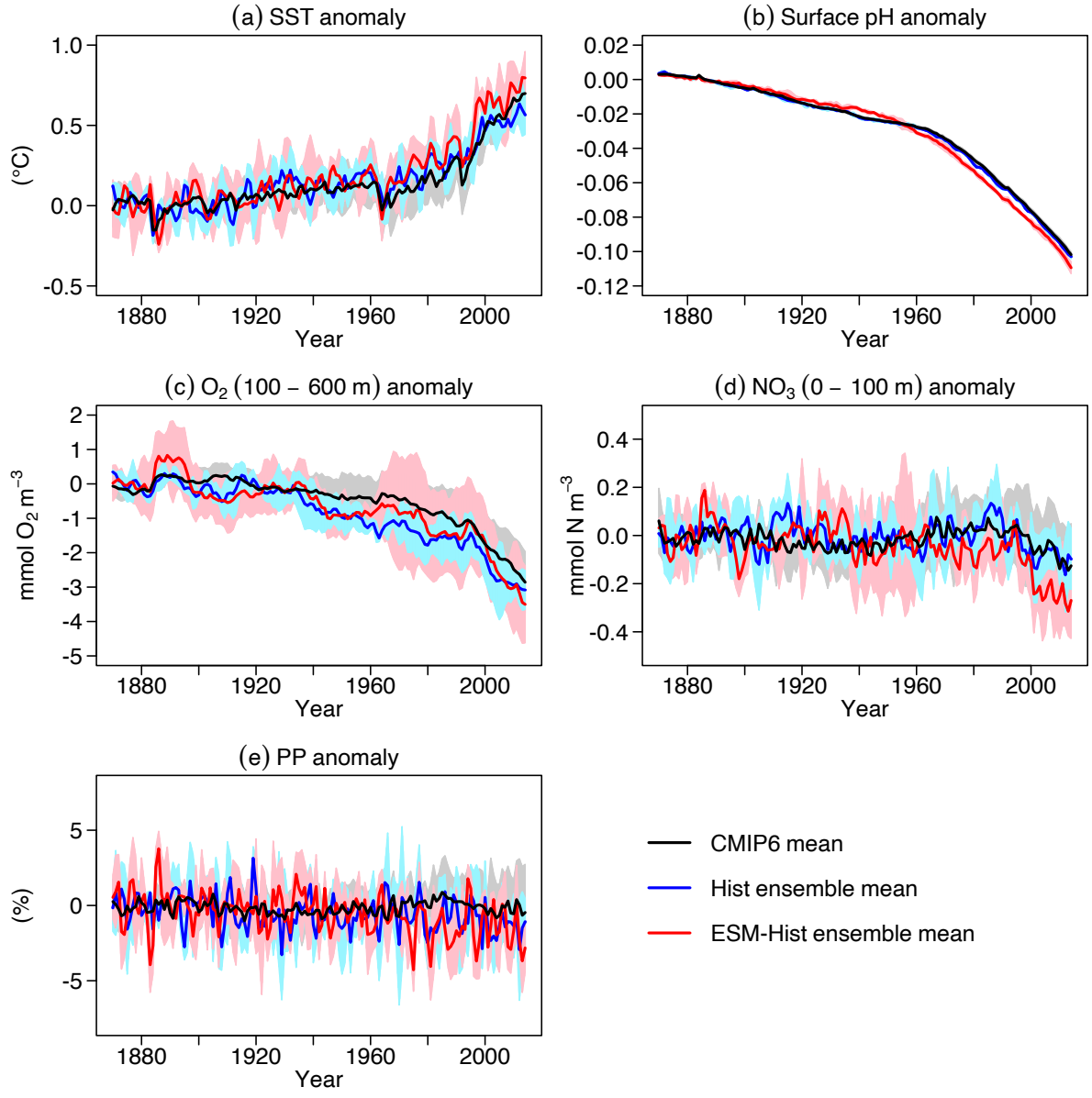

Figure 22. Temporal evolution of global mean a) sea surface temperature (SST), b) sea surface pH, c) oxygen (O_2) between 100 and 600 m, d) nitrate (NO_3) in the upper 100 m, and e) vertically integrated primary production (PP) in percentage. Values are relative to the mean of the time period 1870 – 1899 after subtracting the drifts of the piControl runs. Blue/red lines stand for mean values of *Hist* and *ESM-Hist* simulation ensembles of FOCI-MOPS, and black lines and shaded areas represent mean and ± standard deviation of CMIP6 models as described in Kwiatkowski et al. (2020).

carried out. We plan to use the model to investigate ocean-based CO_2 removal approaches for climate change mitigation, such as ocean alkalinity enhancement. While this can be done to some extent with the current model, new parameterisations and improvements in the simulation of ocean carbonate chemistry will likely be required. Although, some of this work can only be done when more experimental data is available to constrain the model.

We note that FOCI-MOPS is less complex than most of the biogeochemistry components employed in other Earth system models (Séférian et al., 2020), for instance it does not explicitly resolve silicate or iron cycles, and does not consider the $CaCO_3$ saturation state in the dissolution scheme. Nevertheless, as shown by our evaluation in this study, FOCI-MOPS overall shows an adequate performance that makes it an appropriate tool for studying marine biogeochemistry and biogeochemical-climate interactions in different climate change scenarios, in order to inform the development of emission pathways that are consistent with the agreed climate targets.

Code and data availability. The FOCI-MOPS is build based on a published FOCI version (Matthes et al., 2020). All modifications to the published version code and full runtime environment are provided at (https://doi.org/10.5281/zenodo.6772175). Model data and codes necessary to reproduce the figures present here are available at the same location.

Appendix A: Biogeochemical model equations and parameters

The biogeochemical model describes the cycling of phosphorus, nitrogen and oxygen in a stoichiometrically consistent manner ("Model of Oceanic Pelagic Stoichiometry"; Kriest and Oschlies, 2015). The model contains seven components, of which five are calculated in phosphorus units, namely phytoplankton (PHY), zooplankton (ZOO), detritus, dissolved organic matter (DOM) and phosphate (PO_4). Additionally, nitrate (NO_3) and oxygen (O_2) are simulated, with biogeochemical interactions among the different elements coupled via fixed stoichiometric ratios. As the model also simulates NO_3 loss and gain through denitrification and nitrogen fixation, respectively, the nitrate-to-phosphate ratio can vary. Details of the model can be found in Kriest and Oschlies (2015), and in section A1 we briefly describe the equations. We have coupled a carbon cycle, which involves the effects of biogeochemical interactions, calcite formation and dissolution on two additional components dissolved inorganic carbon (DIC) and alkalinity (ALK), and air-sea gas exchange of CO_2 across the sea surface. The implementation of the carbon cycle is described in section A2. Benthic-pelagic exchanges are described in section A3, and a summary of all equations is given in section A4. The biogeochemical model parameters and details on their calibration can be found in section A5.

A1 The biogeochemical model MOPS

A1.1 Plankton dynamics

Phytoplankton (PHY) growth depends on temperature T ($f_1(\mathrm{T})$), day light intensity (I, [W m^{-2} d^{-1}]) and day length τ [days] ($f_2(\mathrm{I},\tau)$), and nutrients ($f_3(\mathrm{PO_4},\mathrm{NO_3})$). Temperature-dependent growth is formulated following Eppley (1972), in the notation by Schmittner et al. (2008):

$$f_1(\mathrm{T}) = \mu'_{\mathrm{PHY}}\, e^{\frac{\mathrm{T}}{15.65}} \tag{A1}$$

where $\mu'_{\mathrm{PHY}} = 0.6$ [d^{-1}] is the maximum growth rate of phytoplankton at T$= 0$°C. Light limitation $f(\mathrm{I})$ is parameterised following Smith (1936), integrated over vertical box thickness and day according to Evans and Parslow (1985), in the notation by Evans and Garçon (1997). We note that while formulation by Evans and Garçon (1997) is based on maximum growth rate and the initial slope of the P-I-curve, α [(W m^{-2})$^{-1}$ d^{-1}], we here calculate the light limitation based on the half-saturation constant for light, $I_{\mathrm{c}} = 9.653$ [W m^{-2}], as expressed through $I_{\mathrm{c}} = \mu'_{\mathrm{PHY}}/\alpha$ (thereby resulting in $\alpha = 0.0622$ [(W m^{-2})$^{-1}$d^{-1}]).

$$f_2(\mathrm{I}) = \frac{\tau}{\Delta z(k_w + k_c \mathrm{PHY})} \left(\phi\left(\frac{2\mathrm{I}}{I_{\mathrm{c}}\tau}\right) - \phi\left(\frac{2\mathrm{I}}{I_{\mathrm{c}}\tau} e^{-\Delta z(k_w + k_c \mathrm{PHY})}\right)\right) \tag{A2}$$

where I [W m^{-2} d^{-1}] is total light during a day at the top of each vertical layer, τ is the length of a day in (fraction of) days, Δz is the vertical box thickness [m], and $k_w = 0.04$ [m^{-1}] and $k_c = 0.48$ [(mmol P m^{-3})$^{-1}$ m^{-1}] are the attenuation coefficients of water and phytoplankton, respectively. The function ϕ is given by

$$\phi(u) = \ln\left(u + \sqrt{1+u^2}\right) - \frac{\sqrt{1+u^2}-1}{u} \tag{A3}$$

(Evans and Garçon, 1997). The dependence of growth on nutrients $f_3(\mathrm{PO4}, \mathrm{NO_3})$ is based on a Monod-function of the least available nutrient X, assuming a constant stoichiometry of phytoplankton given by $d = 16$ [mol N:mol P]:

$$f_3(\mathrm{PO_4}, \mathrm{NO_3}) = \frac{X}{k_{\mathrm{PHY}} + X} \qquad \text{with} \quad X = \min\left(\mathrm{PO_4}, \frac{\mathrm{NO_3}}{d}\right) \tag{A4}$$

where $k_{\mathrm{PHY}} = 0.031$ [mmol P m^{-3}] is the half-saturation constant for phosphate (Kriest et al., 2017). Total phytoplankton growth PP [mmol P m^{-3} d^{-1}] is then given by the minimum of light and nutrient limitation , but only if the most limiting nutrient is above a certain threshold ($X > P^* = 10^{-6}$ [mmol P m^{-3}]):

$$PP = f_1(\mathrm{T})\,\mathrm{PHY}\,\min(f_2(\mathrm{I}), f_3(\mathrm{PO4}, \mathrm{NO_3})) \tag{A5}$$

Phytoplankton experiences a linear loss given by $\lambda_{\mathrm{PHY}} = 0.03$ [d^{-1}]. It is grazed by zooplankton (ZOO), where grazing G described by a Holling-III function, with a maximum grazing rate $\mu_{\mathrm{ZOO}} = 1.893$ [d^{-1}] and half-saturation constant $K_{\mathrm{ZOO}} = 0.086$ [mmol P m^{-3}]:

$$G = \mu_{\mathrm{ZOO}}\mathrm{ZOO}\frac{\mathrm{PHY}^2}{K_{\mathrm{ZOO}}^2 + \mathrm{PHY}^2} \tag{A6}$$

Only a fraction $\epsilon_{\mathrm{ZOO}} = 0.75$ of grazing G (in [mmol P m^{-3} d^{-1}]) is effectively ingested, the rest is released again via egestion. Zooplankton further experiences a quadratic mortality $\kappa_{\mathrm{ZOO}} = 4.548$ [(mmol P m^{-3})$^{-1}$ d^{-1}], and a linear excretion rate given by $\lambda_{\mathrm{ZOO}} = 0.03$ [d^{-1}]. Phytoplankton and zooplankton further die with a constant mortality rate of $\lambda'_{\mathrm{PHY}} = \lambda'_{\mathrm{ZOO}} = 0.01$ [d^{-1}], but only when present above the lower concentration threshold $P^* = 10^{-6}$ [mmol P m^{-3}]. Therefore, the source-minus-sink terms due to biogeochemical interactions for phytoplankton ($S^{\mathrm{Bio}}_{\mathrm{PHY}}$) and zooplankton ($S^{\mathrm{Bio}}_{\mathrm{ZOO}}$) are

$$S^{\mathrm{Bio}}_{\mathrm{PHY}} = PP - G - \lambda_{\mathrm{PHY}}\mathrm{PHY} - \lambda'_{\mathrm{PHY}}\max(0, \mathrm{PHY} - P^*) \tag{A7}$$

$$S^{\mathrm{Bio}}_{\mathrm{ZOO}} = \epsilon_{\mathrm{ZOO}}G - \lambda_{\mathrm{ZOO}}\mathrm{ZOO} - \kappa_{\mathrm{ZOO}}\mathrm{ZOO}^2 - \lambda'_{\mathrm{ZOO}}\max(0, \mathrm{ZOO} - P^*) \tag{A8}$$

Note that whereas Kriest and Oschlies (2015) assumed that plankton cycling only occurs in the upper, well-lit waters, we here skip this restriction and compute plankton interactions over the full water column. (Of course, production will cease in the aphotic zone, because of the light limitation.) Further, we avoid possible negative concentrations because of the Eulerian timestepping by computing biogeochemical fluxes only when plankton concentrations are positive.

A1.2 DOP and Detritus

Dissolved organic matter is implicitly represented by the DOP in phosphorus units in a C:N:P molar ratio of 117:16:1 in the model. We assume that a fraction $\sigma_{\mathrm{DOP}} = 0.15$ of egestion, quadratic zooplankton mortality, and phytoplankton loss given by λ_{PHY} is released as DOP, the rest becomes detritus. Further, phytoplankton and zooplankton mortality leads immediately to the production of DOP. The DOP is remineralised in all layers with a constant rate $\lambda'_{\mathrm{DOP}} = 0.17$ [y^{-1}], but only when present above the lower limit of $P^* = 10^{-6}$ [mmol P m^{-3}]. Its oxic and suboxic remineralisation further depends on the availability of oxidants oxygen and nitrate, as described by terms $S^{\mathrm{Rox}}_{\mathrm{DOP}}$ and $S^{\mathrm{Rsubox}}_{\mathrm{DOP}}$, which are described in detail in section A1.3 below. Thus, the source-minus-sink term for DOP, $S^{\mathrm{Bio}}_{\mathrm{DOP}}$, is

$$\begin{aligned} S^{\mathrm{Bio}}_{\mathrm{DOP}} &= \sigma_{\mathrm{DOP}} \left[(1-\epsilon_{\mathrm{ZOO}})\, G + \kappa_{\mathrm{ZOO}} \mathrm{ZOO}^2 + \lambda_{\mathrm{PHY}} \mathrm{PHY} \right] \\ &+ \lambda'_{\mathrm{PHY}} \max(0, \mathrm{PHY} - P^*) + \lambda'_{\mathrm{ZOO}} \max(0, \mathrm{ZOO} - P^*) - S^{\mathrm{Rox}}_{\mathrm{DOP}} - S^{\mathrm{Rsubox}}_{\mathrm{DOP}} \end{aligned} \tag{A9}$$

Like DOP, detritus (DET) is remineralised with a fixed rate $\lambda'_{\mathrm{DET}} = 0.05$ [d^{-1}] to nutrients when present above the lower limit of $P^* = 10^{-6}$ [mmol P m^{-3}], and its decomposition depends on oxygen and nitrate, as described for terms $S^{\mathrm{Rox}}_{\mathrm{DET}}$ and $S^{\mathrm{Rsubox}}_{\mathrm{DET}}$ in section A1.3 below. In addition, detritus sinks through the water column. We assume that the sinking speed of detritus increases linearly with depth, according to $w = w(z) = w_{\mathrm{lin}}\, z$, where z is the centre of a layer. In steady state, and in the absence of any other processes, this parameterisation can be regarded as equivalent to the so-called "Martin" (power law) curve of particle flux, with the exponent b given by $b = \lambda'_{\mathrm{DET}} / w_{\mathrm{lin}}$ (see Kriest and Oschlies, 2008, for a detailed discussion). For easier comparison with other model studies, which explicitly define b, and for comparison with empirically observed values for this parameter, in our model experiments we prescribe $b = 1.41309$ and evaluate w_{lin} from it via $w_{\mathrm{lin}} = \lambda'_{\mathrm{DET}} / b$. Note that in MOPS, due to reduction of remineralisation by lack of oxidants (section A1.3), the local effective "Martin" exponent b may be smaller than initially prescribed. The source-minus-sink term of detritus, $S^{\mathrm{Bio}}_{\mathrm{DET}}$ is therefore

$$S^{\mathrm{Bio}}_{\mathrm{DET}} = (1-\sigma_{\mathrm{DOP}}) \left[(1-\epsilon_{\mathrm{ZOO}}) G + \kappa_{\mathrm{ZOO}} \mathrm{ZOO}^2 + \lambda_{\mathrm{PHY}} \mathrm{PHY} \right] - S^{\mathrm{Rox}}_{\mathrm{DET}} - S^{\mathrm{Rsubox}}_{\mathrm{DET}} + \frac{\partial w \mathrm{DET}}{\partial z}, \tag{A10}$$

A1.3 Oxic and suboxic remineralisation

If oxygen is above a threshold defined by ${O_2}^* = \max(0, O_2 - {O_2}^{\min})$, with ${O_2}^{\min} = 1$ [mmol O_2 m-3], organic matter is remineralised aerobically according to a sigmoidal function:

$$l_{O_2} = \frac{({O_2}^*)^2}{({O_2}^*)^2 + K_{O_2}^2} \tag{A11}$$

where $K_{O_2} = 1.066$ [mmol O_2 m-3] is the half-saturation constant for the heterotroph's uptake of oxygen. To prevent total oxygen consumption per time step from exceeding available oxygen, we first calculate the theoretical oxygen demand for aerobic remineralisation of detritus and DOP u_{O_2}:

$$u_{O_2} = l_{O_2} \left[\lambda'_{\mathrm{DET}} \max(0, \mathrm{DET} - P^*) + \lambda'_{\mathrm{DOP}} \max(0, \mathrm{DOP} - P^*)\right] R_{-O_2:P}\, \Delta t \tag{A12}$$

where λ'_{DOP} and λ'_{DET} are the remineralisation rates of DOP and detritus, respectively, and Δt is the time step length of the biogeochemical model. $R_{-O_2:P} = 165.08044$ denotes the stoichiometric oxygen demand of aerobic remineralisation. The aerobic decay rate limitation is then

$$s_{O_2} = l_{O_2} \frac{\min(O_2^*, u_{O_2})}{u_{O_2}} \tag{A13}$$

Therefore, the sinks of oxygen due to remineralisation of DOP and detritus are defined by

$$S^{\mathrm{Rox}}_{\mathrm{DOP}} = -\lambda'_{\mathrm{DOP}} \max(0, \mathrm{DOP} - P^*) s_{O_2} \tag{A14}$$

$$S^{\mathrm{Rox}}_{\mathrm{DET}} = -\lambda'_{\mathrm{DET}} \max(0, \mathrm{DET} - P^*) s_{O_2} \tag{A15}$$

If ${O_2}^*$ is lower than 36 mmol O_2 m^{-3} additionally denitrification sets in. As for oxygen, we first define a quadratic rate limitation of this process, based on a minimum concentration of nitrate, ${NO_3}^{\min} = 15.978$ [mmol N m^{-3}], with ${NO_3}^* = \max(0, NO_3 - {NO_3}^{\min})$. To account for inhibition of denitrification by oxygen we further reduce this rate by the inverse oxygen consumption rate:

$$l_{NO_3} = \frac{({NO_3}^*)^2}{({NO_3}^*)^2 + K_{NO_3}^2} (1 - l_{O_2}) \tag{A16}$$

where $K_{NO_3} = 23.104$ [mmol N m^{-3}] is the half-saturation constant for the denitrifiers' uptake of nitrate. As for oxygen, we restrict the use of nitrate to the amount available:

$$u_{NO_3} = l_{NO_3} \left[\lambda'_{\mathrm{DET}} \max(0, \mathrm{DET} - P^*) + \lambda'_{\mathrm{DOP}} \max(0, \mathrm{DOP} - P^*)\right] R_{-NO_3:P}\, \Delta t \tag{A17}$$

with $R_{-\mathrm{NO3:P}} = 0.8R_{-\mathrm{O_2:P}} - d = 116.064352$ [mmol NO_3:mmol P], following the stoichiometry of Paulmier et al. (2009). The rate limitation of anaerobic decay is then

$$s_{\mathrm{NO_3}} = l_{\mathrm{NO3}} \frac{\min(\mathrm{NO_3}^*, u_{\mathrm{NO3}})}{u_{\mathrm{NO_3}}} \tag{A18}$$

Therefore, the sinks of oxygen and nitrate due to denitrification of DOP and detritus are defined by

$$S^{\mathrm{Rsubox}}_{\mathrm{DOP}} = -\lambda'_{\mathrm{DOP}} \max(0, \mathrm{DOP} - P^*) s_{\mathrm{NO_3}} \tag{A19}$$

$$S^{\mathrm{Rsubox}}_{\mathrm{DET}} = -\lambda'_{\mathrm{DET}} \max(0, \mathrm{DET} - P^*) s_{\mathrm{NO_3}} \tag{A20}$$

A1.4 Nitrogen fixation

As in Kriest and Oschlies (2015) nitrogen fixation depends on temperature and nutrient ratio:

$$S^{\mathrm{NFix}}_{\mathrm{NO_3}} = \mu_{\mathrm{NFix}} \max\left(0, \frac{t_2 \mathrm{T}^2 + t_1 \mathrm{T} - t_0}{t_f}\right) \max\left(0, 1 - \frac{\mathrm{NO_3}}{d\mathrm{PO_4}}\right) \tag{A21}$$

with $\mu_{\mathrm{NFix}} = 1.88924$ [μmol N m^{-3} d^{-1}] being the maximum nitrogen fixation of the (implicit) cyanobacteria, and t_2, t_1, t_0 and t_f coefficients that describe the temperature dependency of nitrogen fixation of *Trichodesmium spp.* (Breitbarth et al., 2007), using the approximation by Kriest and Oschlies (2015). We note that in the model nitrogen fixation only occurs when $\mathrm{PO_4} > 10^{-6}$ mmol P m^{-3}.

A1.5 Nutrients and oxygen

Phosphate (PO_4) is affected by primary production, excretion by zooplankton, and the decay of dissolved and particulate organic matter, as explained above, leading to a source-minus-sink term due to biogeochemical interactions, $S^{\mathrm{Bio}}_{\mathrm{PO_4}}$, of

$$S^{\mathrm{Bio}}_{\mathrm{PO_4}} = (-PP + \lambda_{\mathrm{ZOO}}\mathrm{ZOO}) + S^{\mathrm{Rox}}_{\mathrm{DOP}} + S^{\mathrm{Rsubox}}_{\mathrm{DOP}} + S^{\mathrm{Rox}}_{\mathrm{DET}} + S^{\mathrm{Rsubox}}_{\mathrm{DET}} \tag{A22}$$

The loss and gain of nitrate (NO_3) follows that of phosphate for aerobic processes and production. In addition, this tracer is affected by denitrification (fixed nitrogen loss) and nitrogen fixation (fixed nitrogen gain):

$$S^{\mathrm{Bio}}_{\mathrm{NO_3}} = S^{\mathrm{NFix}} - dPP + d\left(\lambda_{\mathrm{ZOO}}\mathrm{ZOO} + S^{\mathrm{Rox}}_{\mathrm{DOP}} + S^{\mathrm{Rox}}_{\mathrm{DET}}\right) - R_{-\mathrm{NO_3:P}}\left(S^{\mathrm{Rsubox}}_{\mathrm{DOP}} + S^{\mathrm{Rsubox}}_{\mathrm{DET}}\right) \tag{A23}$$

Finally, oxygen (O_2) increases due to photosynthesis, and decreases because of aerobic remineralisation and respiration by zooplankton.

$$S^{\mathrm{Bio}}_{\mathrm{O_2}} = R_{-\mathrm{O_2:P}} \left(PP - \lambda_{\mathrm{ZOO}} \mathrm{ZOO} - S^{\mathrm{Rox}}_{\mathrm{DOP}} - S^{\mathrm{Rox}}_{\mathrm{DET}} \right) \quad \text{(A24)}$$

In addition, oxygen exchanges with the atmosphere at the sea surface (i.e., for layer 1) $S^{\mathrm{Air}}_{\mathrm{O_2}}$, following Orr et al. (2017).

A2 The carbon cycle

A2.1 Coupling to the biogeochemical core

Photosynthesis decreases DIC, whereas remineralisation of organic matter to phosphate increases it. We assume a constant stoichiometry between phosphorus and carbon, $a = 117$ [mol C:mol P]; DIC thus changes in proportion to changes in phosphate:

$$S^{\mathrm{Bio}}_{\mathrm{DIC}} = a\, S^{\mathrm{Bio}}_{\mathrm{PO_4}} \quad \text{(A25)}$$

Changes in phosphate and nitrate further affect alkalinity via

$$S^{\mathrm{Bio}}_{\mathrm{ALK}} = -S^{\mathrm{Bio}}_{\mathrm{PO_4}} - S^{\mathrm{Bio}}_{\mathrm{NO_3}} \quad \text{(A26)}$$

A2.2 Calcite production and dissolution

We assume that a constant fraction $p^{\mathrm{CaCO_3}}$ of detritus production via zooplankton egestion and plankton mortality to detritus is in the form of calcite.

$$p^{\mathrm{CaCO_3}} = a\, \sigma_{\mathrm{CaCO_3}} (1 - \sigma_{\mathrm{DOP}}) \left[(1 - \epsilon_{\mathrm{ZOO}}) G + \kappa_{\mathrm{ZOO}} \mathrm{ZOO}^2 + \lambda_{\mathrm{PHY}} \mathrm{PHY} \right] \quad \text{(A27)}$$

where $a = 117$ [mol C:mol P] is the molar ratio of C:P in organic matter, and $\sigma_{\mathrm{CaCO_3}} = 0.032$ [mol $CaCO_3$:mol C] the calcite-to-organic-carbon ratio. Calcite production reduces DIC by one, and alkalinity by two:

$$S^{\mathrm{CaCO_3P}}_{\mathrm{DIC}} = -p^{\mathrm{CaCO_3}} \quad \text{(A28)}$$

$$S^{\mathrm{CaCO_3P}}_{\mathrm{ALK}} = -2\, p^{\mathrm{CaCO_3}} \quad \text{(A29)}$$

Following Schmittner et al. (2008), we integrate the production of calcite over the entire water column:

$$P^{\mathrm{CaCO_3}} = \int_0^{\mathrm{Bottom}} p^{\mathrm{CaCO_3}} \mathrm{d}z \quad \text{(A30)}$$

The total production of calcite is then distributed and dissolved immediately over the entire water column with an e-folding profile $D = \exp(-z/l_{\mathrm{CaCO_3}})$, with $l_{\mathrm{CaCO_3}} = 4289.4$ m, thereby affecting alkalinity and DIC:

$$S_{\mathrm{DIC}}^{\mathrm{CaCO_3D}} = P^{\mathrm{CaCO_3}} \frac{\partial D}{\partial z} \tag{A31}$$

$$S_{\mathrm{ALK}}^{\mathrm{CaCO_3D}} = 2\, P^{\mathrm{CaCO_3}} \frac{\partial D}{\partial z} \tag{A32}$$

and thus the total source-minus-sink for DIC and alkalinity due to calcite formation and dissolution are

$$S_{\mathrm{DIC}}^{\mathrm{CaCO_3}} = S_{\mathrm{DIC}}^{\mathrm{CaCO_3P}} + S_{\mathrm{DIC}}^{\mathrm{CaCO_3D}} \tag{A33}$$

$$S_{\mathrm{ALK}}^{\mathrm{CaCO_3}} = S_{\mathrm{ALK}}^{\mathrm{CaCO_3P}} + S_{\mathrm{ALK}}^{\mathrm{CaCO_3D}} \tag{A34}$$

We note that the redistribution with an e-folding profile over all layers can result in some upward transport of the alkalinity gain caused by calcite dissolution, if calcite-bearing detritus produced at greater depths dissolves further up in the water column. It may, however, be just a small problem, as most detritus will likely be produced in shallow layers, where zooplankton grazing and mortality is high.

A2.3 Air-sea gas exchange of CO_2 and solution of the carbonate system

The simulation of the carbonate chemistry system and of the air-sea gas exchange of CO_2 in MOPS follows an OCMIP-type formulation (Orr et al., 1999) with updates from Orr et al. (2017) for the air-sea gas exchange of CO_2.

The air–sea CO_2 flux is computed as:

$$F_{\mathrm{CO_2}} = k_w \left([CO_2^*]_{sat} - [CO_2^*]\right) \tag{A35}$$

where k_w (in m sec^{-1}) is the gas transfer velocity, $[CO_2^*]_{sat}$ (in mol kg^{-1}) is the saturation concentration of CO_2, and $[CO_2^*]$ (in mol kg^{-1}) is the surface-ocean dissolved CO_2 concentration (please see below for further detail). The instantaneous gas transfer velocity k_w is parameterized based on Wanninkhof (2014) as a quadratic function of the 10m wind speed u:

$$k_w = \xi \left(\frac{Sc}{660}\right)^{-0.5} u^2 \,(1 - f_{ice}) \tag{A36}$$

where ξ is a constant, Sc is the Schmidt number, and f_{ice} is the fraction of the grid cell covered by sea ice.

The saturation concentration of CO_2 in equilibrium with the water-vapor saturated atmosphere at a total atmospheric pressure of 1 atm (i.e. $[CO_2^*]_{sat}$) is computed as:

$$[CO_2^*]_{\mathrm{sat}} = F\, xCO_2 \tag{A37}$$

Where xCO_2 is the mole fraction of CO_2 in dry air and F is the solubility function (Weiss and Price (1980) eq. 13, Table 6, column 3) which includes all non-ideality effects and which fits the effects of water vapor pressure for a total atmospheric pressure of 1 atm.

Once dissolved, CO_2 reacts with seawater forming carbonic acid (H_2CO_3), most of which dissociates into two other inorganic species, bicarbonate (HCO_3^-) and carbonate (CO_3^{2-}) ions. CO_2^* refers to the sum of dissolved CO_2 and the much less abundant H_2CO_3. The sum of the three species CO_2^* + HCO_3^- + CO_3^{2-} is referred to as total dissolved inorganic carbon (DIC). Their partitioning depends on seawater pH, temperature, salinity, and pressure. pH may be calculated from DIC and seawater's ionic charge balance, formalized as total alkalinity (ALK). DIC and ALK are carried as prognostic tracers in the ocean model, and both are used, along with temperature, salinity, and nutrient concentrations, to compute CO_2^* at the ocean surface.

The carbonate chemistry system is solved using the equilibrium constants recommended for best practices (Dickson et al., 2007). The total pH scale is used for all constants except Ks (which uses the "free" scale following Dickson (1990)). The model does not explicitly simulate boron, sulfate and fluoride which are instead estimated as function of chlorinity based on Lee et al. (2010) (for boron), Morris and Riley (1966) (for sulfate) and Riley (1965) (for fluoride). Silicate, which is also not explicitly simulated, is computed as a function of density following Orr et al. (1999).

For reasons of computational efficiency, to solve the carbonate chemistry system we use the approximate and non-iterative method proposed by Follows et al. (2006) (eqs. 8, 11, 12 therein). The algorithm has been shown to provide a sufficiently accurate solution in the context of a three-dimensional global ocean carbon cycle model. The algorithm uses as inputs DIC, ALK, dissolved inorganic phosphorus, silica and boron, as well as the thermodynamic equilibrium coefficients. The species retained in the expression for alkalinity are the phosphoric, silicic, carbonic, boric, sulphuric, fluoridic, and water acid systems. Starting from an initial guess of pH deriving from the previous time step, the formula provides as output an updated value of pH which is then used to compute CO_2^* (eq. 8 in Follows et al., 2006) and surface CO_2 fugacity as:

$$fCO_2 = \frac{CO_2^*}{K_0} \tag{A38}$$

Where K_0 is the solubility coefficient of CO_2 in seawater (eq. 12 and Table 1, column 3 in Weiss (1974)).

A3 Benthic burial and nutrient re-supply

As in Kriest and Oschlies (2013) and Kriest and Oschlies (2015) we assume that once sinking detritus arrives at the seafloor a fraction of it is buried in the sediments. The amount buried, $S_{\mathrm{DET}}^{\mathrm{BUR}}$ [mmol P m^{-2} d^{-1}], depends on the rain rate of detritus to the sea floor (F_{B}, [mmol P m^{-2} d^{-1}]) via

$$S_{\mathrm{DET}}^{\mathrm{BUR}} = \begin{cases} 1.6828\, F_{\mathrm{B}}^{1.799} & k = k_b \\ 0 & k < k_b \end{cases} \tag{A39}$$

where k is the index of each vertical box (counting downwards) and k_b is the last ocean box above the sea floor at each horizontal model grid point.

In contrast to Kriest and Oschlies (2013) and Kriest and Oschlies (2015), the amount buried is not integrated globally and over a year, and then resupplied to the ocean via river runoff; instead, in every time step the global amount of organic

phosphorus, nitrogen and buried is resupplied at the sea surface (in the surface layer) as phosphate, nitrate and DIC. Thus, if $B = \int_A F_{\mathrm{BUR}} \mathrm{d}a$ is the global burial in a time step, integrated over the sea floor area A, and V_1 the global volume of the surface layer

$$S_{\mathrm{PO_4}}^{\mathrm{Supply}} = \begin{cases} \frac{B}{V_1} & k = 1 \\ 0 & k > 1 \end{cases} \tag{A40}$$

We note that this approach has a slightly "fertilising" effect even away from the river mouths. To account for the implicit, simultaneous burial of particulate organic carbon and nitrogen, the respective supply of nitrate and DIC is parameterised using constant stoichiometry:

$$S_{\mathrm{NO_3}}^{\mathrm{Supply}} = d\, S_{\mathrm{PO_4}}^{\mathrm{Supply}} \tag{A41}$$

$$S_{\mathrm{DIC}}^{\mathrm{Supply}} = a\, S_{\mathrm{PO_4}}^{\mathrm{Supply}} \tag{A42}$$

We also account for the equivalent of negative alkalinity (that would be consumed when organic matter was remineralised instead of being buried) by subtracting it from alkalinity at the sea surface:

$$S_{\mathrm{ALK}}^{\mathrm{Supply}} = -S_{\mathrm{PO_4}}^{\mathrm{Supply}} - S_{\mathrm{NO_3}}^{\mathrm{Supply}} \tag{A43}$$

In contrast to organic material, we assume no burial of calcite in the sediment, but dissolve all calcite arriving in the bottom box immediately.

A4 Total source-minus-sinks

Summing up the effects of all processes we arrive at the following equations for the source-minus-sink terms:

$$S_{\mathrm{PHY}} = S_{\mathrm{PHY}}^{\mathrm{Bio}} \quad \text{(equation A7)} \tag{A44}$$

$$S_{\mathrm{ZOO}} = S_{\mathrm{ZOO}}^{\mathrm{Bio}} \quad \text{(equation A8)} \tag{A45}$$

$$S_{\mathrm{DOP}} = S_{\mathrm{DOP}}^{\mathrm{Bio}} \quad \text{(equation A9)} \tag{A46}$$

$$S_{\mathrm{DET}} = S_{\mathrm{DET}}^{\mathrm{Bio}} - S_{\mathrm{DET}}^{\mathrm{BUR}} \quad \text{(equations A10 and A39)} \tag{A47}$$

$$S_{\mathrm{PO_4}} = S_{\mathrm{PO4}}^{\mathrm{Bio}} + S_{\mathrm{PO_4}}^{\mathrm{Supply}} \quad \text{(equations A22 and A40)} \tag{A48}$$

$$S_{\mathrm{NO_3}} = S_{\mathrm{NO3}}^{\mathrm{Bio}} + S_{\mathrm{NO_3}}^{\mathrm{Supply}} \quad \text{(equations A23 and A41)} \tag{A49}$$

$$S_{\mathrm{O_2}} = S_{\mathrm{O_2}}^{\mathrm{Bio}} + S_{\mathrm{O_2}}^{\mathrm{Air}} \quad \text{(equation A24 and Orr et al. (2017))} \tag{A50}$$

$$S_{\mathrm{DIC}} = S_{\mathrm{DIC}}^{\mathrm{Bio}} + S_{\mathrm{DIC}}^{\mathrm{CaCO3}} + S_{\mathrm{DIC}}^{\mathrm{Supply}} + S_{\mathrm{DIC}}^{\mathrm{Air}} \quad \text{(equations A25, A33, A42 and Orr et al. (2017))} \tag{A51}$$

$$S_{\mathrm{ALK}} = S_{\mathrm{ALK}}^{\mathrm{Bio}} + S_{\mathrm{ALK}}^{\mathrm{CaCO3}} + S_{\mathrm{ALK}}^{\mathrm{Supply}} \quad \text{(equations A26, A34, A43)} \tag{A52}$$

A5 Parameter calibration

The biogeochemical model parameterisation is based upon a previous objective calibration of model MOPS coupled to the Transport Matrix Method (Khatiwala, 2007; Khatiwala et al., 2018), using Transport Matrices derived from the ECCO project (Kriest et al., 2020). In particular, Kriest et al. (2020) optimised the parameters for oxidant-dependent remineralisation $NO_3^{\min}$, K_{NO_3}, K_{O_2}, the maximum nitrogen fixation rate μ_{NFix}, the oxygen requirement for aerobic remineralisation, $R_{-O_2:P}$ and the parameter determining the particle flux profile b against observed nutrients and oxygen at a global scale, while all other parameters were kept constant.

However, when comparing parameters optimised for different circulations, Kriest et al. (2020) noted that three of the six parameters optimised were sensitive to characteristic features of the applied circulation, as expressed through the maximum mixed layer depth, age of NADW, and outcrop area of SAMW and AAIW. We therefore adjusted $R_{-O_2:P}$, b and μ_{NFix} to the values for the respective physical diagnostic of NEMO, by using the regression shown in Fig. 6 of Kriest et al. (2020). The adjustment led to a higher value for $R_{-O_2:P}$ (165.08044 instead of 151.1 mol O_2:mol P), a slightly lower value for b (1.41309 instead of 1.46), and a lower value of μ_{NFix} (1.88924 instead of 2.29 μmol N m^{-3} d^{-1}; see also table A1).

To adjust the parameters regarding the calcite cycle, we have extended MOPS in the setup ECCO described by Kriest et al. (2020) to include the carbon cycle described above, but with a slightly different air-sea gas exchange and computation of the carbonate system, and optimised σ_{CaCO3} and l_{CaCO3} after a spin up of 10 years against a data set of alkalinity and preindustrial DIC. The resulting parameters are only slightly different from those applied by Schmittner et al. (2008), namely $\sigma_{CaCO3} = 0.032$ mol $CaCO_3$:mol C_{org} (instead of 0.035 mol $CaCO_3$:mol C_{org}) and $l_{CaCO3} = 4289.4$ m (instead of 3500 m).

Table A1. Biogeochemical model parameters of MOPS (see also Kriest et al., 2020) and for the carbon cycle.

Parameter	Value	Unit	Meaning
Phytoplankton			
μ_{PHY}	0.6	d^{-1}	max. growth rate
I_{c}	9.653	$\mathrm{W\ m}^{-2}$	half-saturation constant for light
K_{PHY}	0.031	$\mathrm{mmol\ P\ m}^{-3}$	half-saturation constant for phosphate
λ_{PHY}	0.03	d^{-1}	exudation rate
λ'_{PHY}	0.01	d^{-1}	mortality rate
Zooplankton			
μ_{ZOO}	1.893	d^{-1}	max. grazing rate
K_{ZOO}	0.086	$\mathrm{mmol\ P\ m}^{-3}$	half-saturation constant
ϵ_{ZOO}	0.75		assimilation efficiency
κ_{ZOO}	4.548	$(\mathrm{mmol\ P\ m}^{-3})^{-1}\ \mathrm{d}^{-1}$	quadratic mortality rate
λ_{ZOO}	0.03	d^{-1}	excretion rate
λ'_{ZOO}	0.01	d^{-1}	mortality rate
Organic matter			
σ_{DOP}	0.15		fraction of organic matter released as DOP
λ'_{DOP}	0.17	y^{-1}	DOP decay rate
$\mathrm{NO}_3^{\mathrm{min}}$	15.978	$\mathrm{mmol\ N\ m}^{-3}$	nitrate threshold for denitrification
$\mathrm{O}_2^{\mathrm{min}}$	1.0	$\mathrm{mmol\ O_2\ m}^{-3}$	oxygen threshold for denitrification
$K_{\mathrm{NO_3}}$	23.104	$\mathrm{mmol\ N\ m}^{-3}$	half sat.-constant for denitrification
$K_{\mathrm{O_2}}$	1.066	$\mathrm{mmol\ N\ m}^{-3}$	half sat.-constant for oxic remineralisation
λ'_{DET}	0.05	d^{-1}	detritus decay rate
b	1.41309		sinking exponent
Nitrogen fixation			
μ_{NFix}	1.88924	$\mu\mathrm{mol\ N\ m}^{-3}\ \mathrm{d}^{-1}$	max. nitrogen fixation rate
t_2	-0.0042	$^{\circ}\mathrm{C}^{-2}$	coefficient for T-dependency
t_1	0.2253	$^{\circ}\mathrm{C}^{-1}$	coefficient for T-dependency
t_0	-2.7819		coefficient for T-dependency
t_f	0.2395		coefficient for T-dependency
Carbon cycle and stoichiometry			
d	16	mol N:mol P	nitrogen stoichiometry of organic matter
a	117	mol C:mol P	carbon stoichiometry of organic matter
$R_{-\mathrm{O_2:P}}$	165.08044	mol $\mathrm{O_2}$:mol P	$\mathrm{O_2}$ demand of remineralisation
$\sigma_{\mathrm{CaCO_3}}$	0.032	mol $\mathrm{CaCO_3}$:mol $\mathrm{C_{org}}$	fraction of calcite in organic carbon
$l_{\mathrm{CaCO_3}}$	4289.4		e-folding dissolution length scale of calcite

Appendix B: Biogeochemical model evaluation

B1 Model postprocessing

The model geometry is based on a curvilinear grid, complicating a direct comparison to observations, which are mostly available on regular (rectangular) grids. Thus, we have mapped the model output onto a horizontal grid defined by $1^\circ \times 1^\circ$, using Ferret's functions `curv_to_rect_map` (with a radius of 2° for map creation) and `curv_to_rect`. The vertical grid of NEMO was maintained. All further analysis of model fit was carried out on these remapped quantities, unless stated otherwise.

B2 Data sets for model validation

For a complete biogeochemical model evaluation we used data sets of phosphate, nitrate, oxygen, DIC, total alkalinity, surface chlorophyll, mesozooplankton, particulate and dissolved organic matter. Because many of the observed quantities are available in different spatial resolutions they were gridded onto the rectangular model grid. Further details, including conversion from different units, are described below.

B2.1 Nutrients, oxygen, DIC and alkalinity

For the spatial distribution (Section 3.2.1) comparisons of dissolved inorganic tracers we used the interpolated data, and for model evaluation with statistical metrics (Section 3.2.3) we used the non-interpolated data of the Global Ocean Data Analysis Project version 2 mapped climatology (GLODAPv2.2016b, Lauvset et al., 2016; Olsen et al., 2016), as available under `https://www.nodc.noaa.gov/ocads/oceans/GLODAPv2_2020/` (downloaded on 12 May 2016). Observed concentrations of all inorganic tracers have been converted from μmol kg^{-1} to mmol m^{-3} using in situ density computed from GLODAP's temperature and salinity. Originally the non-interpolated data set contains between 158401 and 252808 data points for the different tracers; because the NEMO grid, onto which the data are interpolated, has a higher vertical resolution, the final data set contains between 183213 and 295603 data points (see Table B1).

B2.2 Phytoplankton

For the assessment of simulated phytoplankton we use chlorophyll data derived from remote sensing (MODIS-Aqua; Melin, 2013, downloaded on 08 April 2020). The original surface data are available as a monthly climatology on a 9 km grid. After averaging to annual mean chlorophyll, the data are gridded (by averaging) onto a horizontal grid defined by $1^\circ \times 1^\circ$. Chlorophyll was converted to carbon using the algorithm derived by Sathyendranath et al. (2009), and then to phosphorus using a C:P ratio of 117 mol C: mol P. The resulting data set contains 36.669 data points, which are all located in the surface layer, with minimum and maximum values of 0 and 0.25 mmol P m^{-3}, respectively, an unweighted mean of 0.0161 mmol P m^{-3} and a standard deviation of 0.0122 mmol P m^{-3} (see Table B1).

Table B1. Statistics for observations, regridded onto model grid: number of observations, minimum and maximum concentration, volume-weighted mean and standard deviation. See section B2 for further details.

Type	Unit	Number	Min	Max	Mean	SD	Source
PO_4	mmol P m^{-3}	267495	0	3.63	2.14	0.71	Lauvset et al. (2016),
NO_3	mmol N m^{-3}	282467	0	47.56	30.41	9.76	Olsen et al. (2016)
O_2	mmol O_2 m^{-3}	295603	0.5	463.9	183.90	69.37	
DIC	mmol C m^{-3}	201421	1181	2495	2327	87.3	
Alkalinity	mmol Eq m^{-3}	185676	1152	2731	2444	57.7	
Phytoplankton, surface	mmol P m^{-3}	36669	0	0.248	0.0161	0.0122	Melin (2013)
Zooplankton, 0-100m	mmol P m^{-3}	37828	0	0.348	0.0062	0.0101	Moriarty and O'Brien (2013)
POP	mmol P m^{-3}	13061	0	1.685	0.0246	0.0417	Martiny et al. (2014)
DOP, 0-100m	mmol P m^{-3}	1765	0	3.92	0.167	0.185	Torres-Valdés et al. (2009), Moutin et al. (2008), Yoshimura et al. (2007), Landolfi (unpubl.)

B2.3 Zooplankton

For the evaluation of simulated zooplankton we use the MAREDAT data set of mesozooplankton (Moriarty and O'Brien, 2013). This sparse, quasi-climatological data set contains 42.245 data points of monthly mean mesozooplankton (in mg C m^{-3}) on a $1° \times 1°$ degree grid. After averaging over a year, and mapping onto the spatial grid of NEMO, we obtained a total of 37.838 data points for the upper 100 m. Conversion to phosphorus was carried out by assuming a C:P ratio of 117 mol C: mol P.

Many groups of mesozooplankton carry out diurnal vertical migration, i.e. they descend to depths between $\approx 200 - 500$m depth at dawn, and ascend to the surface layers for feeding at dusk (e.g., Kiko et al., 2017, 2020). This process is so far not included in the model (see Aumont et al., 2017), and may lead to an overestimation of simulated zooplankton biomass, when compared only against surface data. Therefore, to account for the maximum total potential biomass of grazers in the observations, we integrated all observed biomass within the upper 500 m, and distributed it evenly over the upper 100 m for model comparison.

Further, the biogeochemical model does not distinguish between micro- and mesozooplankton, but aggregates both types into one single component. Unfortunately, samples for microzooplankton are much more sparse (only 2029 monthly data in the data set by Buitenhuis et al., 2012) than those of mesozooplankton, and often taken at other locations and during other times. Based on an analysis at stations where both small and large zooplankton observations are available, we estimated an approximate ratio of micro-to-mesozooplankton of one. For comparison with the model we therefore doubled the observed concentrations of mesozooplankton, resulting in minimum and maximum concentrations of 0 and 0.348 mmol P m^{-3}, an average of 0.0062 mmol P m^{-3}, and a standard deviation of 0.0101 mmol P m^{-3} (see Table B1).

B2.4 POP

There is no direct observational equivalent to simulated detritus; the closest type of observation are those of particulate organic phosphorus (POP), nitrogen (PON) or carbon (POC). For model evaluation we downloaded the data set by Martiny et al. (2014, data set CNP_data_DRYAD_edit_2.csv, downloaded on 16 April 2020), which contains observations of POP, PON and POC. After omitting some entries where depth was not given, we obtained 6940 data points for POP, and 46.705 data point for PON. Because of the much higher data frequency for PON, we used this variable as further diagnostic, and converted it to POP using a stoichiometric ratio of 16 mol N:mol P.

To map data onto a regular grid we averaged all data that fall within boxes defined by a horizontal resolution of $1^\circ \times 1^\circ$ and 23 depth intervals, centered at 5, 15, 27.5, 45, 65, 87.5, 117.5, 160, 222.5, 310, 435, 610, 847.5, 1160, 1542.5, 1975, 2450, 2950, 3450, 3950, 4450, 4950 and 5450 m. The resulting data set contained 6887 data points for PON, with minimum and maximum concentrations (after conversion to POP) of 0 and 1.69 mmol P m^{-3}, respectively, an average of 0.0266 mmol P m^{-3} and a standard deviation of 0.0499 mmol P m^{-3}. Following this mapping, we interpolated the data onto the NEMO grid. Because of the higher vertical resolution of NEMO, this data set contains more observations, but similar statistics (see Table B1).

Particulate organic matter is usually collected with Niskin bottles and then filtered; thus it entails not only detritus (dead organic particles), but also phytoplankton and possibly a fraction of zooplankton. We therefore compare these observations to the sum of simulated detritus, phytoplankton, plus half of the zooplankton, thereby assuming that microzooplankton is caught in the Niskin bottles and remains on filters for PON analysis.

B2.5 DOP

Most observations of dissolved organic phosphorus applied for model evaluation have been compiled by Angela Landolfi. They include data from cruises 36N, AMT10,AMT12, AMT14, AMT15, AMT16 and AMT17 (Torres-Valdés et al., 2009), the BIOSOPE cruise (Moutin et al., 2008), the North Atlantic (cruise D279, April-May 2004; Landolfi et al., 2016) and the unpublished data form Indian Ocean (cruise CD139, March-April 2002; Landolfi, unpubl.). Coefficient of variation of DOP measurements is about 10% in Landolfi et al. (2016). In the compilation we only included data with a positive (good) quality flag. We further included data from the northern North Pacific, read from Fig. 2 of Yoshimura et al. (2007). Data were gridded onto a $1^\circ \times 1^\circ$ grid with 23 vertical layers, as applied for mapping of PON. After mapping onto this grid we obtained 814 data points in the upper 100 m, with minimum and maximum values of 0 and 3.92 mmol P m^{-3}, an average of 0.178 mmol P m^{-3}, and a standard deviation of 0.21 mmol P m^{-3}. Gridding onto the finer NEMO grid increases the number of observations, but largely maintains the statistics (see Table B1). Note that the majority of the surface observational data (phytoplankton, zooplankton, POP, and DOP) were collected between Spring and Autumn, and potential biases could exist when compared with annual mean model results.

B3 Metrics

To assess the performance of the biogeochemical model we apply six statistical measures and metrics, that account in different ways for potential errors in average concentrations (biases), the spatial variability of observations, and the match to spatial patterns. In particular we evaluated the model bias (absolute, as well as normalised by the observed mean), the model's standard deviation σ_{M} normalised by the standard deviation of observations σ_{O}, the root-mean-squared-error (RMSE), the pattern error or centred RMS difference RMSE'(RMSE minus bias), and the correlation coefficient r between model and observations. All calculations take into account the spatial dimensions of the model, thereby emphasising deviations in the deep ocean, where box thicknesses are large. To investigate the model's representation of dissolved inorganic tracers in different vertical domains, beside the global model fit we also evaluated the metrics in different vertical domains, namely for 0-100 m, 100-200 m, 200-500 m, 500-1000 m, 1000-2000 m and 2000-5000 m. Vertical domains of the organic tracers are surface for phytoplankton, the upper 100 meters for zooplankton and DOP (see also above for treatment of zooplankton observations), and the full domain for POP.

A slight distortion in the physical model (e.g., a current being located slightly off) may cause a large RMSE, and thereby induce a large model error, even if the biogeochemical model is dynamically correct. To account for this, and to compare this model with the results by Ilyina et al. (2013), we further added a seventh metric, namely the Bhattacharyya distance (BD), which evaluates the similarity between observed and simulated frequency distributions of tracers. In particular, to evaluate BD we binned simulated and observed tracer concentrations into $N = 50$ concentration classes over a typical range of concentrations (phosphate: 0-4 mmol P m^{-3}; nitrate: 0-50 mmol N m^{-3}; oxygen: 0-400 mmol O_2 m^{-3}; DIC and alkalinity: 1700-2500 mmol m^{-3}; phytoplankton and zooplankton: 0-0.1 mmol P m^{-3}; POP: 0-0.5 mmol P m^{-3}; DOP: 0-1 mmol P m^{-3}). Examples for different distributions are given in Figures B1 and 16. Following binning, BD was evaluated as

$$BD = -\ln\left(\sum_{i=1}^{N} m_i o_i\right) \tag{B1}$$

where m_i and o_i are the frequencies of simulated and observed model boxes with concentration of class i. We note that BD relates to the Hellinger distance HD:

$$HD = \sqrt{0.5 \sum_{i=1}^{N} (\sqrt{m_i} - \sqrt{o_i})^2} \tag{B2}$$

via $BD = -\ln(1 - HD^2)$. In contrast to BD the Hellinger distance is bounded by $0 \leq HD \leq 1$. Finally, the $L1$ norm of distributions as given by

$$L1 = \sum_{i=1}^{N} |m_i - o_i| \tag{B3}$$

is evaluated. (Note that this norm is bounded by $0 \leq L1 \leq 2$.) Figures B1 and 16 list the different metrics of inorganic and organic tracers in different vertical domains. In all cases, the smaller the area of overlap between the two distributions, the larger the metric.

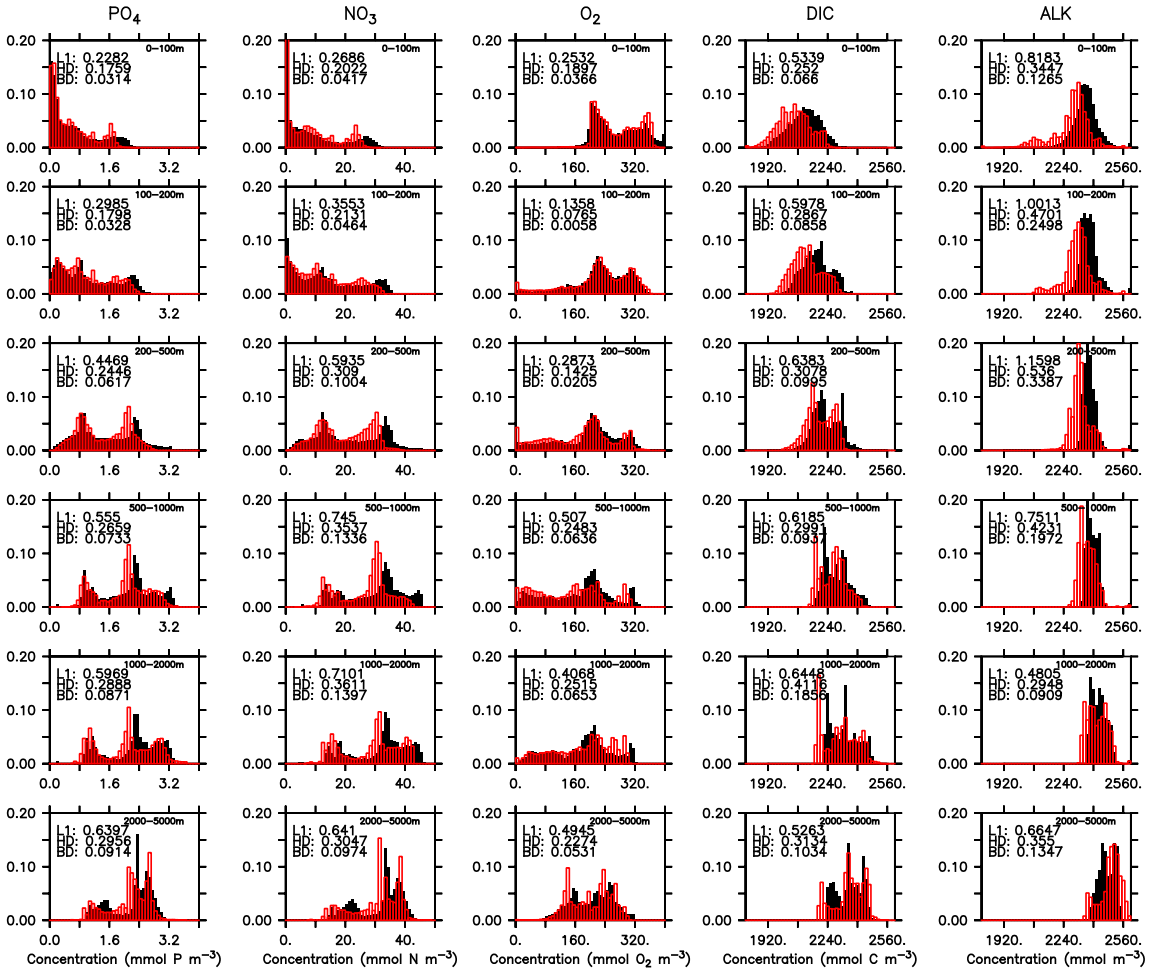

Figure B1. Frequency distribution of phosphate, nitrate, oxygen, DIC and alkalinity (left to right) from observations (black filled bars) and model (red bars) for different vertical domains (top to bottom). Numbers denote three different metrics for the similarity of the distributions, namely $L1$ (Equation B3), HD (Equation B2), and BD (Equation B1).

Table B2. Different metrics for surface (0-100m), total domain (0-8000m) and range of metrics over seven different vertical domains (0-100m, 100-200m, 200-500m, 500-1000m, 1000-2000m, 2000-5000m, 0-8000m) of historical experiments ensemble mean from 1972 to 2013 for PO_4, NO_3, O_2, ALK, 2002 for DIC, and 2005 – 2014 for Phy, Zoo, POP, and DOP. Different metrics include the correlation coefficient r, the root-mean-squared-error RMSE, the pattern error RMSE' (RMSE minus global bias), the global bias in mmol m^{-3}, bias normalised by observed global mean, normalised standard deviation and the Bhattacharyya distance BD, for each model component. Except for BD all metrics have been calculated on a volume-weighted basis. See text for further details.

	PO_4	NO_3	O_2	DIC	ALK	Phy	Zoo	POP	DOP
				Surface (0-100m)					
r	0.888	0.892	0.906	0.779	0.724	0.362	0.133	-	0.107
RMSE	0.306	4.344	27.021	82.414	90.511	0.012	0.010	-	0.408
RMSE'	0.289	4.155	26.000	58.686	63.259	0.012	0.010	-	0.195
Bias	-0.101	-1.269	7.359	-57.861	-64.734	0.004	0.002	-	0.359
Bias (rel.)	-17.5	-18.7	3.0	-2.7	-2.7	26.2	34.8	-	216.6
$\sigma_{\mathrm{M}}/\sigma_{\mathrm{O}}$	0.827	0.837	0.913	1.062	1.309	0.405	0.609	-	0.479
BD	0.031	0.042	0.037	0.066	0.127	0.327	0.068	-	1.261
				Total (0-8000m)					
r	0.946	0.931	0.920	0.946	0.925	-	-	0.419	-
RMSE	0.245	3.975	30.126	38.298	36.639	-	-	0.041	-
RMSE'	0.229	3.575	28.588	36.412	36.502	-	-	0.038	-
Bias	-0.087	-1.738	-9.503	-11.871	-3.163	-	-	-0.014	-
Bias (rel.)	-4.1	-5.7	-5.2	-0.5	-0.1	-	-	-57.3	-
$\sigma_{\mathrm{M}}/\sigma_{\mathrm{O}}$	0.971	0.963	1.048	1.210	1.430	-	-	0.482	-
BD	0.030	0.045	0.016	0.020	0.095	-	-	0.068	-
				Min./Max. of all seven vertical domains					
r	0.89/ 0.96	0.85/ 0.95	0.91/ 0.94	0.78/ 0.95	0.72/ 0.92	-	-	-	-
RMSE	0.20/ 0.34	2.65/ 6.01	22.59/ 46.97	31.06/ 82.41	25.08/ 90.51	-	-	-	-
RMSE'	0.19/ 0.34	2.59/ 4.80	21.84/ 34.17	30.53/ 58.69	22.13/ 63.26	-	-	-	-
Bias	-0.17/ -0.04	-3.62/ -0.54	-32.22/ 7.36	-57.86/ 3.38	-64.73/ 18.79	-	-	-	-
Bias (rel.)	-17.5/ -2.2	-18.7/ -1.7	-21.0/ 3.0	-2.7/ 0.1	-2.7/ 0.8	-	-	-	-
$\sigma_{\mathrm{M}}/\sigma_{\mathrm{O}}$	0.82/ 1.08	0.75/ 1.04	0.91/ 1.11	0.99/ 1.23	1.08/ 1.43	-	-	-	-
BD	0.03/ 0.09	0.04/ 0.14	0.01/ 0.07	0.02/ 0.19	0.09/ 0.34	-	-	-	-

Author contributions. DE, IK, JVD, and LP implemented the MOPS codes into the FOCI; CC and JVD carried out simulations with assistance of SW. All authors discussed the results and wrote the manuscript.

Competing interests. The authors declare that they have no conflict of interest.

Acknowledgements. Parallel supercomputing resources have been provided by the North-German Supercomputing Alliance (HLRN). The authors wish to acknowledge use of the Ferret program of NOAA's Pacific Marine Environmental Laboratory for analysis and graphics in this paper.

Financial support

DE and JVD were supported by the Helmholtz-Gemeinschaft for the research project "Advanced Earth Systm Modelling Capacity" (Grant ZT-0003). CC was supported by the OceanNETs project, which has received funding from the European Union's Horizon 2020 research and innovation program under grant agreement number 869357, and Deutsche Forschungsgemeinschaft (DFG) (project no: CH 2605/1-1). LP was financially supported by the GEOMAR Helmholtz Centre for Ocean Research Kiel and by the project CP1219 of the Cluster of Excellence "The Future Ocean" funded by the DFG.

References

Anderson, L. A. and Sarmiento, J. L.: Redfield ratios of remineralization determined by nutrient data analysis, Global Biogeochemical Cycles, 8, 65–80, https://doi.org/10.1029/93GB03318, 1994.

Arneth, A., Harrison, S. P., Zaehle, S., Tsigaridis, K., Menon, S., Bartlein, P. J., Feichter, J., Korhola, A., Kulmala, M., O'Donnell, D., Schurgers, G., Sorvari, S., and Vesala, T.: Terrestrial biogeochemical feedbacks in the climate system, Nature Geoscience, 3, 525–532, https://doi.org/10.1038/ngeo905, 2010.

Aumont, O., van Hulten, M., Roy-Barman, M., Dutay, J.-C., Éthé, C., and Gehlen, M.: Variable reactivity of particulate organic matter in a global ocean biogeochemical model, Biogeosciences, 14, 2321–2341, https://doi.org/10.5194/bg-14-2321-2017, 2017.

Balch, W., Drapeau, D., Bowler, B., and Booth, E.: Prediction of pelagic calcification rates using satellite measurements, Deep Sea Research Part II: Topical Studies in Oceanography, 54, 478–495, https://doi.org/https://doi.org/10.1016/j.dsr2.2006.12.006, 2007.

Bastos, A., Ciais, P., Barichivich, J., Bopp, L., Brovkin, V., Gasser, T., Peng, S., Pongratz, J., Viovy, N., and Trudinger, C. M.: Re-evaluating the 1940s CO_2 plateau, Biogeosciences, 13, 4877–4897, https://doi.org/10.5194/bg-13-4877-2016, 2016.

Berthet, S., Séférian, R., Bricaud, C., Chevallier, M., Voldoire, A., and Ethé, C.: Evaluation of an Online Grid-Coarsening Algorithm in a Global Eddy-Admitting Ocean Biogeochemical Model, Journal of Advances in Modeling Earth Systems, 11, 1759–1783, https://doi.org/https://doi.org/10.1029/2019MS001644, 2019.

Bhattacharyya, A.: On a Measure of Divergence between Two Multinomial Populations, Sankhyā: The Indian Journal of Statistics (1933-1960), 7, 401–406, 1946.

Bianchi, D., Dunne, J. P., Sarmiento, J. L., and Galbraith, E. D.: Data-based estimates of suboxia, denitrification, and N2O production in the ocean and their sensitivities to dissolved O2, Global Biogeochemical Cycles, 26, https://doi.org/https://doi.org/10.1029/2011GB004209, 2012.

Breitbarth, E., Oschlies, A., and LaRoche, J.: Physiological constraints on the global distribution of *Trichodesmium* - effect of temperature on diazotrophy, Biogeosciences, 4, 53–61, https://doi.org/10.5194/bg-4-53-2007, 2007.

Brovkin, V., Raddatz, T., Reick, C. H., Claussen, M., and Gayler, V.: Global biogeophysical interactions between forest and climate, Geophysical Research Letters, 36, https://doi.org/https://doi.org/10.1029/2009GL037543, 2009.

Buitenhuis, E. T., Rivkin, R. B., Sailley, S., and Le Quéré, C.: Global distributions of microzooplankton abundance and biomass - Gridded data product (NetCDF) - Contribution to the MAREDAT World Ocean Atlas of Plankton Functional Types, https://doi.org/10.1594/PANGAEA.779970, 2012.

Buitenhuis, E. T., Hashioka, T., and Quéré, C. L.: Combined constraints on global ocean primary production using observations and models, Global Biogeochemical Cycles, 27, 847–858, https://doi.org/https://doi.org/10.1002/gbc.20074, 2013.

Buitenhuis, E. T., Le Quéré, C., Bednaršek, N., and Schiebel, R.: Large Contribution of Pteropods to Shallow CaCO3 Export, Global Biogeochemical Cycles, 33, 458–468, https://doi.org/https://doi.org/10.1029/2018GB006110, 2019.

Cabré, A., Marinov, I., Bernardello, R., and Bianchi, D.: Oxygen minimum zones in the tropical Pacific across CMIP5 models: mean state differences and climate change trends, Biogeosciences, 12, 5429–5454, https://doi.org/10.5194/bg-12-5429-2015, 2015.

Carr, M.-E., Friedrichs, M. A., Schmeltz, M., Aita, M. N., Antoine, D., Arrigo, K. R., Asanuma, I., Aumont, O., Barber, R., Behrenfeld, M., Bidigare, R., Buitenhuis, E. T., Campbell, J., Ciotti, A., Dierssen, H., Dowell, M., Dunne, J., Esaias, W., Gentili, B., Gregg, W., Groom, S., Hoepffner, N., Ishizaka, J., Kameda, T., Quere, C. L., Lohrenz, S., Marra, J., Melin, F., Moore, K., Morel, A., Reddy, T. E., Ryan, J., Scardi, M., Smyth, T., Turpie, K., Tilstone, G., Waters, K., and Yamanaka, Y.: A comparison of global esti-

mates of marine primary production from ocean color, Deep Sea Research Part II: Topical Studies in Oceanography, 53, 741 – 770, https://doi.org/https://doi.org/10.1016/j.dsr2.2006.01.028, 2006.

Cheng, L., Trenberth, K. E., Fasullo, J., Boyer, T., Abraham, J., and Zhu, J.: Improved estimates of ocean heat content from 1960 to 2015, Science Advances, 3, https://doi.org/10.1126/sciadv.1601545, https://advances.sciencemag.org/content/3/3/e1601545, 2017.

Debreu, L., Vouland, C., and Blayo, E.: AGRIF: Adaptive grid refinement in Fortran, Computers Geosciences, 34, 8 – 13, https://doi.org/https://doi.org/10.1016/j.cageo.2007.01.009, 2008.

DeVries, T., Deutsch, C., Primeau, F., Chang, B., and Devol, A.: Global rates of water-column denitrification derived from nitrogen gas measurements, Nature Geoscience, 5, 2012.

DeVries, T., Deutsch, C., Rafter, P. A., and Primeau, F.: Marine denitrification rates determined from a global 3-D inverse model, Biogeosciences, 10, 2481–2496, https://doi.org/10.5194/bg-10-2481-2013, 2013.

Dickson, A., Sabine, C., and Christian, J.: Guide to best practices for ocean CO_2 measurements, PICES Special Publication 3, 191 pp., 2007.

Dickson, A. G.: Standard potential of the reaction: AgCl(s) + 12H2(g) = Ag(s) + HCl(aq), and and the standard acidity constant of the ion HSO_4^- in synthetic sea water from 273.15 to 318.15 K, The Journal of Chemical Thermodynamics, 22, 113 – 127, https://doi.org/https://doi.org/10.1016/0021-9614(90)90074-Z, 1990.

Dietze, H. and Loeptien, U.: Revisiting "nutrient trapping" in global coupled biogeochemical ocean circulation models, Global Biogeochemical Cycles, 27, 265–284, https://doi.org/https://doi.org/10.1002/gbc.20029, 2013.

Dong, F., Li, Y., Wang, B., Huang, W., Shi, Y., and Dong, W.: Global Air–Sea CO2 Flux in 22 CMIP5 Models: Multiyear Mean and Interannual Variability, Journal of Climate, 29, 2407 – 2431, https://doi.org/10.1175/JCLI-D-14-00788.1, https://journals.ametsoc.org/view/journals/clim/29/7/jcli-d-14-00788.1.xml, 2016.

Dunne, J. P., Sarmiento, J. L., and Gnanadesikan, A.: A synthesis of global particle export from the surface ocean and cycling through the ocean interior and on the seafloor, Global Biogeochemical Cycles, 21, https://doi.org/10.1029/2006GB002907, 2007.

Duteil, O., Koeve, W., Oschlies, A., Aumont, O., Bianchi, D., Bopp, L., Galbraith, E., Matear, R., Moore, J. K., Sarmiento, J. L., and Segschneider, J.: Preformed and regenerated phosphate in ocean general circulation models: can right total concentrations be wrong?, Biogeosciences, 9, 1797–1807, https://doi.org/10.5194/bg-9-1797-2012, 2012.

Eppley, R. W.: Temperature and phytoplankton growth in the sea, Fish. Bull., 70, 1063–1085, 1972.

Eugster, O. and Gruber, N.: A probabilistic estimate of global marine N-fixation and denitrification, Global Biogeochemical Cycles, 26, https://doi.org/https://doi.org/10.1029/2012GB004300, 2012.

Evans, G. T. and Garçon, V.: One–dimensional models of water column biogeochemistry, JGOFS Report 23, Scientific Committee on Oceanic Research, Bergen, Norway, 85 pp., 1997.

Evans, G. T. and Parslow, J. S.: A Model of Annual Plankton Cycles, Biological Oceanography, 3, 327–347, https://doi.org/10.1080/01965581.1985.10749478, 1985.

Eyring, V., Bony, S., Meehl, G. A., Senior, C. A., Stevens, B., Stouffer, R. J., and Taylor, K. E.: Overview of the Coupled Model Intercomparison Project Phase 6 (CMIP6) experimental design and organization, Geoscientific Model Development, 9, 1937–1958, https://doi.org/10.5194/gmd-9-1937-2016, 2016.

Falkowski, P. G.: Evolution of the nitrogen cycle and its influence on the biological sequestration of CO2 in the ocean, Nature, 387, 272–275, https://doi.org/10.1038/387272a0, 1997.

Fassbender, A. J., Sabine, C. L., and Palevsky, H. I.: Nonuniform ocean acidification and attenuation of the ocean carbon sink, Geophysical Research Letters, 44, 8404–8413, https://doi.org/https://doi.org/10.1002/2017GL074389, 2017.

Follows, M. J., Ito, T., and Dutkiewicz, S.: On the solution of the carbonate chemistry system in ocean biogeochemistry models, Ocean Modelling, 12, 290 – 301, https://doi.org/https://doi.org/10.1016/j.ocemod.2005.05.004, 2006.

Friedlingstein, P., Cox, P., Betts, R., Bopp, L., von Bloh, W., Brovkin, V., Cadule, P., Doney, S., Eby, M., Fung, I., Bala, G., John, J., Jones, C., Joos, F., Kato, T., Kawamiya, M., Knorr, W., Lindsay, K., Matthews, H. D., Raddatz, T., Rayner, P., Reick, C., Roeckner, E., Schnitzler, K.-G., Schnur, R., Strassmann, K., Weaver, A. J., Yoshikawa, C., and Zeng, N.: Climate–Carbon Cycle Feedback Analysis: Results from the C4MIP Model Intercomparison, Journal of Climate, 19, 3337–3353, https://doi.org/10.1175/JCLI3800.1, 2006.

Friedlingstein, P., O'Sullivan, M., Jones, M. W., Andrew, R. M., Hauck, J., Olsen, A., Peters, G. P., Peters, W., Pongratz, J., Sitch, S., Le Quéré, C., Canadell, J. G., Ciais, P., Jackson, R. B., Alin, S., Aragão, L. E. O. C., Arneth, A., Arora, V., Bates, N. R., Becker, M., Benoit-Cattin, A., Bittig, H. C., Bopp, L., Bultan, S., Chandra, N., Chevallier, F., Chini, L. P., Evans, W., Florentie, L., Forster, P. M., Gasser, T., Gehlen, M., Gilfillan, D., Gkritzalis, T., Gregor, L., Gruber, N., Harris, I., Hartung, K., Haverd, V., Houghton, R. A., Ilyina, T., Jain, A. K., Joetzjer, E., Kadono, K., Kato, E., Kitidis, V., Korsbakken, J. I., Landschützer, P., Lefèvre, N., Lenton, A., Lienert, S., Liu, Z., Lombardozzi, D., Marland, G., Metzl, N., Munro, D. R., Nabel, J. E. M. S., Nakaoka, S.-I., Niwa, Y., O'Brien, K., Ono, T., Palmer, P. I., Pierrot, D., Poulter, B., Resplandy, L., Robertson, E., Rödenbeck, C., Schwinger, J., Séférian, R., Skjelvan, I., Smith, A. J. P., Sutton, A. J., Tanhua, T., Tans, P. P., Tian, H., Tilbrook, B., van der Werf, G., Vuichard, N., Walker, A. P., Wanninkhof, R., Watson, A. J., Willis, D., Wiltshire, A. J., Yuan, W., Yue, X., and Zaehle, S.: Global Carbon Budget 2020, Earth System Science Data, 12, 3269–3340, https://doi.org/10.5194/essd-12-3269-2020, 2020.

Frölicher, T. L., Sarmiento, J. L., Paynter, D. J., Dunne, J. P., Krasting, J. P., and Winton, M.: Dominance of the Southern Ocean in Anthropogenic Carbon and Heat Uptake in CMIP5 Models, Journal of Climate, 28, 862–886, https://doi.org/10.1175/JCLI-D-14-00117.1, 2015.

Fu, W., Randerson, J. T., and Moore, J. K.: Climate change impacts on net primary production (NPP) and export production (EP) regulated by increasing stratification and phytoplankton community structure in the CMIP5 models, Biogeosciences, 13, 5151–5170, https://doi.org/10.5194/bg-13-5151-2016, https://bg.copernicus.org/articles/13/5151/2016/, 2016.

Garcia, H. E., Locarnini, R. A., Boyer, T. P., Antonov, J. I., Mishonov, A. V., Baranova, O. K., Zweng, M. M., Reagan, J. R., and Johnson, D. R.: Dissolved Oxygen, Apparent Oxygen Utilization, and Oxygen Saturation, in: World Ocean Atlas 2013, edited by Levitus, S., vol. 3, NOAA Atlas NESDIS 75, https://doi.org/http://www.nodc.noaa.gov/OC5/indprod.html, 2013a.

Garcia, H. E., Locarnini, R. A., Boyer, T. P., Antonov, J. I., Mishonov, A. V., Baranova, O. K., Zweng, M. M., Reagan, J. R., and Johnson, D. R.: Dissolved Inorganic Nutrients (phosphate, nitrate, silicate), in: World Ocean Atlas 2013, edited by Levitus, S., vol. 4, NOAA Atlas NESDIS 76, http://www.nodc.noaa.gov/OC5/indprod.html, 2013b.

Gruber, N., Clement, D., Carter, B. R., Feely, R. A., van Heuven, S., Hoppema, M., Ishii, M., Key, R. M., Kozyr, A., Lauvset, S. K., Lo Monaco, C., Mathis, J. T., Murata, A., Olsen, A., Perez, F. F., Sabine, C. L., Tanhua, T., and Wanninkhof, R.: The oceanic sink for anthropogenic CO2 from 1994 to 2007, Science, 363, 1193–1199, https://doi.org/10.1126/science.aau5153, https://science.sciencemag.org/content/363/6432/1193, 2019.

Guidi, L., Legendre, L., Reygondeau, G., Uitz, J., Stemmann, L., and Henson, S. A.: A new look at ocean carbon remineralization for estimating deepwater sequestration, Global Biogeochemical Cycles, 29, 1044–1059, https://doi.org/https://doi.org/10.1002/2014GB005063, 2015.

Hauck, J., Zeising, M., Le Quéré, C., Gruber, N., Bakker, D. C. E., Bopp, L., Chau, T. T. T., Gürses, Ö., Ilyina, T., Landschützer, P., Lenton, A., Resplandy, L., Rödenbeck, C., Schwinger, J., and Séférian, R.: Consistency and Challenges in the Ocean Carbon Sink Estimate for the Global Carbon Budget, Frontiers in Marine Science, 7, 852, https://doi.org/10.3389/fmars.2020.571720, 2020.

Hellinger, E.: Neue Begründung der Theorie quadratischer Formen von unendlichvielen Veränderlichen., Journal für die reine und angewandte Mathematik, 1909, 210 – 271, https://doi.org/https://doi.org/10.1515/crll.1909.136.210, 1909.

Holling, C. S. and Buckingham, S.: A behavioral model of predator-prey functional responses, Behavioral Science, 21, 183–195, https://doi.org/10.1002/bs.3830210305, 1976.

Honjo, S., Manganini, S. J., Krishfield, R. A., and Francois, R.: Particulate organic carbon fluxes to the ocean interior and factors controlling the biological pump: A synthesis of global sediment trap programs since 1983, Progress in Oceanography, 76, 217 – 285, https://doi.org/https://doi.org/10.1016/j.pocean.2007.11.003, 2008.

Iglesias-Rodriguez, M. D., Armstrong, R., Feely, R., Hood, R., Kleypas, J., Milliman, J. D., Sabine, C., and Sarmiento, J.: Progress made in study of ocean's calcium carbonate budget, Eos, Transactions American Geophysical Union, 83, 365–375, https://doi.org/https://doi.org/10.1029/2002EO000267, 2002.

Ilyina, T., Six, K. D., Segschneider, J., Maier-Reimer, E., Li, H., and Núñez-Riboni, I.: Global ocean biogeochemistry model HAMOCC: Model architecture and performance as component of the MPI-Earth system model in different CMIP5 experimental realizations, Journal of Advances in Modeling Earth Systems, 5, 287–315, https://doi.org/10.1029/2012MS000178, 2013.

IPCC: Climate Change and Land: an IPCC special report on climate change, desertification, land degradation, sustainable land management, food security, and greenhouse gas fluxes in terrestrial ecosystems, in press edn., 2019.

Ishii, M., Fukuda, Y., Hirahara, S., Yasui, S., Suzuki, T., and Sato, K.: Accuracy of Global Upper Ocean Heat Content Estimation Expected from Present Observational Data Sets, SOLA, 13, 163–167, https://doi.org/10.2151/sola.2017-030, 2017.

Jones, C. D., Arora, V., Friedlingstein, P., Bopp, L., Brovkin, V., Dunne, J., Graven, H., Hoffman, F., Ilyina, T., John, J. G., Jung, M., Kawamiya, M., Koven, C., Pongratz, J., Raddatz, T., Randerson, J. T., and Zaehle, S.: C4MIP – The Coupled Climate–Carbon Cycle Model Intercomparison Project: experimental protocol for CMIP6, Geoscientific Model Development, 9, 2853–2880, https://doi.org/10.5194/gmd-9-2853-2016, 2016.

Khatiwala, S.: A computational framework for simulation of biogeochemical tracers in the ocean, Global Biogeochemical Cycles, 21, https://doi.org/https://doi.org/10.1029/2007GB002923, 2007.

Khatiwala, S., Graven, H., Payne, S., and Heimbach, P.: Changes to the Air-Sea Flux and Distribution of Radiocarbon in the Ocean Over the 21st Century, Geophysical Research Letters, 45, 5617–5626, https://doi.org/https://doi.org/10.1029/2018GL078172, 2018.

Kiko, R., Biastoch, A., Brandt, P., Cravatte, S., Hauss, H., Hummels, R., Kriest, I., Marin, F., McDonnell, A. M. P., Oschlies, A., Picheral, M., Schwarzkopf, F. U., Thurnherr, A. M., and Stemmann, L.: Biological and physical influences on marine snowfall at the equator, Nature Geoscience, 10, 852–858, https://doi.org/10.1038/ngeo3042, 2017.

Kiko, R., Brandt, P., Christiansen, S., Faustmann, J., Kriest, I., Rodrigues, E., Schütte, F., and Hauss, H.: Zooplankton-Mediated Fluxes in the Eastern Tropical North Atlantic, Frontiers in Marine Science, 7, 358, https://doi.org/10.3389/fmars.2020.00358, 2020.

Kriest, I. and Oschlies, A.: On the treatment of particulate organic matter sinking in large-scale models of marine biogeochemical cycles, Biogeosciences, 5, 55–72, https://doi.org/10.5194/bg-5-55-2008, 2008.

Kriest, I. and Oschlies, A.: Swept under the carpet: organic matter burial decreases global ocean biogeochemical model sensitivity to remineralization length scale, Biogeosciences, 10, 8401–8422, https://doi.org/10.5194/bg-10-8401-2013, 2013.

Kriest, I. and Oschlies, A.: MOPS-1.0: towards a model for the regulation of the global oceanic nitrogen budget by marine biogeochemical processes, Geoscientific Model Development, 8, 2929–2957, https://doi.org/10.5194/gmd-8-2929-2015, 2015.

Kriest, I., Sauerland, V., Khatiwala, S., Srivastav, A., and Oschlies, A.: Calibrating a global three-dimensional biogeochemical ocean model (MOPS-1.0), Geosci. Model Dev., 10, 127–154, https://doi.org/10.5194/gmd-10-127-2017, 2017.

Kriest, I., Kähler, P., Koeve, W., Kvale, K., Sauerland, V., and Oschlies, A.: One size fits all? Calibrating an ocean biogeochemistry model for different circulations, Biogeosciences, 17, 3057–3082, https://doi.org/10.5194/bg-17-3057-2020, 2020.

Kwiatkowski, L., Yool, A., Allen, J. I., Anderson, T. R., Barciela, R., Buitenhuis, E. T., Butenschön, M., Enright, C., Halloran, P. R., Le Quéré, C., de Mora, L., Racault, M.-F., Sinha, B., Totterdell, I. J., and Cox, P. M.: iMarNet: an ocean biogeochemistry model intercomparison project within a common physical ocean modelling framework, Biogeosciences, 11, 7291–7304, https://doi.org/10.5194/bg-11-7291-2014, 2014.

Kwiatkowski, L., Torres, O., Bopp, L., Aumont, O., Chamberlain, M., Christian, J. R., Dunne, J. P., Gehlen, M., Ilyina, T., John, J. G., Lenton, A., Li, H., Lovenduski, N. S., Orr, J. C., Palmieri, J., Santana-Falcón, Y., Schwinger, J., Séférian, R., Stock, C. A., Tagliabue, A., Takano, Y., Tjiputra, J., Toyama, K., Tsujino, H., Watanabe, M., Yamamoto, A., Yool, A., and Ziehn, T.: Twenty-first century ocean warming, acidification, deoxygenation, and upper-ocean nutrient and primary production decline from CMIP6 model projections, Biogeosciences, 17, 3439–3470, https://doi.org/10.5194/bg-17-3439-2020, 2020.

Landolfi, A., Dietze, H., and Volpe, G.: Longitudinal variability of organic nutrients in the North Atlantic subtropical gyre, Deep Sea Research Part I: Oceanographic Research Papers, 111, 50–60, https://doi.org/https://doi.org/10.1016/j.dsr.2015.11.009, 2016.

Landschützer, P., N. G. and Bakker, D.: An updated observation-based global monthly gridded sea surface pCO2 and air-sea CO2 flux product from 1982 through 2015 and its monthly climatology (NCEI Accession 0160558). Version 2.2. NOAA National Centers for Environmental Information. Dataset. [2017-07-11], 2017.

Lauvset, S. K., Key, R. M., Olsen, A., van Heuven, S., Velo, A., Lin, X., Schirnick, C., Kozyr, A., Tanhua, T., Hoppema, M., Jutterström, S., Steinfeldt, R., Jeansson, E., Ishii, M., Perez, F. F., Suzuki, T., and Watelet, S.: A new global interior ocean mapped climatology: GLODAP version 2, Earth System Science Data, 8, 325–340, https://doi.org/10.5194/essd-8-325-2016, 2016.

Le Quéré, C., Rödenbeck, C., Buitenhuis, E. T., Conway, T. J., Langenfelds, R., Gomez, A., Labuschagne, C., Ramonet, M., Nakazawa, T., Metzl, N., Gillett, N., and Heimann, M.: Saturation of the Southern Ocean CO2 Sink Due to Recent Climate Change, Science, 316, 1735, https://doi.org/10.1126/science.1136188, 2007.

Lee, K.: Global net community production estimated from the annual cycle of surface water total dissolved inorganic carbon, Limnology and Oceanography, 46, 1287–1297, https://doi.org/https://doi.org/10.4319/lo.2001.46.6.1287, 2001.

Lee, K., Kim, T.-W., Byrne, R. H., Millero, F. J., Feely, R. A., and Liu, Y.-M.: The universal ratio of boron to chlorinity for the North Pacific and North Atlantic oceans, Geochimica et Cosmochimica Acta, 74, 1801 – 1811, https://doi.org/https://doi.org/10.1016/j.gca.2009.12.027, 2010.

Liddicoat, S. K., Wiltshire, A. J., Jones, C. D., Arora, V. K., Brovkin, V., Cadule, P., Hajima, T., Lawrence, D. M., Pongratz, J., Schwinger, J., Séférian, R., Tjiputra, J. F., and Ziehn, T.: Compatible Fossil Fuel CO2 Emissions in the CMIP6 Earth System Models' Historical and Shared Socioeconomic Pathway Experiments of the Twenty-First Century, Journal of Climate, 34, 2853 – 2875, https://doi.org/10.1175/JCLI-D-19-0991.1, 2021.

Lin, D., Xia, J., and Wan, S.: Climate warming and biomass accumulation of terrestrial plants: a meta-analysis, New Phytologist, 188, 187–198, https://doi.org/https://doi.org/10.1111/j.1469-8137.2010.03347.x, 2010.

Luo, Y.-W., Doney, S. C., Anderson, L. A., Benavides, M., Berman-Frank, I., Bode, A., Bonnet, S., Boström, K. H., Böttjer, D., Capone, D. G., Carpenter, E. J., Chen, Y. L., Church, M. J., Dore, J. E., Falcón, L. I., Fernández, A., Foster, R. A., Furuya, K., Gómez, F., Gundersen, K., Hynes, A. M., Karl, D. M., Kitajima, S., Langlois, R. J., LaRoche, J., Letelier, R. M., Marañón, E., McGillicuddy Jr., D. J., Moisander, P. H., Moore, C. M., Mouriño Carballido, B., Mulholland, M. R., Needoba, J. A., Orcutt, K. M., Poulton, A. J., Rahav, E., Raimbault, P., Rees, A. P., Riemann, L., Shiozaki, T., Subramaniam, A., Tyrrell, T., Turk-Kubo, K. A., Varela, M., Villareal, T. A., Webb, E. A., White,

A. E., Wu, J., and Zehr, J. P.: Database of diazotrophs in global ocean: abundance, biomass and nitrogen fixation rates, Earth System Science Data, 4, 47–73, https://doi.org/10.5194/essd-4-47-2012, 2012.

Lutz, M. J., Caldeira, K., Dunbar, R. B., and Behrenfeld, M. J.: Seasonal rhythms of net primary production and particulate organic carbon flux to depth describe the efficiency of biological pump in the global ocean, Journal of Geophysical Research: Oceans, 112, https://doi.org/10.1029/2006JC003706, 2007.

Madec, G.: NEMO ocean engine, Note du Pôle de modélisation, Institut Pierre-Simon Laplace (IPSL), France, No 27, ISSN No 1288-1619, 2016.

Martin, J. H., Knauer, G. A., Karl, D. M., and Broenkow, W. W.: VERTEX: carbon cycling in the northeast Pacific, Deep Sea Research Part A. Oceanographic Research Papers, 34, 267 – 285, https://doi.org/https://doi.org/10.1016/0198-0149(87)90086-0, 1987.

Martiny, A. C., Vrugt, J. A., and Lomas, M. W.: Concentrations and ratios of particulate organic carbon, nitrogen, and phosphorus in the global ocean, Scientific Data, 1, https://doi.org/10.1038/sdata.2014.48, 2014.

Matthes, K., Biastoch, A., Wahl, S., Harlaß, J., Martin, T., Brücher, T., Drews, A., Ehlert, D., Getzlaff, K., Krüger, F., Rath, W., Scheinert, M., Schwarzkopf, F. U., Bayr, T., Schmidt, H., and Park, W.: The Flexible Ocean and Climate Infrastructure version 1 (FOCI1): mean state and variability, Geoscientific Model Development, 13, 2533–2568, https://doi.org/10.5194/gmd-13-2533-2020, 2020.

McCarthy, G., Smeed, D., Johns, W., Frajka-Williams, E., Moat, B., Rayner, D., Baringer, M., Meinen, C., Collins, J., and Bryden, H.: Measuring the Atlantic Meridional Overturning Circulation at 26°N, Progress in Oceanography, 130, 91–111, https://doi.org/https://doi.org/10.1016/j.pocean.2014.10.006, 2015.

Melin, F.: GMIS - MODIS-AQUA Monthly climatology sea surface Chlorophyll-a concentration (9km) in $mg.m^{-3}$. European Commission, Joint Research Centre (JRC) [Dataset], 2013.

Moriarty, R. and O'Brien, T. D.: Distribution of mesozooplankton biomass in the global ocean, Earth System Science Data, 5, 45–55, https://doi.org/10.5194/essd-5-45-2013, 2013.

Morice, C. P., Kennedy, J. J., Rayner, N. A., Winn, J. P., Hogan, E., Killick, R. E., Dunn, R. J. H., Osborn, T. J., Jones, P. D., and Simpson, I. R.: An Updated Assessment of Near-Surface Temperature Change From 1850: The HadCRUT5 Data Set, Journal of Geophysical Research: Atmospheres, 126, e2019JD032 361, https://doi.org/https://doi.org/10.1029/2019JD032361, 2021.

Morris, A. and Riley, J.: The bromide/chlorinity and sulphate/chlorinity ratio in sea water, Deep Sea Research and Oceanographic Abstracts, 13, 699 – 705, https://doi.org/https://doi.org/10.1016/0011-7471(66)90601-2, 1966.

Moutin, T., Karl, D. M., Duhamel, S., Rimmelin, P., Raimbault, P., Van Mooy, B. A. S., and Claustre, H.: Phosphate availability and the ultimate control of new nitrogen input by nitrogen fixation in the tropical Pacific Ocean, Biogeosciences, 5, 95–109, https://doi.org/10.5194/bg-5-95-2008, 2008.

Muller-Karger, F. E., Varela, R., Thunell, R., Luerssen, R., Hu, C., and Walsh, J. J.: The importance of continental margins in the global carbon cycle, Geophysical Research Letters, 32, https://doi.org/https://doi.org/10.1029/2004GL021346, 2005.

Oka, A.: Ocean carbon pump decomposition and its application to CMIP5 earth system model simulations, Progress in Earth and Planetary Science, 7, 25, https://doi.org/10.1186/s40645-020-00338-y, 2020.

Olsen, A., Key, R. M., van Heuven, S., Lauvset, S. K., Velo, A., Lin, X., Schirnick, C., Kozyr, A., Tanhua, T., Hoppema, M., Jutterström, S., Steinfeldt, R., Jeansson, E., Ishii, M., Pérez, F. F., and Suzuki, T.: The Global Ocean Data Analysis Project version 2 (GLODAPv2) – an internally consistent data product for the world ocean, Earth System Science Data, 8, 297–323, https://doi.org/10.5194/essd-8-297-2016, 2016.

Orr, J. C., Najjar, R., Sabine, C. L., and Joos, F.: Abiotic-HOWTO, Internal OCMIP Report, LSCE/CEA Saclay, Gifsur- Yvette, France, 25 pp., 1999.

Orr, J. C., Najjar, R. G., Aumont, O., Bopp, L., Bullister, J. L., Danabasoglu, G., Doney, S. C., Dunne, J. P., Dutay, J.-C., Graven, H., Griffies, S. M., John, J. G., Joos, F., Levin, I., Lindsay, K., Matear, R. J., McKinley, G. A., Mouchet, A., Oschlies, A., Romanou, A., Schlitzer, R., Tagliabue, A., Tanhua, T., and Yool, A.: Biogeochemical protocols and diagnostics for the CMIP6 Ocean Model Intercomparison Project (OMIP), Geoscientific Model Development, 10, 2169–2199, https://doi.org/10.5194/gmd-10-2169-2017, 2017.

Oschlies, A., Brandt, P., Stramma, L., and Schmidtko, S.: Drivers and mechanisms of ocean deoxygenation, Nature Geoscience, 11, 467–473, https://doi.org/10.1038/s41561-018-0152-2, 2018.

Oschlies, A., Koeve, W., Landolfi, A., and Kähler, P.: Loss of fixed nitrogen causes net oxygen gain in a warmer future ocean, Nature Communications, 10, 2805, https://doi.org/10.1038/s41467-019-10813-w, 2019.

Paulmier, A., Kriest, I., and Oschlies, A.: Stoichiometries of remineralisation and denitrification in global biogeochemical ocean models, Biogeosciences, 6, 923–935, https://doi.org/10.5194/bg-6-923-2009, 2009.

Paulsen, H., Ilyina, T., Jungclaus, J. H., Six, K. D., and Stemmler, I.: Light absorption by marine cyanobacteria affects tropical climate mean state and variability, Earth System Dynamics, 9, 1283–1300, https://doi.org/10.5194/esd-9-1283-2018, 2018.

Pugnaire, F. I., Morillo, J., Peñuelas, J., Reich, P. B., Bardgett, R. D., Gaxiola, A., Wardle, D. A., and van der Putten, W. H.: Climate change effects on plant-soil feedbacks and consequences for biodiversity and functioning of terrestrial ecosystems, Science Advances, 5, eaaz1834, https://doi.org/10.1126/sciadv.aaz1834, 2019.

Qu, B., Song, J., Li, X., Yuan, H., Zhang, K., and Xu, S.: Global air-sea CO2 exchange flux since 1980s: results from CMIP6 Earth System Models, Journal of Oceanology and Limnology, https://doi.org/10.1007/s00343-021-1096-8, 2022.

Rayner, N. A., Parker, D. E., Horton, E. B., Folland, C. K., Alexander, L. V., Rowell, D. P., Kent, E. C., and Kaplan, A.: Global analyses of sea surface temperature, sea ice, and night marine air temperature since the late nineteenth century, Journal of Geophysical Research: Atmospheres, 108, https://doi.org/https://doi.org/10.1029/2002JD002670, 2003.

Reick, C. H., Raddatz, T., Brovkin, V., and Gayler, V.: Representation of natural and anthropogenic land cover change in MPI-ESM, Journal of Advances in Modeling Earth Systems, 5, 459–482, https://doi.org/https://doi.org/10.1002/jame.20022, 2013.

Riebesell, U., Körtzinger, A., and Oschlies, A.: Sensitivities of marine carbon fluxes to ocean change, Proceedings of the National Academy of Sciences, 106, 20 602–20 609, https://doi.org/10.1073/pnas.0813291106, 2009.

Riley, J. P.: The occurence of anomalously high fluoride concentrations in the North Atlantic, Deep-Sea Res., 12, 1965.

Sabine, C. L., Feely, R. A., Gruber, N., Key, R. M., Lee, K., Bullister, J. L., Wanninkhof, R., Wong, C. S., Wallace, D. W. R., Tilbrook, B., Millero, F. J., Peng, T.-H., Kozyr, A., Ono, T., and Rios, A. F.: The Oceanic Sink for Anthropogenic CO2, Science, 305, 367–371, https://doi.org/10.1126/science.1097403, 2004.

Sarmiento, J. L. and Gruber, N.: Sinks for Anthropogenic Carbon, Physics Today, 55, 30–36, https://doi.org/10.1063/1.1510279, 2002.

Sathyendranath, S., Stuart, V., Nair, A., Oka, K., Nakane, T., Bouman, H., Forget, M., Maass, H., and Platt, T.: Carbon-to-chlorophyll ratio and growth rate of phytoplankton in the sea, Marine Ecology Progress Series, 383, 73–84, 2009.

Schmidtko, S., Stramma, L., and Visbeck, M.: Decline in global oceanic oxygen content during the past five decades, Nature, 542, 335–339, https://doi.org/10.1038/nature21399, 2017.

Schmittner, A., Oschlies, A., Matthews, H. D., and Galbraith, E. D.: Future changes in climate, ocean circulation, ecosystems, and biogeochemical cycling simulated for a business-as-usual CO2 emission scenario until year 4000 AD, Global Biogeochemical Cycles, 22, n/a–n/a, https://doi.org/10.1029/2007GB002953, gB1013, 2008.

Schultz, M. G., Stadtler, S., Schröder, S., Taraborrelli, D., Franco, B., Krefting, J., Henrot, A., Ferrachat, S., Lohmann, U., Neubauer, D., Siegenthaler-Le Drian, C., Wahl, S., Kokkola, H., Kühn, T., Rast, S., Schmidt, H., Stier, P., Kinnison, D., Tyndall, G. S., Orlando, J. J., and Wespes, C.: The chemistry–climate model ECHAM6.3-HAM2.3-MOZ1.0, Geoscientific Model Development, 11, 1695–1723, https://doi.org/10.5194/gmd-11-1695-2018, 2018.

Séférian, R., Bopp, L., Gehlen, M., Orr, J. C., Ethé, C., Cadule, P., Aumont, O., Salas y Mélia, D., Voldoire, A., and Madec, G.: Skill assessment of three earth system models with common marine biogeochemistry, Climate Dynamics, 40, 2549–2573, https://doi.org/10.1007/s00382-012-1362-8, 2013.

Séférian, R., Berthet, S., Yool, A., Palmiéri, J., Bopp, L., Tagliabue, A., Kwiatkowski, L., Aumont, O., Christian, J., Dunne, J., Gehlen, M., Ilyina, T., John, J. G., Li, H., Long, M. C., Luo, J. Y., Nakano, H., Romanou, A., Schwinger, J., Stock, C., Santana-Falcón, Y., Takano, Y., Tjiputra, J., Tsujino, H., Watanabe, M., Wu, T., Wu, F., and Yamamoto, A.: Tracking Improvement in Simulated Marine Biogeochemistry Between CMIP5 and CMIP6, Current Climate Change Reports, 6, 95–119, https://doi.org/10.1007/s40641-020-00160-0, 2020.

Siegel, D. A., Buesseler, K. O., Doney, S. C., Sailley, S. F., Behrenfeld, M. J., and Boyd, P. W.: Global assessment of ocean carbon export by combining satellite observations and food-web models, Global Biogeochemical Cycles, 28, 181–196, https://doi.org/https://doi.org/10.1002/2013GB004743, 2014.

Smith, E. L.: Photosynthesis in Relation to Light and Carbon Dioxide, Proceedings of the National Academy of Sciences of the United States of America, 22, 504–511, https://doi.org/10.1073/pnas.22.8.504, 1936.

Somes, C. J., Oschlies, A., and Schmittner, A.: Isotopic constraints on the pre-industrial oceanic nitrogen budget, Biogeosciences, 10, 5889–5910, https://doi.org/10.5194/bg-10-5889-2013, 2013.

Somes, C. J., Dale, A. W., Wallmann, K., Scholz, F., Yao, W., Oschlies, A., Muglia, J., Schmittner, A., and Achterberg, E. P.: Constraining Global Marine Iron Sources and Ligand-Mediated Scavenging Fluxes With GEOTRACES Dissolved Iron Measurements in an Ocean Biogeochemical Model, Global Biogeochemical Cycles, 35, e2021GB006 948, https://doi.org/https://doi.org/10.1029/2021GB006948, https://agupubs.onlinelibrary.wiley.com/doi/abs/10.1029/2021GB006948, e2021GB006948 2021GB006948, 2021.

Terhaar, J., Frölicher, T. L., and Joos, F.: Southern Ocean anthropogenic carbon sink constrained by sea surface salinity, Science Advances, 7, eabd5964, https://doi.org/10.1126/sciadv.abd5964, 2021.

Tjiputra, J. F., Assmann, K., and Heinze, C.: Anthropogenic carbon dynamics in the changing ocean, Ocean Science, 6, 605–614, https://doi.org/10.5194/os-6-605-2010, 2010.

Torres-Valdés, S., Roussenov, V. M., Sanders, R., Reynolds, S., Pan, X., Mather, R., Landolfi, A., Wolff, G. A., Achterberg, E. P., and Williams, R. G.: Distribution of dissolved organic nutrients and their effect on export production over the Atlantic Ocean, Global Biogeochemical Cycles, 23, https://doi.org/https://doi.org/10.1029/2008GB003389, 2009.

Valcke, S.: The OASIS3 coupler: a European climate modelling community software, Geoscientific Model Development, 6, 373–388, https://doi.org/10.5194/gmd-6-373-2013, 2013.

Wallmann, K.: Phosphorus imbalance in the global ocean?, Global Biogeochemical Cycles, 24, n/a–n/a, https://doi.org/10.1029/2009GB003643, gB4030, 2010.

Wang, W.-L., Moore, J. K., Martiny, A. C., and Primeau, F. W.: Convergent estimates of marine nitrogen fixation, Nature, 566, 205–211, https://doi.org/10.1038/s41586-019-0911-2, 2019.

Wanninkhof, R.: Relationship between wind speed and gas exchange over the ocean revisited, Limnology and Oceanography: Methods, 12, 351–362, https://doi.org/https://doi.org/10.4319/lom.2014.12.351, 2014.

Weijer, W., Cheng, W., Garuba, O. A., Hu, A., and Nadiga, B. T.: CMIP6 Models Predict Significant 21st Century Decline of the Atlantic Meridional Overturning Circulation, Geophysical Research Letters, 47, e2019GL086 075, https://doi.org/https://doi.org/10.1029/2019GL086075, 2020.

Weiss, R.: Carbon dioxide in water and seawater: the solubility of a non-ideal gas, Marine Chemistry, 2, 203 – 215, https://doi.org/https://doi.org/10.1016/0304-4203(74)90015-2, 1974.

Weiss, R. and Price, B.: Nitrous oxide solubility in water and seawater, Marine Chemistry, 8, 347 – 359, https://doi.org/https://doi.org/10.1016/0304-4203(80)90024-9, 1980.

Yoshimura, T., Nishioka, J., Saito, H., Takeda, S., Tsuda, A., and Wells, M. L.: Distributions of particulate and dissolved organic and inorganic phosphorus in North Pacific surface waters, Marine Chemistry, 103, 112 – 121, https://doi.org/https://doi.org/10.1016/j.marchem.2006.06.011, 2007.

Zalesak, S. T.: Fully multidimensional flux-corrected transport algorithms for fluids, Journal of Computational Physics, 31, 335–362, https://doi.org/https://doi.org/10.1016/0021-9991(79)90051-2, 1979.

Zickfeld, K., Fyfe, J. C., Saenko, O. A., Eby, M., and Weaver, A. J.: Response of the global carbon cycle to human-induced changes in Southern Hemisphere winds, Geophysical Research Letters, 34, https://doi.org/https://doi.org/10.1029/2006GL028797, 2007.